Immunological effects of focused ultrasound as a therapy for melanoma and breast cancer.

Lydia Kitelinger

Buffalo, NY

B.S. Biochemistry, University of Rochester, 2020

A Dissertation presented to the Graduate Faculty of
the University of Virginia in Candidacy for the
Degree of Doctor of Philosophy

Department of Pathology

University of Virginia
April 24th, 2025

Abstract

Focused ultrasound (FUS) is a clinically relevant and attractive therapeutic, due to its non-invasive and non-ionizing nature. By employing FUS, solid malignancies can be targeted and destroyed via mechanical or thermal based approaches. Significant progress in the field has been made in the design of therapeutic transducers and imaging systems which allow for precision-based targeting, however, the immunological effects induced by FUS remain unclear. While FUS treatment can promote the physical debulking of a tumor, the cell death induced through ultrasonic insult needs to be better understood. Here, we demonstrate that boiling histotripsy (BH), a mechanically ablative form of FUS, enhances melanoma-specific T-cell activation and induces T-cell expansion in the tumor draining lymph nodes (TDLNs) independent of conventional dendritic cell (cDC) migration – the canonical form of tumor antigen transport required to initiate a T-cell response in the Sham, untreated state. This suggests that tumor antigen captured by LN-resident cDCs is capable of eliciting tumor-specific T-cell activation in response to a bolus of antigen disseminated to the TDLNs by BH. Importantly, we did observe variability in the strength of T-cell activation. As we know cDCs post BH are not reaching the same heightened activation state as cDCs that have been exposed to toll-like receptor (TLR) agonists, we have identified an area of the Cancer-Immunity Cycle that would benefit from an adjuvant therapy. Further studies are required to determine which antigen presenting cell (APC) subset is required for BH-mediated T-cell activation. In addition, we found that the level of tumor debulking and constrain of primary tumor growth resulting from BH treatment, promoted substantially different immune effects in the tumor microenvironment – particularly in the skewing of cDC1 and cDC2 activation. These results both define mechanisms of BH-induced anti-tumor immunity and inform the design of improved combinatorial therapies for melanoma.

The notion that the amount of destruction elicited by FUS varies as properties of the sound waves, or ablative regimens are altered was also observed when we compared two regimens of thermally ablative FUS (TFUS) – one that induced ~20-30% tumor cell death and another that resulted in ~5% tumor cell destruction. We found that triple negative breast cancer tumors treated with the more ablative TFUS regimen had a larger amount of differentially expressed genes and pathways which sustained in the week following treatment. This was not observed with the less ablative strategy. The tune-abliity of FUS, and how exactly the sound waves are eliciting divergent immune responses remains to be assessed. In all, our studies provide clarity on the strengths and weakness of BH and TFUS as anti-tumorigenic immune stimulates and highlights areas of immune activation that could be further enhanced through dual immune-based therapies, such as TLR agonism and immune checkpoint blockade, to improve their efficacy and better leverage these FUS modalities as cancer therapeutics.

Acknowledgements

First, I would like to thank my mentors, Drs. Tim Bullock and Richard Price. Both have pushed me intellectually and supported me during my studies as my thesis project morphed during my PhD. I truly believe I got the best of two great minds mentoring me over the years. Tim has pushed me to define the testable hypothesizes, and design ways to break a system to test them. As my project began getting into the nitty gritty of immunology, Rich was always there to provide a fresh perspective and shed light on how my data could push forward the field of therapeutic ultrasound. Their passion for science was evident in every interaction I had with them. Both have created collaborative and supportive lab environments over the years, and the consistency of their lab culture speaks volumes to how they lead and manage their respective labs.

Next, I would like to thank the remaining members of my thesis committee: Dr. James Zimring, Dr. Natasha Sheybani, and Dr. Michael (Rusty) Elliott. Their guidance and insight into my projects have been invaluable, and I have learned so much from each of them. I do want to give a special acknowledgement to Dr. Zimring. I had the pleasure of taking his Metascience of Experimental Biology course as well as partake in shared PRPR seminars, and his ability to critically think and identify crucial experimental controls as well as fallacies within an experiment not only pushed me to be a better scientist, but they also inspired me to carry that level of attention to detail and those standards into my own career.

Additionally, I would like to thank all members of the Bullock and Price labs over the years. I think it is a rarity in our current day and age for people to love what they do and who they do it with, and I am happy to say that that has been my experience over the last few years. I would like to particularly acknowledge Andrew Thim. When I began my PhD, he was a senior

student in the Price lab who specialized in the engineering and physics of focused ultrasound, and as his project took a slight immunological turn, we began collaborating. He was an excellent teacher, a sounding board for advice, and all around one of the best people I have ever met. The collaboration Andrew and I had allowed each of us to shine and own our individual expertise's, while learning from one another. Ultimately, our work led to the publication of two co-first author manuscripts, and I can only hope to encounter that in sync level of collaboration again in my future careers. In addition, my PhD experience would not have been the same without Claire Conarroe and Carly Van Wagoner. Their daily support both directly at the lab bench as well as mentally and emotionally over the years has been invaluable. They are much more than lab mates, they truly have become great friends of mine, and I looked forward to seeing them every day.

My family and friends outside of UVA have also provided me endless support throughout my PhD journey. My parents and extended family have continuously supported my pursuance of a career in research, and I am grateful to have them. I was also blessed to have my family grow during my graduate career, and I am so appreciative of the family I have gained.

Lastly, I would like to thank my wife, Olivia. I was lucky enough to meet you during my second year of graduate school, and you have really gotten to experience all the highs and lows of my PhD with me. I could not thank you enough for your continuous support. You are my biggest cheerleader, and I could not ask for anyone better to go through life with. I am beyond grateful to have you, and I am excited for our future and this next chapter in our lives.

Table of Contents

List of Figures

Abbreviations

TME	Tumor microenvironment
PAMPs	Pathogen associated molecular patterns
DAMPs	Damage associated molecular patterns
APCs	Antigen presenting cells
cDCs	Conventional dendritic cells
TDLNs	Tumor-draining lymph nodes
MHC-I/-II	Major histocompatibility class I or class II
TCR	T-cell receptor
MDSCs	Myeloid-derived suppressor cells
T_{regs}	Regulatory T-cells
ILCs	Innate lymphoid cells
IL-10	Interleukin-10
TGF-β	Transforming growth factor-beta
ICB	Immune checkpoint blockade
CAR	Chimeric antigen receptor
anti-PD-1	Anti-programmed cell death protein 1
anti-PD-L1	Anti-programmed cell death protein ligand 1
Anti-CTLA-4	Anti-cytotoxic T lymphocyte associated protein 4
BrCa	Breast cancer
ER	Estrogen receptor
PR	Progesterone receptor

HER2	Human epidermal growth factor 2
TNBC	Triple negative breast cancer
M-MDSCs	Monocytic myeloid-derived suppressor cells
G-MDSCs	Granulocytic myeloid-derived suppressor cells
TAMs	Tumar-associated macrophages
TILs	Tumor-infiltrating lymphocytes
FUS	Focused ultrasound
BH	Boiling histotripsy
TFUS	Thermally ablative focused ultrasound
TNF-α	Tumor necrosis factor-alpha
IFN-γ	Interferon-gamma
GEM	Gemcitabine
TRP-2	Tyrosinase related protein 2
Zbtb46	Zinc finger and BTB domain containing 46
ZsG	ZsGreen
YUMM	Yale University melanoma model
PBS	Phosphate-buffered saline
RBC	Red blood cell
BFA	Brefeldin A
QC	Quality control
DGE	Differential gene expression
DEGs	Differentially expressed genes
GMF	Geometric mean fluorescence intensity

IF	Immunofluorescence
MCTL	Murine T-cell media
Vβ13	V-beta chain 13
ACT	Adoptive cell transfer
CTV	CellTrace Violet
cLNs	Contralateral lymph nodes
BM	Bone marrow
TLR	Toll-like receptor
WT	Wildtype
SSC	Side scatter
PCD	Passive cavitation detection
CBC	Complete blood count
ABC	ATP-binding cassette
PET	Positron emission tomography

Chapter One: General Introduction

Importance of Adaptive Immunity in Cancer

The innate and the adaptive immune systems work in conjunction to survey for cancerous cells in attempts to eliminate and prevent tumor progression. This process is referred to as the Cancer-Immunity Cycle[1]. As tumor cells die, they release their cellular contents into the tumor microenvironment (TME); this includes antigens, pathogen- and damage-associated molecular patterns (PAMPs & DAMPs). These antigens, PAMPs and DAMPs can be captured and recognized, respectively, by innate antigen presenting cells (APCs), notably conventional dendritic cells (cDCs) – which are potent activators of T-cells[2]. cDCs will process the tumor antigen, and their recognition of PAMPs and/or DAMPs can result in their activation and migration of the cDCs from the TME to secondary lymphoid organs such as the tumor-draining lymph nodes (TDLNs). The trafficking of tumor antigen by cDCs from the periphery to the TDLNs is dependent on the chemotactic axis of the CCR7 receptor and its ligands CCL19 and CCL21[3,4]. Once in the lymphoid organs, cDCs will display the antigens complexed with major histocompatibility class I (MHC-I) or class II (MHC-II) on their surface and present the complexes to T-cells. cDCs can be classified into cDC1s and cDC2s. cDC1s can directly cross-present antigen to $CD8^+$ T-cells, while cDC2s specialize in the presentation of antigen to $CD4^+$ T-cells, but they have also been shown to cross-present antigen to $CD8^+$ T-cells through antigen-antibody complexes or soluble antigen acquisition[5]. cDC1s and cDC2s can be further subdivided in migratory and resident cDCs. Migratory cDCs move throughout the periphery sampling antigen, while resident cDCs residing solely in secondary lymphoid organs. Once inside lymphoid tissues, cDCs localize to discrete niches. Migratory cDCs are positioned near T-cell rich zones within the paracortex. In contrast, resident cDCs are enriched in the lymphatic

sinuses, located closer to the perimeter of the lymph nodes[6–8]. While both migratory and resident cDCs are capable of inducing T-cell expansion[4], the presence of tumor antigen in the lymph nodes is dependent on migratory cDCs – specifically cDC1s – which through direct cell-to-cell synaptic interaction can then pass off antigen to resident cDCs[9]. These findings position migratory cDC1s as the most likely cDC subset to stimulate a cytolytic $CD8^+$ T-cell response against cancer.

The (MHC)-antigen complexes are highly selective, and the T-cell receptor (TCR) interaction that recognizes these complexes is very specific. TCR recognition is the first signal required for T-cell activation. If the T-cell also receives co-stimulatory receptor engagement as well as cytokine support from either the cDC itself or the surrounding cell milieu, it will undergo activation and proliferation – resulting in cytotoxic $CD8^+$ or helper $CD4^+$ effector formation[10]. These effector cells then must exit the TDLN and enter circulation, where they will traffic back to the TME and extravasate into the tumor. Once there, again through TCR and cognate (MHC)-antigen interaction, the T-cell will recognize its pathogenic target, and can carry out its effector function to eliminate the cancerous cell[1].

As the field of cancer immunology is actively being studied, progress can bring about observations denoting alterations to the nuances of the Cancer-Immunity Cycle[11]. However, an essential dogma that remains is the critical role of T-cells and the adaptive immune system in controlling cancer. Early evidence in preclinical models highlighted the importance of the adaptive immune system in cancer immunosurveillance[12,13]. This has been shown clinically given the positive prognostic implications of having tumors infiltrated by T-cells[14–17]. Another key component of the adaptive immune system is memory. Once the effector T-cells have performed their role, many of these T-cells will undergo cell death. However, a small proportion

of these cells will remain and become memory T-cells – capable of responding much more rapidly if they were to encounter the same non-self-antigen again[10]. Cancer cells combat immune memory by mutating and evolving quicker than the immune system, and tumors ultimately arise when malignant cells evade and escape immunosurveillance[18].

A prominent factor that hinders the development of an adaptive immune response to a tumor is the suppressive TME. Comprised of myeloid-derived suppressor cells (MDSCs)[19], regulatory T-cells (T_{regs}), pro-tumorigenic macrophages, and pro-tumorigenic innate lymphoid cells (ILCs), these microenvironments are not only rich in suppressive proteins such as IL-10 (interleukin-10)[20], TGF-β (transforming growth factor-beta)[21], and arginase-1[22], but they are also hypoxic[23] and metabolically demanding[24]. All these factors can impede T-cell activation. Additionally, cancer cells themselves, as well as tumorigenic APCs in the TME, can upregulate inhibitory receptors[25] – disarming the function of effector T-cells. In addition, the stromal network and dysregulated tumor vasculature can hinder the ability of effector T-cells to infiltrate into the solid malignancy[26]. If the T-cell can overcome these obstacles and undergo activation, the chronic exposure to antigen can result in T-cell exhaustion[27]. While immune checkpoint blockade (ICB), cancer vaccines, vascular normalization strategies, and chimeric antigen receptor (CAR) T-cells are just a few advances that aim to improve different steps along the Cancer-Immunity Cycle, these therapies are not effective for every patient – indicating primary resistance to the therapy. In some cases, patients will initially respond to immune-based treatments such as ICB and experience therapeutic benefit but then develop disease recurrence – secondary resistance[28]. Therefore, adjunct therapeutics need to be harnessed to alleviate immunosuppression and increase the immunogenicity of these tumors so that a cytolytic adaptive response against the cancer can be achieved.

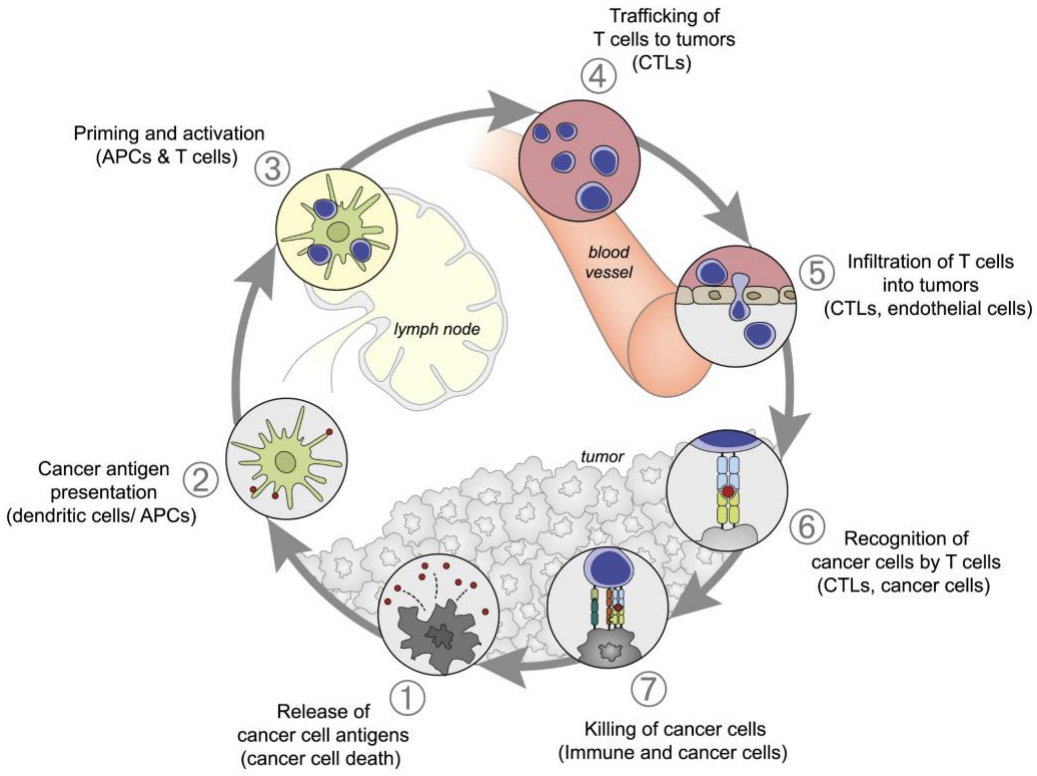

Figure 1-1: The Cancer-Immunity Cycle[1].

Melanoma & Triple Negative Breast Cancer – Therapeutic Limitations of Immunosuppression

Melanoma remains the deadliest type of skin cancer[29], and as the incidence of melanoma continues to rise, ~105,000 new cases will be diagnosed in the US alone in 2025. The therapeutic success rate depends largely on the stage at which the melanoma is detected. If the cancer is diagnosed while it remains localized to the skin, a patient's five-year relative survival rate is 99%. However, this drops to 35% for patients with distant metastatic spread. For patients with distal metastasis, surgical resection is no longer a curative treatment option, and thus, not commonly used at this stage due to its invasive nature. While incidence has risen, the mortality rates for melanoma patients has decreased over the last decade[30]. Much of this success can be attributed to the advent of both targeted therapies and ICB. Given in the adjuvant setting post-surgery, or as a first-line treatment in the case of metastatic disease, ICB immunotherapies

pembrolizumab/nivolumab (anti-PD-1; anti-programmed cell death protein 1), atezolizumab (anti-PD-L1; anti-programmed cell death protein ligand 1), and ipilimumab (anti-CTLA-4; cytotoxic T lymphocyte associated protein 4) are thought to activate and elicit an adaptive immune response against the cancer by blocking inhibitory molecules that suppress cytolytic T-cell activation and function[31]. ICB, particularly anti-PD-1 therapies, has shown efficacy in prolonging progression free and overall survival in melanoma patients with late-stage disease[32–34]. Despite its success, there remains a large subset – 40-60% of ICB treated patients – that do not respond to treatment[32,33,35], and even in the cohort that responds, ~25% will develop disease recurrence[36]. Therefore, we are studying melanoma as a model for both primary and secondary resistance to ICB.

Breast cancer (BrCa) remains the second leading cause of cancer mortality in women. In 2023, about 297,000 new cases of invasive BrCa were diagnosed[37]. This disease is inherently heterogenous. Clinically, the expression of estrogen (ER), progesterone (PR), and human epidermal growth factor 2 (HER2) receptors are used to subdivide BrCa cases—with treatment and prognosis hinging on receptor expression. Triple-negative breast cancer (TNBC) refers to a subgroup of breast tumors lacking ER, PR, and HER2 expression. TNBC makes up about 15% of all BrCa cases. Compared to hormone receptor and HER2-positive subtypes, TNBC presents as a more aggressive cancer, with a mortality rate of 40% within 5 years following diagnosis[38,39]. Mortality is the result of metastatic disease, and patients with TNBC are more likely to experience distant metastatic spread and local recurrence than patients presenting with other BrCa subtypes[40–43]. While historically TNBC has lacked targeted drug and antibody treatments that are available for ER/PR$^+$ and HER2$^+$ BrCa, in the last few years, pembrolizumab (anti-PD-1) immunotherapy has emerged as a promising neoadjuvant and late-stage therapeutic for TNBC

patients whose tumors present with a combined positive score of 10 for PD-L1 expression[44,45]. However, only ~20–34% of TNBC malignancies meet this criterion for pembrolizumab treatment[46,47], and only ~20–30% of tumors respond to immunotherapy. Therefore, we are studying TNBC as a model of primary resistance to ICB.

Both melanoma and BrCa malignancies are thought to arise when tumor cells acquire resistance to immunosurveillance and evade elimination by the immune system. This is deemed the "escape" phase of cancer progression, and it is commonly associated with the development of an immunosuppressive tumor microenvironment (TME)[48]. Prominent immune cell subsets involved in pro-tumorigenic immunity are myeloid-derived suppressor cells (MDSCs)[19]. MDSCs—both monocytic (M-MDSCs) and granulocytic (G-MDSCs)—differentiate from immature myeloid cells that undergo high levels of dysregulated myelopoiesis in response to cytokines emitted by cancers[49]. MDSCs function as pro-tumorigenic by inhibiting T-cell proliferation and their cytolytic activity[50–52], supporting tumor angiogenesis[53,54], triggering metastasis dissemination[55], and inducing the expansion of other suppressive immune cell populations such as T_{regs}[56] and tumor-associated macrophages (TAMs)[57]. MDSC enrichment is associated with poor prognosis for many cancers including melanoma and BrCa[58,59], while the presence of tumor-infiltrating lymphocytes (TILs) like $CD8^+$ and $CD4^+$ T-cells as well as cDCs in tumors is positively correlated with melanoma and BrCa prognosis and overall survival[15–17,60,61]. However, many melanomas and BrCa tumors are devoid of these advantageous immune cells. This poses a key limitation of ICB as clinical responsiveness is typically only observed in patients with these adaptive immune-infiltrated tumors. This further highlights the need for additional therapeutics to combat immunosuppression and alleviate pro-tumorigenic factors hindering adaptive immune responses to cancer.

Focused Ultrasound as a Cancer Therapeutic

Focused ultrasound (FUS) is a clinically relevant therapeutic, that employs high intensity ultrasonic waves concentrated into a small volume on the order of a grain of rice. With FUS, ablation can be applied to targets deep within the body, while avoiding off-target effects. In the last few decades, technological developments in transducer design, modes of energy delivery and real time imaging propelled the use of high intensity FUS as a treatment for solid tumor malignancies. This approach is an attractive therapy because it is non-invasive, non-ionizing, and precise. As the ultrasonic waves pass through the body, effects are only observed within the focal zone - where the sounds waves converge[62].

There are two main modalities of FUS – mechanical ablation and thermal ablation. Mechanical FUS induces tissue disruption by using pulsed, high-pressure acoustic waves (Figure 1-2A)[63]. This results in cell lysis and tissue fragmentation in the absence of thermal destruction, which can allow for sharp treatment margins between the ablated and non-ablated tissue as there is no dispersal of residual heating away from the treated region[64]. The specific mechanical ablation approach we are utilizing is boiling histotripsy (BH). BH deploys the high-pressure sound waves on the order of millisecond long pulses to produce tissue destruction through the formation of endogenous vapor bubbles that undergo oscillation and ultimately implosion[65]. In contrast, thermally ablative FUS (TFUS) utilizes ultrasound beam focusing of high intensity, continuous acoustic waves to elevate tissue temperatures within the focal zone above 60^{o}C, with minimal thermal damage to skin and tissue outside of the focus. Instantaneous cell death and coagulative necrosis occurs when tissue temperature is above 60^{o}C for 1 second[62]. The heat generated within the focal zone dissipates and generates a transition zone between the necrotic

tissue and the viable tissue (Figure 1-2B)[63]. While the cells within the transition zone do not receive the instantaneously fatal thermal dose, they do undergo thermal stress which can result in apoptosis. This is evident by the high numbers of apoptotic, caspase-3 positive cells present within the transition zone of TFUS treated tumors[66]. Although they rely on different ultrasonic properties, both mechanical and thermal FUS treatment regimens can induce debulking of the primary tumor.

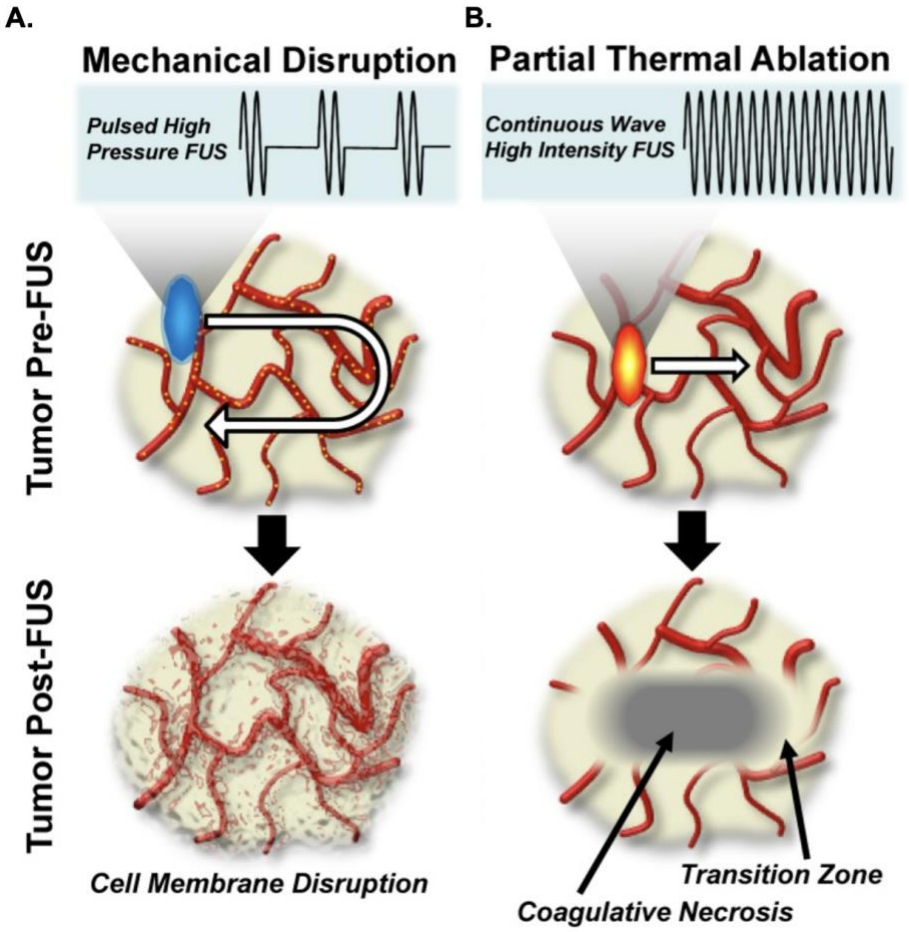

Figure 1-2. Schematic detailing the effects of Mechanical (A) or TFUS (B) on treated tumors [63].

In addition to debulking and minimizing the physical size of a tumor, FUS has been hypothesized to intersect with other areas of cancer immunity (Figure 1-3)[63]. Treating a tumor with FUS results in tumor cell death[62,66], which leads to the release of tumor antigens and

endogenous danger signals such as DAMPs. These signals include the extracellular release of ATP[67], heat shock proteins [67–71], and HMGB-1[69]. Antigen presenting cells such as cDCs, respond to DAMPs and phagocytize dying tumor cells. Evidence supports an increase in DC tumor infiltration[72], suggesting FUS ablation may be able to elicit DC recruitment into the TME, and an increase in cDC maturation – phenotypically observed by the upregulation of activation marker CD86 following FUS therapy[72–75]. Post FUS treatment, a larger number and proportion of T-cells have been found within the TME and in circulation[76–79] – indicating that FUS can induce T-cell infiltration into the tumors, as well as systemic expansion of circulating T-cell populations. Both of which would improve the likelihood of establishing an adaptive immune response against the disease. Increased expression of the pro-inflammatory cytokines such as TNF-α (tumor necrosis factor-alpha) and IFN-γ (interferon-gamma)[67,73,76,79] and reduced expression of immunosuppressive cytokines like TGF-β[79,80] have also been described post both TFUS and BH.

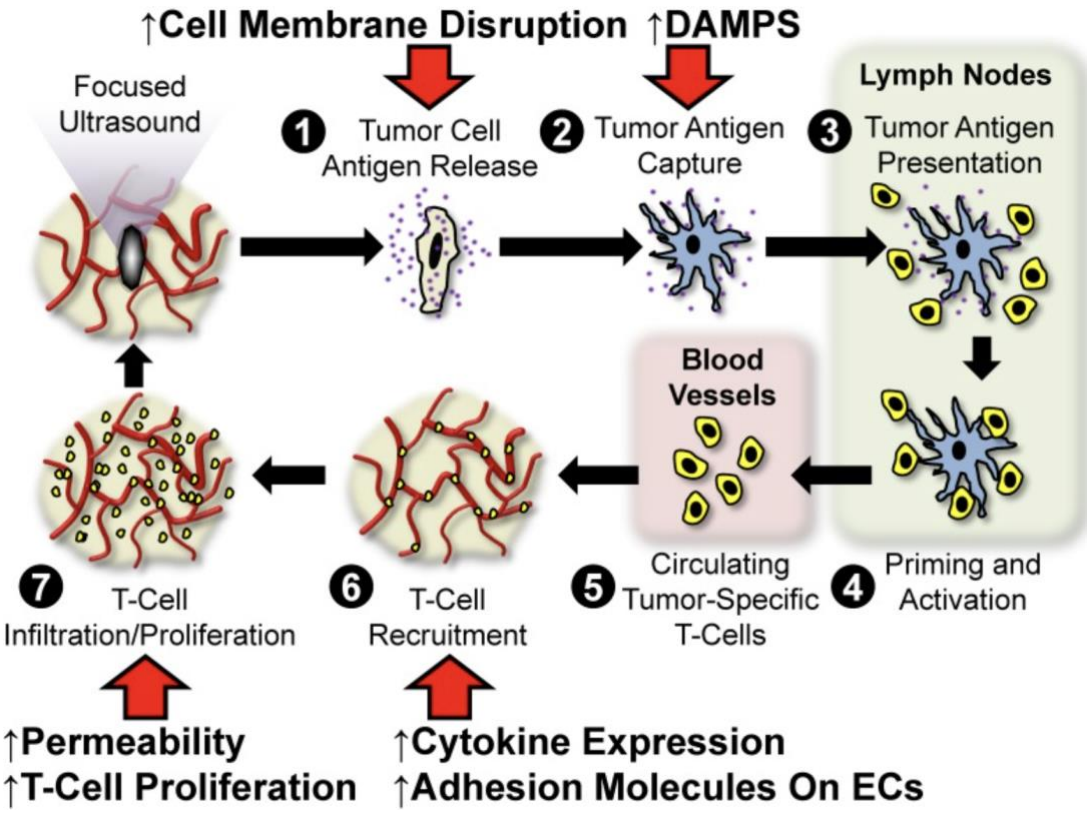

Figure 1-3. Hypothesized points of intersection between FUS and the Cancer-Immunity Cycle[63].

Given that both mechanical and thermally ablative FUS are capable of physically debulking tumors and can induce immunomodulatory effects, our research labs have proposed the use of FUS in combination with ICB to combat primary and/or secondary resistance to treatment. By comparing BH and TFUS based approaches, we are working to identify similarities and differences in FUS immunogenicity with the goal of identifying an optimal treatment regimen for achieving the most robust anti-tumor immune response. In preclinical settings, we and others have shown that treating primary solid tumors with FUS mechanical ablation can result in tumor control of distal, untreated tumors – deemed an abscopal response[75,79,81]. In some settings, constrained primary and distal tumor growth is fully dependent on $CD8^+$ T-cells, and mechanical ablation can elevate $CD8^+$ T-cell presence in ablated and abscopal tumors[79,81]. Utilizing TFUS, studies have shown that combinatorial treatment strategies with ICB or immune adjuvants, such as toll-like receptor agonists and anti-CD40, can enhance immune activation in FUS treated and untreated tumors[82,83], and our labs have also reported that the dual treatment of TFUS with the chemotherapy gemcitabine (GEM) constrains TNBC outgrowth and lengthens overall survival in a T-cell dependent manner[84]. However, while both FUS modalities are now implemented in clinical trials[85,86], FUS alone is not curative[75,81,82,84]. A key limiting factor to achieving therapeutic success is understanding how FUS as a monotherapy is impacting the immune system. It is not well understood in the field whether FUS-insult to a tumor induces a strong inflammatory response and/or a wound healing response – of which the former would support anti-tumor immunity while the latter may dampen an adaptive immune response to the cancer – and whether the sound waves can be tuned to promote a more cDC1:$CD8^+$ T-cell driven response. All the preclinical successes described above utilized different FUS parameters. Therefore, knowing how alterations to the properties of the sound

waves impacts immunogenicity and immune response to the ablation would provide much needed insight to the FUS field.

In parallel, it is also unclear how TFUS+GEM work together to confer this therapeutic advantage against TNBC. As GEM has been shown to have myeloablative effects, we hypothesized that GEM augments FUS-insulted tumor immunity in this setting by alleviating MDSC presence and immunosuppression in the TME. Whether the depletion of MDSC presence prior to TFUS treatment is essential to improve the efficacy of the ablation, or whether GEM is acting on myeloid cells that infiltrate into the TME in response to the tissue damage – i.e. a wound healing response in which granulocytic cells are the first cell type to be recruited[87] – remains unknown. Therefore, understanding the immunological consequences of FUS as a single therapy, as well as how it is working in the combinatorial setting with GEM, are essential for improving the efficacy and leveraging the utility of FUS as a cancer therapy.

Thesis Rationale

The ability of the immune system to aid or hinder the progression of malignant disease has been well established and is highlighted by the differential prognostic implications of TIL versus MDSC presence in the TME and periphery of cancer patients. While the clinical implementation of immunotherapies and the discovery of ICB have provided means to target dysfunctional T-cells, many tumors do not respond to these treatments. Thus, there is a need to leverage additional therapeutics to alleviate immunosuppression and increase the immunogenicity of tumors to achieve a cytolytic adaptive response against the cancer.

FUS is an attractive therapeutic tool because of its non-ionizing and non-invasive nature. Many tumors and metastatic lesions are deemed nonresectable due to either their physical location within the body and/or that the overall disease burden is too great on an individual that surgical removal is no longer advantageous. By employing FUS, cancerous tissue can be precisely targeted and destroyed via mechanical or thermal cell destruction. This results in the physical debulking of the tumor. Additionally, the cell death induced by FUS has been shown to have immune enhancing effects – intersecting with numerous steps of the Cancer-Immunity Cycle. However, we and others have shown that FUS alone is not curative, but when combined with adjunct treatments such as chemotherapies or ICB, FUS can induce adaptive-immune mediated control of tumors. Broadly speaking, we aimed to understand the immunological effects FUS treatment regimens have on systemic and local immunity with the goal of improving the efficacy and utility of FUS as a cancer therapy.

As a newer FUS modality, the effects that mechanically lysing tumors with BH has on tumor antigen dispersion and interaction of this antigen with cDC subsets in the TDLNs or the TME are unknown. Migratory cDC1s are believed to be the main cDC subset responsible for

promoting T-cell activation and expansion in the canonical cancer setting. This is due to their ability to acquire antigen in the periphery, migrate to the draining LNs, and cross-present the antigen to $CD8^+$ T-cells. However, cDC2s and subcapsular macrophages have also been shown to either cross-present antigen directly to $CD8^+$ T-cells or be required for $CD8^+$ T-cell priming against dead cell-associated antigens, respectively. Because LNs are well-organized structures with size exclusion properties, particulate larger than 70 kDa is constrained to the peripheral lymphatic sinuses – unable to freely drain into T-cell rich zones – making this larger antigen more likely to interact with LN-resident APCs such as cDC2s and subcapsular macrophages that are enriched in the lymphatic sinuses. The requirement of cDC trafficking of tumor antigen to the TDLNs in the context of BH treatment is unknown, and the ability of BH to elicit tumor-specific T-cell activation is unclear. Therefore, we tested whether CCR7-mediated cDC migration was required for tumor antigen deposition and tumor-specific T-cell activation in the TDLNs post BH. It is also unknown whether BH impacts APC presence, antigen acquisition, and activation status in the TME. Because the presence of immune cell subsets in melanoma can have prognostic implications, and it has been proposed that cDCs in the TME are required to provide a secondary co-stimulation signal to the T-cells to promote a robust adaptive immune response against a tumor, understanding how BH effects these cells is critical in providing insight into whether APC activation and/or their phagocytic potential following BH are rate limiting steps of the Cancer Immunity Cycle. Addressing these gaps in knowledge will provide clarity on the strengths and weakness of BH as an anti-tumorigenic immune stimulate and highlight areas of immune activation that could be further enhanced by combining immune-based therapies, such as TLR agonism and ICB, with BH to improve its efficacy and better leverage BH as a cancer therapeutic.

Additionally, when considering the immunological implications of FUS, we built off prior work that had shown that combining TFUS with the myeloablative chemotherapy gemcitabine (GEM) controls primary tumor growth and lengthens overall survival of mice bearing TNBC tumors in a T-cell dependent manner. However, the basis of enhanced T-cell control initiated by TFUS+GEM is unclear. It is unknown whether TFUS+GEM is directly promoting T-cell activation and expansion, or if the combinatorial therapy is targeting MDSC and T_{regs} – alleviating immunosuppression systemically and/or in the TME. It is also undetermined how GEM as a monotherapy impacts the immune environment of TNBC. As a systemically myeloablative chemotherapy, we hypothesized that GEM augments tumor immunity in this combinatorial setting by alleviating MDSC presence and immunosuppression in the TME. To address these unknowns, we employed myeloid depleting monoclonal antibodies to impinge on MDSC populations, and we performed time course studies of the TNBC TME to assess changes to immune populations over time as a result of GEM treatment. Given that the prior preclinical findings of *Sheybani et al*. have resulted in a phase I clinical trial here at UVA, understanding the basis of T-cell mediated TFUS+GEM immunity, and the impacts of GEM alone on the TME are crucial for the further development a durable therapy against TNBC for every patient.

Chapter Two: Materials and Methods

Mice

All mouse experiments were conducted in accordance with the guidelines and regulations of the University of Virginia and approved by the University of Virginia Animal Care and Use Committee. All the following mice, excluding the TRP-2 (tyrosinase related protein 2) TCR (T-cell receptor) transgenics that were gifted to us by Dr. Andrea Schietinger lab of the Memorial Sloan Kettering Cancer Center, were obtained from The Jackson Laboratory (Jax, Bar Harbor, ME, USA). For BrCa experiments, seven- to nine-week-old female BALB/cJ mice were acquired (Jax #000651), while eight- to ten-week-old male C57Bl/6J mice were used for the melanoma studies (Jax #000664). B6.Cg-*Thy1*^{a}/Cy Tg(TcraTcrb)8Rest/J (PMEL TCR transgenics; Jax #005023) and TRP-2 TCR transgenics were used in the adoptive cell transfer studies. For the bone marrow chimera studies, B6.SJL-*Ptprc*^{a} *Pepc*^{b}/BoyJ (CD45.1^{+} C57BL/6J; Jax #002014) were used as recipient mice, while B6(Cg)-*Zbtb46*$^{tm1(HBEGF)Mnz}$/J (Zbtb46^{dtr}; Jax #019506), C57Bl/6J (CD45.2^{+} C57BL/6J; Jax #000664), and B6.129P2(C)-*Ccr7*^{tm1Rfor}/J (CCR7$^{-/-}$; Jax #006621) were used as the donor mice. All mice were housed on a 12 h/12 h light/dark cycle and supplied food ad libitum.

Tumor models & generation

The TNBC 4T1 cell line was maintained in RPMI-1640+L-glutamine (Gibco #11875-093) supplemented with 10% fetal bovine serum (FBS, Corning (Glendale, AZ, USA) #35-010-CV). The stably transduced B16F10-ZsGreen cell line was a gift from Dr. Matthew Krummel at the University of California, San Francisco[4], and they were maintained in RPMI-1640+L-Glutamine supplemented with 5% FBS. The YUMM1.7 cell line was gifted to us by Dr. Drew

Dudley's lab at the University of Virginia. Utilizing a lentivirus containing ZsGreen (ZsG), we transduced the YUMM1.7 cells to stably express the fluorescent ZsG antigen. The ZsG^+ cells were enriched via sorting on the Influx Sorter in the UVA Flow Cytometry Core and expanded. These cells were grown in DMEM/F12 (Gibco #11330-032) supplemented with 10% FBS and 1% Non-Essential Amino Acids (NEAA; Gibco #11140-050). All cells were grown at 37 °C with 5% CO_2. Thawed cells were cultured for up to three passages for all experiments. Cells tested negative for mycoplasma prior to freezing.

3.5×10^5 4T1 cells or 3×10^5 melanoma cells (B16-ZsG or YUMM-ZsG) were subcutaneously (s.c.) implanted into the shaved right flank of mice through a 25G × 1 ½ in needle (BD PrecisionGlide Needle #305127). Tumor outgrowth was monitored via digital caliper measurements. Tumor volume was calculated as follows: volume = (length × $width^2$)/2. On the initial day of treatment, mice were randomized into cohorts in a manner that ensured matching of mean starting tumor volumes across experimental groups.

Focused ultrasound

In vivo ultrasound-guided boiling histotripsy

Mice underwent Sham or BH treatment 13 days post tumor inoculation**.** On treatment day, mice were anesthetized with an i.p. injection of ketamine hydrochloride injection (20 mg/mL; Zoetis) and dexmedetomidine hydrochloride (0.05 mg/mL; Dechra) in sterilized 0.9% saline (Hospira #PAA128035). Dexmedetomidine hydrochloride was reversed with a i.p. injection of atipamezole hydrochloride (Revertidine, Modern Veterinary Therapeutics) after Sham or BH treatment. Right flanks of mice were reshaved to remove hair that had regrown since tumor implantation, after which BH was performed using the FUSSY system. The imaging transducer has been updated to an Acuson S2000 Helix Evolution Touch, 14L5 SP imaging

probe, 10 MHz, 25 mm field width linear imaging array (Siemens, Inc.), which is orthogonally coupled to an updated 2.5 MHz center-frequency, single-element therapy transducer. An arbitrary function generator (Tektronix, AFG 3052C) and amplifier (E&I, 1040L) were used in conjunction with the therapy transducer to produce the BH treatments. Both the imaging and treatment transducers were ultrasonically coupled to the animal using degassed, deionized water at 37°C during the duration of each BH treatment. BH was applied in a pulsed fashion for 10 s, at a peak negative pressure = 21 MPa, pulse repetition frequency = 4 Hz, pulse length = 3 ms, with treatment points spaced 1 mm in a rectangular grid pattern and two planes of treatment, which were separated by 2 mm. With this ablation pattern and focal size, we calculate that ~20% of each tumor was exposed to BH. The treatment scheme is outlined in Figure 2-1A. Sham treatment comprised of fully submerging the flank tumor in the 37°C water bath for 6 minutes.

Thermal ablative focused ultrasound

Mice underwent Sham or TFUS treatment 14 days post tumor inoculation**.** On treatment day, mice were anesthetized with an i.p. injection of ketamine hydrochloride (20 mg/mL; Zoetis) and dexmedetomidine hydrochloride (0.05 mg/mL; Dechra) in sterilized 0.9% saline (Hospira #PAA128035). Dexmedetomidine hydrochloride was reversed with a i.p. injection of atipamezole hydrochloride (Revertidine, Modern Veterinary Therapeutics) after Sham or TFUS treatment. Right flanks of mice were reshaved to remove hair that had regrown since tumor implantation, after which TFUS was performed using an in-house built ultrasound-guided FUS system. This system, referred to as FUSSY, incorporates ultrasound guidance via an Acuson Sequoia 512 with a 15L8 imaging probe, an 8 MHz, 25 mm field width linear imaging array (Siemens, Inc.). This imaging transducer is placed orthogonally to the focal axis of the therapy transducer – a 1.1 MHz center-frequency, single-element transducer (Sonic Concepts Inc.) –

which is used in combination with an arbitrary function generator (Tektronix, AFG 3052C) and amplifier (E&I, 1040L) to produce TFUS treatments. This therapy transducer had an active diameter of 64 mm and radius of curvature of 63.2 mm. A custom MATLAB (Mathworks) interface integrated real time control of US imaging, stage motion, and FUS parameters. Both the imaging and treatment transducers were ultrasonically coupled to the animal using degassed,

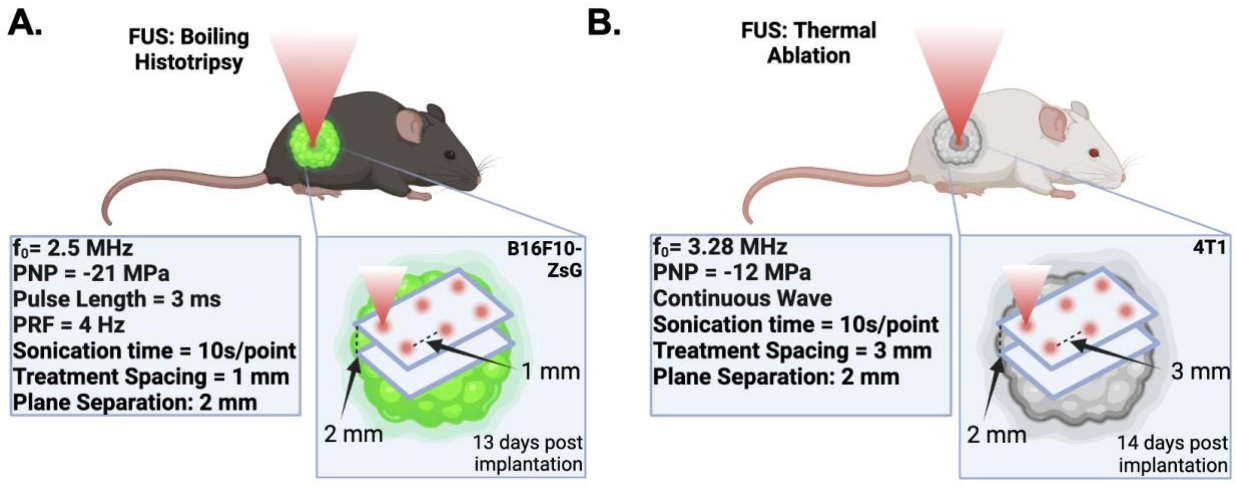

Figure 2-1. Schematic for FUS treatment parameters. **A.** Boiling histotripsy was applied with the following parameters: Operational frequency (f0 = 2.5 MHz); peak-negative pressure (PNP = -21 MPa); pulse length (3 ms); pulse repetition frequency (PRF = 4 Hz); sonication time = 10 s/point; treatment spacing = 1 mm; plane separation = 2 mm. With this treatment scheme, ~20% of the tumor volume is ablated. **B.** Thermal ablative FUS was applied with the following parameters: Operational frequency (f_0 = 3.28 MHz); peak-negative pressu3ere (PNP = -12 MPa); sonication time = 10 s/point; treatment spacing = 3 mm (unless otherwise stated); plane separation = 2 mm. This is a partial ablation regime, leaving behind viable tumor tissue.

Gemcitabine therapy

Gemcitabine (GEM; 1.2 mg/mouse in 500 µL volume; Hospira; Kalamazoo, MI, USA) was diluted in 0.9% saline and administered intraperitoneally (i.p.) 14 days after tumor inoculation. For the outgrowth studies, a total of 3 GEM doses were given once a week on days 14, 21, and 28 after the tumor implantations. Mice that did not receive GEM received an i.p. injection of "vehicle" treatment (500 µL of sterile 0.9% saline). GEM dose was based on existing literature demonstrating the use of GEM for inhibition of MDSCs in 4T1 tumor-bearing mice[88].

Preparation of single cell suspensions

Tumors

Tumors were harvested and enzymatically digested for 1 h at 37 °C in RMPI media supplemented with 5% FBS, 20 U/mL Type I Collagenase (Gibco; Grand Island, NY, USA #17018029) and 0.1 mg/mL DNase I (Roche; Branchburg, NJ, USA #10104159001). After digestion, tumors were subjected to manual homogenization (Tenbroeck Tissue Grinder #62400-518 Wheaton; Ottawa, ON, CAN) and filtered through 100 μm filter mesh (Genesee Scientific; Research Triangle Park, NC, USA #57-103) to generate single-cell suspensions, which were then spun down at 1200 RPM for 5 min (Eppendorf 5180; Enfield, CT, USA). Tumor pellets were resuspended in 10 mL of 1× PBS, and then 10 mL of Lympholyte (Cedarlane Labs; Burlington, ON, CAN #CL5035) was underlaid. Tumor samples were centrifuged in the Eppendorf 5180 at 1000 RPM for 20 min with no brake and low acceleration to separate tumor cells from lymphocytes and other immune cells. The layers above the tumor pellet were collected and placed into a clean 50 mL conical tube. 1× PBS was added to fill the conical tube to the 50 mL line. Tumor samples were spun down for 10 min at 800 RPM to pellet cells. Afterwards, the supernatants were decanted, and the pelleted cells were vortexed and resuspended in the ~200 μL1× PBS remaining in the conical tube. These cells were then transferred to a 96 well V-bottom plate for staining.

Lymph nodes

Right axillary and brachial lymph nodes were pooled for tumor draining lymph node (TDLN) analysis. LNs were subjected to manual homogenization and filtered through 100 μm filter mesh to generate single-cell suspensions. These were then spun down at 1200 RPM for 5

min, supernatants were decanted, and all the cells were transferred to a 96 well V-bottom plate for staining.

Spleens

Spleens were harvested and manually homogenized and filtered through 100 μm filter mesh to generate single-cell suspensions. They were then spun down at 1200 RPM for 5 min and resuspended in 2 mL of Red Blood Cell (RBC) Lysis Buffer (eBioscience; Middletown, VA, USA #00-4333-57) for 2 min. Afterwards, 5 mL of RMPI media containing 5%FBS was added to quench the RBC lysis buffer. Spleens were centrifuged at 1200 RPM for 5 min. Pellets were resuspended in 3 mL of media, and 100 μL of splenocytes were added to a 96 well V-bottom plate for staining.

Blood

Blood was collected via tail bleeds for temporal studies, and submandibular bleeds for terminal studies. Samples underwent RBC lysis by resuspending in 2 mL of RBC Lysis Buffer for 5 min, quenching with 3 mL of media, and then spun down at 1200 RPM for 5 min. Supernatants were decanted, and all the cells were transferred to a 96 well V-bottom plate for staining.

Flow cytometry

Once all samples were transferred to a 96 well V-bottom plate, they underwent an initial wash with 1X PBS, and then cells were stained for viability using Fixable Live/Dead Blue for 30 min at 4 °C. Next, the samples were incubated with anti-mouse 5 μg/mL CD16/32 to block Fc gamma receptors for 15 min at 4 °C. In panels where CCR7 was stained for, cells were spun down post Fc block and resuspended in 100uL of anti-CCR7 antibody made up 1:100 in FACS + 2% NMS (normal mouse serum; Valley Biomedical, Inc., Winchester, VA, USA, # AS3054), and

stained for 30 min at 37 °C. Afterwards, cells were washed with FACS buffer; spun down; resuspended in a mixture of Brilliant Stain Buffer and FACS + 2% NMS at a ratio of 1:9, respectively; and stained for 30 min at 4 °C with fluorescent monoclonal antibodies for surface markers.

Following a wash with FACs buffer, the eBioscience FOXp3/Transcription Factor Staining Buffer Set (#00-5523-00) was used for intranuclear staining. Cells were resuspended in 100 µL of solution 3 parts Fix/Perm Diluent + 1 part Fix/Perm Concentrate for 55 min at 4 °C. Then, the samples were stained for intracellular and intranuclear factors with antibodies made up in 1X Perm/Wash Buffer at 4 °C for 25 min. Following a wash with 1X Perm Buffer, the cells were lastly fixed in 1X BD FACS Lysis in the dark for 10 min at room temperature. They were then resuspended in FACS buffer for running on the cytometer. Flow cytometry was performed with the Cytek Aurora Borealis (Cytek Biosciences; Fremont, CA, USA) and SpectroFlo v3.0.3 software (Cytek Biosciences). Data were analyzed using FlowJo 10 software (FlowJo, LLC; Ashland, OR, USA).

tSNE analysis on the granulocytic ($Ly6G^+CD11b^+$) populations in the TME was also performed in FlowJo 10 with an iteration of 1000, perplexity of 30, learning rate (eta) of 10500, KNN algorithm of exact (vantage point tree), and gradient algorithm of Barnes–Hut.

T-cell depletions

T-cell depletion antibodies—anti-CD8 (2.43 clone; BioXCell #BE0061), anti-CD4 (GK1.5 clone; BioXCell #BE0003-1) or rat isotype control IgG2b (LTF-2 clone; BioXCell #BE0090) —were diluted in sterilized 0.9% saline and administered i.p. every 3 to 4 days starting at day 20 (6 days post-TFUS) for a total of seven doses (100 µg of each antibody for a

total 200 μg per mouse). Mice were bled on day 27 after 3 doses of depletion antibodies were administered, and lymphocyte depletion was confirmed by flow cytometry.

Brefeldin A injections

To prevent cytokine secretion from cells, 250 μg of Brefeldin A (BFA; Selleck Chemicals; Randor, PA, USA # S7046) diluted in sterilized 0.9% saline was administered in 200 μL intraperitoneally to tumor-bearing mice 4h prior to harvest.

RNA extraction, QC, and library preparations

At 24 h and 168 h (7 days) after GEM administration, tumors were excised from 4T1 tumor-bearing mice and placed into RNAlater solution (Invitrogen; Carlsbad, CA, USA #AM7020). Samples were kept at 4 °C for 24 h and then stored at −80 °C to preserve RNA prior to extraction. The RNeasy Lipid Tissue Mini Kit (Qiagen; Germantown, MD, USA #74804) was used to extract RNA from the tumors. This work was performed by the Biorepository and Tissue Research Facility, which is supported by the University of Virginia School of Medicine, Research Resource Identifiers (RRID): SCR_022971.

RNA quality control (QC), library preps, and sequencing were performed by UVA's Genome Analysis and Technology Core, RRID: SCR_018883. RNA QC was run with the Agilent TapeStation RNA kit. Library preps were performed with the NEBNext® Poly(A) mRNA Magnetic Isolation Module (cat# E7490L) and NEBNext Ultra II Directional RNA Library Prep Kit for Illumina (cat# E7760L). Library QC was performed with the Agilent TapeStation D5000 HS kit and Qubit dsDNA High Sensitivity kit (Cat# Q32851). Sequencing was performed with Illumina's NextSeq 2000 P3-100 kit.

RNA-sequencing analysis

Quality control

The UVA Bioinformatics Core received 30 million (on an average) paired end reads (on an average 75 bases long read) for each of the replicates sufficient for gene level quantitation. Read quality was assessed using fastqc program http://www.bioinformatics.babraham.ac.uk/projects/fastqc/ (accessed on 31 March 2023), and the raw data quality report was generated using the MultiQC tool[89]. They had a good quality read, and there were no traces of adaptor contamination.

Mapping and quantitation

The Bioinformatics Core utilized the "splice aware" aligner "STAR"[90] aligner for mapping the reads. Prior to mapping, they constructed a mouse reference index based on the GRCm38 mouse genome reference (Mus_musculus.GRCm38.dna.primary assembly.fa and Mus_musculus.GRCm38.91.chr.gtf) and setting the "sjdboverhang" parameter to 74 to match the read length of our samples. Subsequently, read mapping and quantification were conducted, and more than 95% of the reads mapped to the mouse genome and transcriptome. Gene-based read counts were derived from the aligned reads, and subsequently, a count matrix was generated, serving as the input file for the analysis of differential gene expression.

Differential gene expression analysis (DGE)

The DESeq2 package[91] was used to conduct the differential gene expression analysis. Low expressed genes (genes expressed only in a few replicates and had low counts) were excluded from the analysis before identifying differentially expressed genes. Data normalization, dispersion estimates, and model fitting (negative binomial) was carried out with the DESeq function. The log-transformed, normalized gene expression of the 500 most variable genes were used to perform an unsupervised principal component analysis. The differentially expressed genes were ranked based on the log2fold change and FDR corrected p-values. Further additional

noise was removed using adaptive shrinkage estimators using "apeglm" argument in "lfcShrink" function[92]. The MA plot (function plotMA in DESeq2) and Volcano plot representing significant upregulated and downregulated genes was generated using the specific functions in DESeq2 package. The heat map was generated using the "pheatmap" package in R.

Pathway analysis

Pathway analysis was performed using "fgsea" package in Bioconductor R (https://bioconductor.org/packages/release/bioc/html/fgsea.html, accessed on 31 March 2023). The reference database for mouse pathway enrichment analysis comprised Hallmark, C2, C5, and Hallmark gene sets from the "msigdb"[93–95]. For each pathway analysis, a list of the top 10 significant pathways based on p-value was produced. Additionally, GSEA-style plots were generated for both upregulated and downregulated pathways.

Immunofluorescent staining

Tumor draining axillary and brachial lymph nodes were harvested from B16ZsG mice 1.5-2.5 h post BH or Sham treatment and placed into 15mL conical tubes containing 2mL 4% paraformaldehyde (Santa Cruz Biotechnology #sc-281692). LNs were kept at 4 °C overnight. The following day, LNs were transferred to new 15mL conical tubes containing 2mL 30% sucrose, and were placed back at 4 °C for 24-48 h. LNs were required to dehydrate and sink in the sucrose media before being frozen into Optimal Cutting Temperature Compound (OCT; Sakura #4583) blocks and stored at -80 °C before sectioning and staining. Naïve LNs were harvested and processed from non-tumor bearing mice as a ZsG control.

To assess the spatial distribution and location of ZsGreen tumor antigen and ZsG+ dendritic cells, 12 um mounted sections were incubated with blocking solution (1% normal donkey serum in 2% BSA and 0.1% Tween 20 PBS) at room temperature for 1 h. Sections were

next incubated overnight at 4°C with primary antibodies, including rabbit anti-CD11c (1:300, Cell Signaling #97585S), and either rat anti-MHCII (1:200, Invitrogen #14-5321-82) or rat anti-Lyve-1 (1:200, Invitrogen #14-0443082), and were diluted in 2% BSA and 0.1% Tween 20 in PBS. After washing 3x for 10 min in 0.1% Tween 20 PBS, sections were incubated for 1 h at room temp with Alexa Fluor 568 donkey anti-rat (1:400, # A78946) and Alexa Fluor 647 donkey anti-rabbit (1:400, #32795). After washing 3x for 10 min in 0.1% Tween 20 PBS, sections were incubated for 15 mins. at room temp with DAPI (1:1000, ThermoFisher #62248). After final washes in PBS, sections were sealed with ProLong Gold antifade reagent (Invitrogen, #P36930) and a Fisherbrand Microscope Cover Glass (#12-544-E) was placed over top of the sections for confocal imaging.

Confocal microscopy & analysis

Stained sections were imaged with a Leica Stellaris 5 confocal microscope (Leica Microsystems) using sequential scanning mode for DAPI, ZsGreen, 568 and 647 dyes. Images (512 x 512 pixels), tiled in the x-y plane were collected using a 20x objective. Individual regions of interest (ROIs) were manually drawn around each LN. All analysis was done using Fiji/ImageJ. To determine ZsGreen tumor antigen abundance and intensity in the LNs, % area and mean grey scale intensity was calculated for the ZsGreen channel in each ROI. Tumor antigen presence in lymphatic endothelium was assessed by comparing the co-localization of ZsGreen presence with Lyve-1 expression between Sham and BH TDLNs. To quantify the proportion of tumor antigen expressing DCs ($CD11c^+MHCII^+$), a colocalization mask of CD11c and MHCII expressing pixels was created for each ROI. This mask was then colocalized with ZsGreen presence, and the % area of ZsG^+ $CD11c^+MHCII^+$ was divided by the % area of $CD11c^+MHCII^+$ x 100 to get the % of DCs ZsG^+. For all analysis, 4-7 slices per LN were

analyzed, and values were averaged for each LN. Final images were adjusted and assembled in PowerPoint.

Adoptive T-cell transfers

Spleens and lymph nodes were harvested from PMEL or TRP-2 TCR transgenic mice into murine T-cell media (MCTL; RPMI-1640+L-glutamine supplemented with 10% FBS, 1% 100x NEAA, 1.5% HEPES (Gibco # 15630-080), 2% 50x Essential Amino Acids (Gibco #11130-051), 2% Sodium Pyruvate (Gibco #11360-070), 2% 100x L-glutamine (Gibco #25030-081), 0.8% 1M Sodium Hydroxide (Sigma #S2770), 0.1% 50mg/mL Gentamicin (Gibco #15750-060), and 0.1% 0.05M 2-betamercaptoethanol (Sigma #M-7522). Organs were processed into single cell suspensions accordingly as described in the previous section: "Preparation of single cell suspensions." CD8 T-cells were isolated via negative magnetic enrichment (eBioscience # 8804-6822-74). Following CD8 enrichment, cells were stained for 20 min at 37°C with CellTrace Violet (Thermo Scientific #C34557) at a concentration of 5uM in serum free MCTL. Following incubation, complete MCTL media was used to quench the cells, which were then spun down at 1200 RPM for 5 min. The T-cells were resuspended in calcium and magnesium free Hanks' Balanced Salt Solution (HBSS; Gibco #14175-095) to a final volume of 10^7 cells/mL. One million of these cells (100uL) were intravenously (i.v.) injected into recipient mice prior to Sham or BH treatment for the adoptive cell transfer (ACT).

For experiments where proliferation was assessed, a sphingosine-1-phosphate receptor agonist, FTY720 (Sigma-Aldrich #SML0700), was used to block T-cell egress from the lymphoid organs. These mice received drinking water supplemented with 2ug/mL FTY720 two days prior to ACT as well as daily i.p. injections of 25ug FTY20 in 100uL 1X PBS beginning one day prior to ACT until the end of study.

Vaccinations

These mice were used as positive controls for PMEL and TRP-2 $CD8^+$ T-cell activation and expansion post ACT. They were injected i.p. on day 13 with 100 μg αCD40 (FGK45; Ichor #ICH1073), 75 μg polyI:CLC (Oncovir, Inc., Hiltonol®), 25 μg hgp100 (GenScript #RP20344), and when stated 50 μg mTRP-2 (GenScript #RP20250) in 200μL of 0.9% saline.

PolyI:CLC delivery

50 μg of polyI:CLC diluted int 200 μL of 0.9% saline was injected i.p. day 13 post tumor inoculation.

Myeloid depleting antibodies

Myeloid depleting antibodies—anti-Ly6G (1A8 clone; BioXCell #BE0075-1), anti-GR1 (RB6-8C5 clone; BioXCell #BE0075) rat isotype controls; IgG2a (2A3 clone; BioXCell #BE0089) & IgG2b (LTF-2 clone; BioXCell #BE0090), and anti-rat kappa immunoglobulin light chain (MAR 18.5 clone; BioXCell #BE0122)—were diluted in sterilized 0.9% saline and administered i.p. at varying doses and timelines. Details for each experiments exact administration can be found in figure schematics and figure legends.

Anti-Interferon gamma delivery

To neutralize IFN-γ, 200 μg of either anti-IFN-γ (BioXCell; Bridgeport, NJ, USA XMG1.2 #BE0055) or the IgG1 isotype control (BioXCell HRPN #BE0088) was diluted in sterilized 0.9% saline was administered i.p. to 4T1 tumor-bearing mice immediately preceding GEM or saline injections on days 14, 21, and 28 after tumor implantation.

Anti-CCR7 delivery

To impede cDC migration, 10 µg of either αCCR7 (Invitrogen #16-1971-85) or isotype control IgG2α (Invitrogen #16-4321-85) was administered in 100 µL of 0.9% saline on days 9, 11 and 13 immediately prior to Sham or BH treatment.

Generating bone marrow chimeras

Whole chimeras

Recipient CD45.1^{+} C57BL/6J mice were placed on Sulfamethoxazole/Trimethoprim (Sulfa; TEVA #NDC 0703-9526-01) water at a concentration of 95 mg/kg/24 h 2-3 days prior to the first irradiation dose. They remained on Sulfa water for 21 days following irradiation. These mice were irradiated over two sessions 24 h apart on the Mark1 68A irradiator by Cesium-137 (JL Shepherd) for a total of 1200 rads (600 rads/session). Donor mouse femurs and tibias were collected from both Zbtb46^{dtr} and CD45.2^{+} C57BL/6J mice into 1X PBS + 10% FBS solution. In a tissue culture hood, bones were dried and sprayed with 70% ethanol for sterilization. Once dried, the bones were placed knee side down in a 0.5mL Eppendorf tube containing a hole in the bottom from an 18gauge needle. This 0.5mL Eppendorf containing the bones was placed inside a larger 1.5mL Eppendorf tube. Parafilm was placed over top of the shut 0.5mL Eppendorf to prevent opening and breaking sterility. These 1.5mL Eppendorf's were spun down in a microcentrifuge at 10,000g for 30 sec. The bones remained in the 0.5mL Eppendorf, while BM cells pelleted into the 1.5mL Eppendorf. Pellets were transferred into 15mL conical tubes and resuspended in 5mL of ACK Lysis Buffer (Gibco #A10492-01) for 2 min. Afterwards, 10mL of 1X PBS + 10% FBS was added to quench the lysis buffer. BM was filtered through 40um mesh, centrifuged at 1200 RPM for 5 min, and resuspended in HBSS to a final concentration of 2 x 10^{7} cells/mL. 2 million total cells (100uL) were injected i.v. following the second irradiation dose.

Mixed chimeras

The same procedures were followed for the mixed chimeras as previously stated for the whole chimeras, with CD45.1^{+} C57BL/6J mice being used as the recipients. Donor mouse femurs and tibias were collected from both Zbtb46^{dtr} and CCR7$^{-/-}$ mice. Following cell preparation and ACK Lysis, both Zbtb46^{dtr} and CCR7$^{-/-}$ BM was resuspended in HBSS to a final concentration of 2 x 10^{7} cells/mL. Zbtb46^{dtr} and CCR7$^{-/-}$ BM was combined into a single solution, and 2 million total cells (100uL) were injected i.v. following the second irradiation dose.

Statistical analysis

Statistical analyses were performed in GraphPad Prism 9 (GraphPad Software). Mouse survival was analyzed using a Kaplan–Meier analysis, and a log-rank (Mantel–Cox) test was used to assess significance. ROUT outliers' analysis with Q = 0.1% was ran prior to any flow cytometry analysis. Groups of summary data across time were compared using a full-model, two-way analysis of variance (ANOVA) with multiple comparisons, comparing each cell mean with the other cell mean in that row. We acknowledge changes in the immune environment over time after tumor implantation and chose to focus on alterations to the immune repertoire in response to GEM alone or BH at each individual timepoint, rather than changes over time. When comparing two groups of flow cytometry data at a single timepoint, an unpaired, two-tailed *t*-test with Welch's correction (i.e., did not assume equal standard deviations) was performed. To assess correlations, a simple linear regression model was used. All figures, unless otherwise stated in the figure legend, show the mean ± standard deviation (SD). *p*-values and significance are specified in figure legends. Graphical renderings were made with BioRender.com

Chapter Three: Mechanical ablation enhances acute activation of melanoma-specific T cells & tumor antigen acquisition by conventional dendritic cells in a trafficking independent manner.

INTRODUCTION

Melanoma remains the deadliest type of skin cancer. While the incidence rate for melanoma continues to rise in 2025, there has been success over the last decade in reducing the mortality rate of this disease[30]. Much of this success can be attributed to the advent of both targeted therapies immune checkpoint blockade (ICB) – there remains a large subset of patients, 40-60%, that do not respond to this treatment[32,33,35]. Additionally, the presence of tumor-infiltrating lymphocytes (TILs) such as $CD8^+$ and $CD4^+$ T cells positively correlates melanoma prognosis and responsive to ICB[15,17,96]. Therefore, there is a clinical need for a therapeutic intervention that can alter tumor immunogenicity, enhance TIL presence, and elicit immune activation against the cancer.

Boiling histotripsy (BH) is a mechanical form of focused ultrasound (FUS) - a non-invasive and non-ionizing therapy that utilizes the concentration of acoustic waves into a small volume on the order of a grain of rice. By deploying high-pressure, millisecond long ultrasound pulses into a tumor, tissue fractionization is induced through cavitation and the formation of endogenous vapor bubbles that undergo oscillation and ultimately implosion[97]. BH is an attractive therapeutic modality not only due to the non-invasive nature of FUS, but also because this is a non-thermal based approach. The non-thermal nature is believed to achieve sharp treatment margins between the ablated and non-ablated tissue as there is no dispersal of residual heating away from the treated region[64]. This is imperative when trying to treat cancerous lesions

that are in close proximity to central nerves or major organs that may be damaged by thermal stress. We and others have shown that treating primary solid tumors with FUS mechanical ablation can result in tumor control of distal, untreated tumors – deemed an abscopal response [75,79,81]. In some settings, constrained primary and distal tumor growth is fully dependent on $CD8^+$ T-cells, and mechanical ablation can elevate $CD8^+$ T-cell presence in ablated and abscopal tumors[79,81]. While BH appears to be a promising debulking and immune-stimulating treatment, it is not curative in pre-clinical melanoma models [75,81]. Therefore, it is crucial to understand how BH is impacting the immune system as monotherapy so that we can implore efficacious combinatorial regimens against this disease, while limiting toxicity that can arise when treating patients with ICB and immune agonists[31].

In previous studies, we were able to assess the effects of BH on tumor antigen acquisition by antigen presenting cells (APCs) in the tumor-draining lymph nodes (TDLNs) by utilizing a murine melanoma cell line that was stably transduced to express the fluorescent antigen ZsGreen (ZsG)[75]. While we examined presence of ZsG antigen in many APCs post BH, we focused specifically on conventional dendritic cells (cDCs) because they are the professional APCs capable of eliciting robust T-cell responses[2]. cDCs can be classified into cDC1s and cDC2s. cDC1s can directly cross-present antigen to $CD8^+$ T-cells, while cDC2s specialize in the presentation of antigen to $CD4^+$ T-cells, but they have also been shown to cross-present antigen to $CD8^+$ T-cells through antigen-antibody complexes[5]. cDC1s and cDC2s can be further subdivided in migratory and resident subsets. Migratory cDCs move throughout the periphery sampling antigen, while resident cDCs residing solely in secondary lymphoid organs such as the lymph nodes (LNs). Once inside lymphoid tissues, cDCs localize to discrete niches[6–8]. This is critical when thinking about where antigen liberated from BH treatment is going within the

TDLNs because LNs are well-organized structures that have size exclusion properties. Particulate antigen larger than 70 kDa is constrained to the peripheral lymphatic sinuses and is unable to freely drain into the conduit network, which reaches deep into the LN paracortex[98–100], where migratory cDC1s are positioned near T-cell rich zones. In contrast, LN-resident cDCs are enriched in the lymphatic sinuses[6–8] . While both migratory and resident cDCs are capable of inducing T-cell expansion, the presence of tumor antigen in the lymph nodes is dependent on migratory cDCs – specifically cDC1s[4] – which through direct cell-to-cell synaptic interaction can then pass off antigen to resident cDC1s[9]. Although our prior work utilizing spectral flow cytometry enabled us to examine tumor antigen acquisition in distinct APCs in the TDLNs, those studies did not provide spatial information about where this tumor antigen is localizing within the TDLNs. Knowing how tumor antigen is making its way to the TDLNs and where it is localizing, will provide insight into what cells it is interacting with first, and what cells it is predominately interacting with. This is essential for understanding how an adaptive immune response is being initiated by BH treatment as it is unknown whether this mechanical insult to the tumor is liberating cell-free antigen that can bypass the requirement of migratory cDC trafficking for the stimulation of a $CD8^+$ T-cell response against the cancer.

Here, we show that the bolus of tumor antigen in the TDLNs post BH localizes acutely to the lymphatic sinuses – indicative of antigen drainage and lymph-borne antigen. We found that BH significantly enhances melanoma-specific T-cell activation and induces T-cell expansion in TDLNs. When we impeded the CCR7 chemotactic axis that is required for cDC migration from the periphery into the draining LNs[4,101], BH-induced antigen presence and T-cell expansion was not impacted. This suggests that tumor antigen captured by LN-resident cDCs is eliciting tumor-specific T-cells responses in response to BH treatment. Overall, these results both define

mechanisms of BH-induced anti-tumor immunity and inform the design of improved combinatorial therapies for melanoma.

RESULTS

Boiling histotripsy liberated tumor antigen is acutely localized to the lymphatic sinuses

We have previously reported that treating B16F10-ZsGreen (B16-ZsG) murine melanoma tumors with BH results in the accumulation of ZsG tumor antigen in the TDLNs and the acquisition of this antigen by cDCs 24hrs post treatment[75]. We have since repeated this work in another murine melanoma model YUMM1.7 (Yale University Melanoma Model)[102] - a genomically stable model that expresses the human-relevant mutations $Braf^{V600E}$ and loss of *Pten* - which we transduced to express ZsG (YUMM-ZsG) (Figure 3-1). While the previous spectral flow cytometric analysis of BH treated melanoma allowed us to assess single cell up-take of ZsG, it did not provide any spatial information regarding the location of the tumor antigen following BH. To understand where tumor antigen localizes acutely within the TDLNs post BH with respect to $CD11c^{+}MHC\text{-}II^{+}$ DCs, we utilized immunofluorescent (IF) microscopy (Figure 3-2A). Consistent with our prior flow cytometry analysis, we found a significant increase in the amount ZsG tumor antigen present in the TDLNs (Figure 3-2B) as well as the area of the TDLNs containing the tumor antigen (Figure 3-2C). This indicates that applying BH to these tumors increases the availability of tumor antigen across the TDLNs, potentially increasing the opportunity of naïve T cells to encounter professional APC. Additionally, consistent with the previous flow cytometry data, we observed no difference in the proportion of $CD11c^{+}MHC\text{-}II^{+}$ DCs between Sham and BH TDLNs (Figure 3-2D), while still significantly increasing the proportion of DCs that are ZsG^{+} in the BH TDLNs compared to the Sham controls (Figure 3-2E);

suggesting that DC-mediating trafficking and migration of tumor antigen is not responsible for the burst of antigen presence in the TDLNs induced acutely following BH treatment.

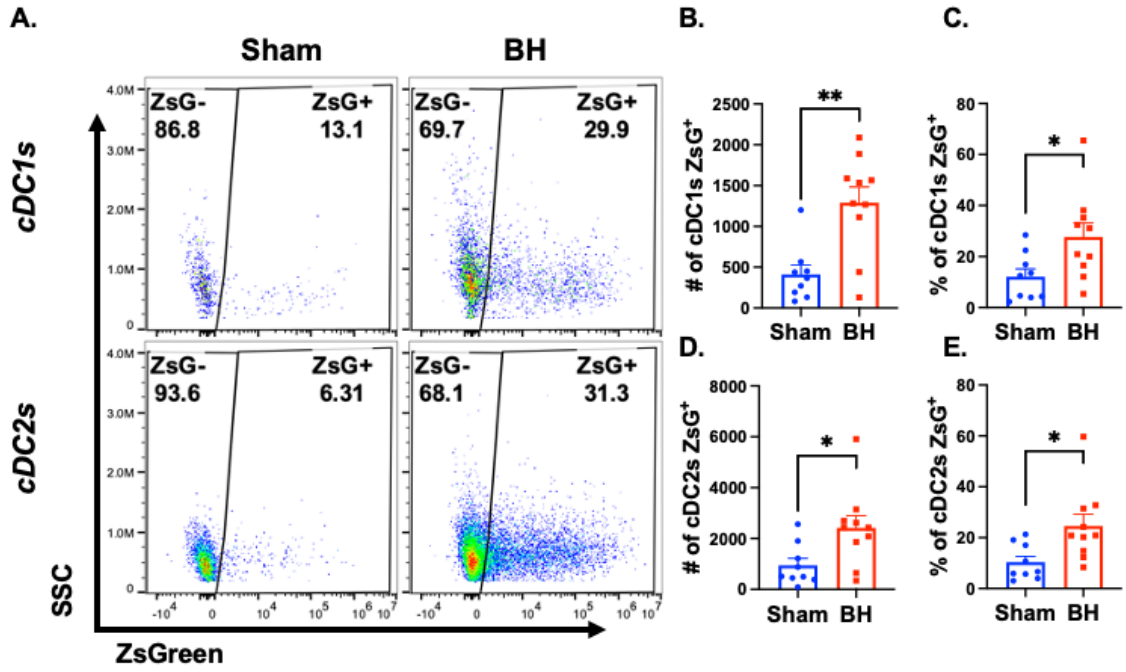

Figure 3-1. Elevated ZsG tumor antigen acquisition by conventional type 1 and type 2 dendritic cells (cDC1s & cDC2s) in the TDLNs was observed 24 h post BH treatment of YUMM-ZsG melanomas. A. Representative flow plots showing ZsG expression in cDC1s (top) and cDC2s (bottom) in the TDLNs of Sham and BH cohorts. Frequencies shown are of the parent population. **B & D.** Quantification of the number of ZsG^+ cDC1s (**B**) and cDC2s (D). **C & E.** Bar graph showing the proportion of cDC1s (**C**) and cDC2s (**E**). that are ZsG^+. (n=9-10) Unpaired t test with Welch's correction: ∗ P<0.05, ∗∗ P<0.01; ROUT Outliers analysis with Q=0.1%. Mean ± SEM (standard error of the mean).

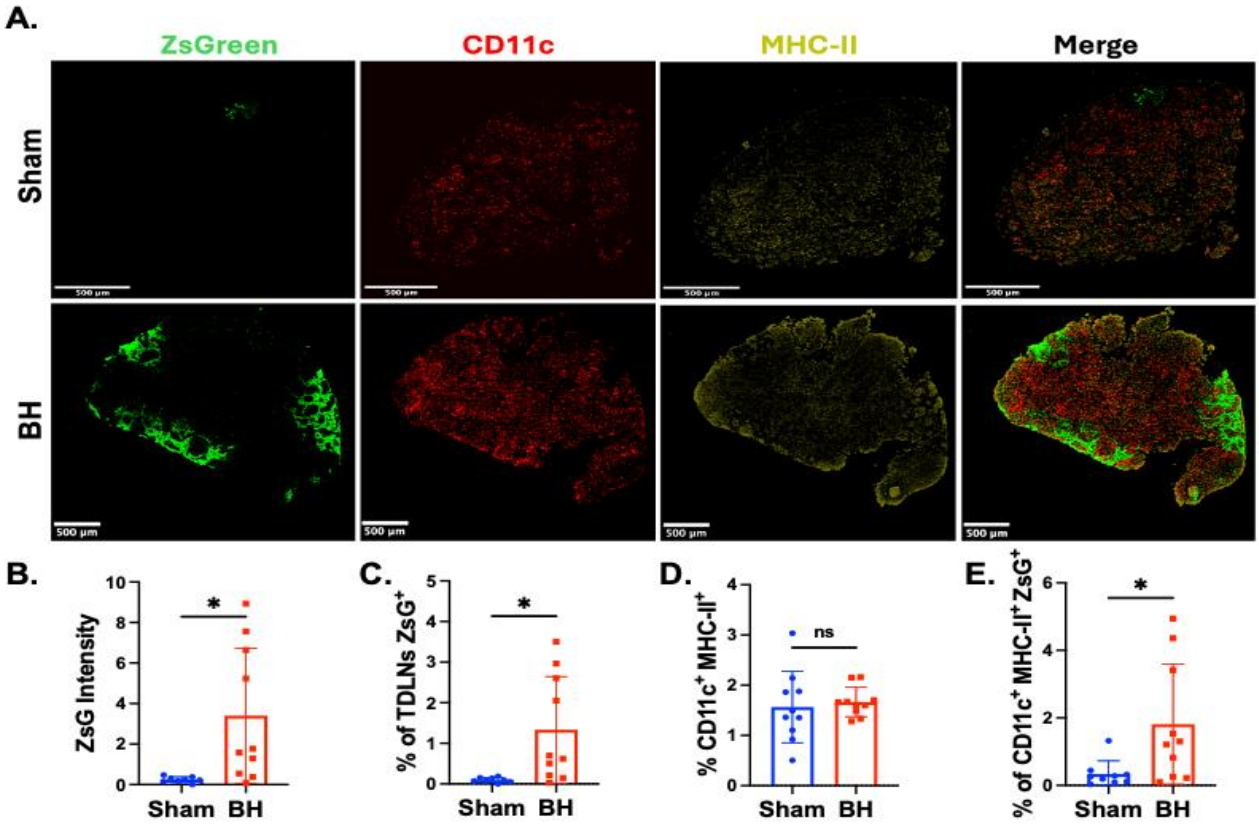

Figure 3-2. BH acutely increases ZsG tumor antigen presence and colocalization with dendritic cells in the TDLNs, while not altering DC presence. A. Immunofluorescent images of Axillary TDLNs showing elevated abundance of ZsG 2 h post BH or Sham treatment co-localizing with $CD11c^{+}MHC\text{-}II^{+}$ dendritic cells. **B.** IF quantification of the mean gray scale intensity of ZsG averaged a crossed both the Axillary and Brachial TDLNs. **C.** IF quantification for the proportion of the TDLNs that is expressing the ZsG tumor antigen averaged a crossed both LNs. **D.** IF quantification for the proportion of $CD11c^{+}MHC\text{-}II^{+}$ DCs averaged from both TDLNs. **E.** IF quantification for the proportion of $CD11c^{+}MHC\text{-}II^{+}$ DCs co-localized with ZsG tumor antigen averaged a crossed both TDLNs. (n=10) Unpaired t test with Welch's correction: ns = non-significant, ∗ $P<0.05$; ROUT Outliers analysis with Q=0.1%. Mean ± SD.

We noticed that much of the ZsG antigen was present on the outer edges of the lymph nodes, in regions where the lymphatic sinuses are located. To determine whether liberated tumor antigen post BH was indeed localizing in the lymphatic sinuses, we utilized IF on B16-ZsG TDLNs 2-3 h post Sham or BH treatment and stained for Lyve-1, a marker of lymphatic endothelium (Figure 3-3A). We found that following BH, there was a significant increase in the colocalization and proportion of the $Lyve\text{-}1^{+}$ endothelium that contained ZsG tumor antigen (Figure 3-3B). The most prominent phagocytic APC that resides in the $Lyve\text{-}1^{+}$ subcapsular and

medullary sinuses are $CD169^+$ macrophages[103,104]. By flow cytometry, we can identify these cells in the TDLNs (Figure 3-4A), and when we compared the total number of $CD169^+$ sinus macrophages between the Sham and BH cohorts, we observed no difference (Figure 3-4B). However, we observed that BH significantly increased the number and proportion of ZsG^+ $CD169^+$ sinus macrophages (Figure 3-4C-E). We also enumerated the amount of tumor antigen these cells were acquiring on a per cell basis by analyzing the Geometric Mean Fluorescence intensity (GMF) of ZsG on ZsG^+ $CD169^+$ macrophages and found that there was a significant increase in the amount of antigen in these macrophages after BH compared to the Sham controls (Figure 3-4F). Although the most abundant, $CD169^+$ sinus macrophages are not the only APCs that inhabit the lymphatic sinuses. LN-resident conventional type 2 dendritic cells (cDC2s; $CD11b^+XCR1^-CD11c^+MHC\text{-}II^{lo}$) have also been shown to be enriched within the lymphatic endothelium, where they can phagocytose and process lymph-borne antigens to promote an immune response[6,7]. Similar to the $CD169^+$ macrophages, we found that BH treatment results in the significant increase of tumor antigen positive LN-resident cDC2s as well as an elevation in the amount of ZsG antigen these cells are acquiring (Figure 3-5A-E, respectively). Taken together, these findings demonstrate that mechanically ablating B16-ZsG melanoma tumors results in the rapid distribution of tumor antigen to the TDLNs where it localizes to peripheral regions of the LNs where it will first encounter APCs residing in the lymphatic endothelium – rather than migratory APCs that tend to be located deeper within the LNs[6,8].

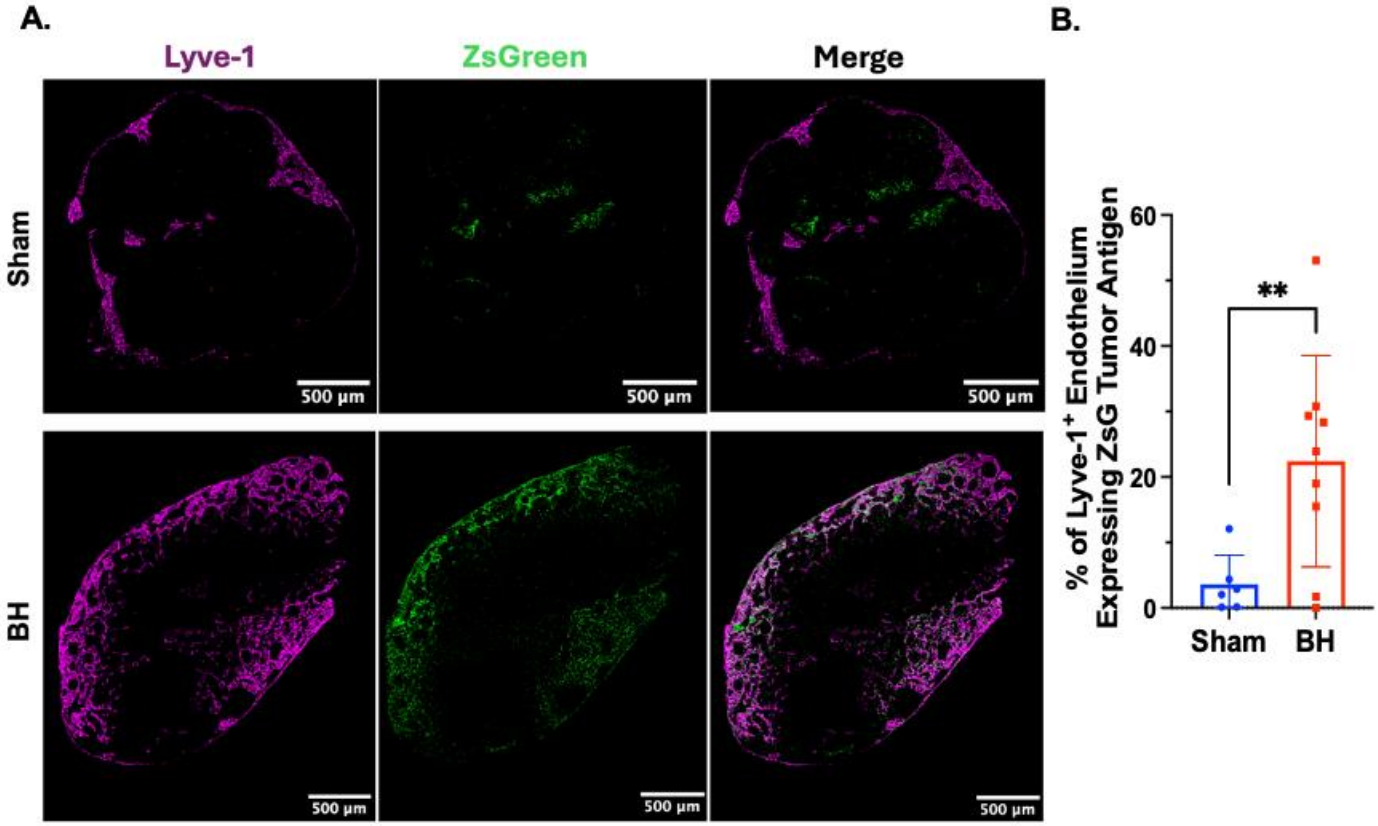

Figure 3-3. BH-liberated ZsG tumor antigen localizes to the lymphatic sinuses. A. Immunofluorescent images of Axillary TDLNs showing elevated abundance of ZsG 2 h post BH or Sham treatment co-localizing with Lyve-1 lymphatic endothelium. **B.** IF quantification for the proportion of Lyve-1 expressing endothelium co-localized with ZsG tumor antigen. (n=6-9) Unpaired t test with Welch's correction: ∗∗ $P<0.01$; ROUT Outliers analysis with Q=0.1%. Mean ± SD.

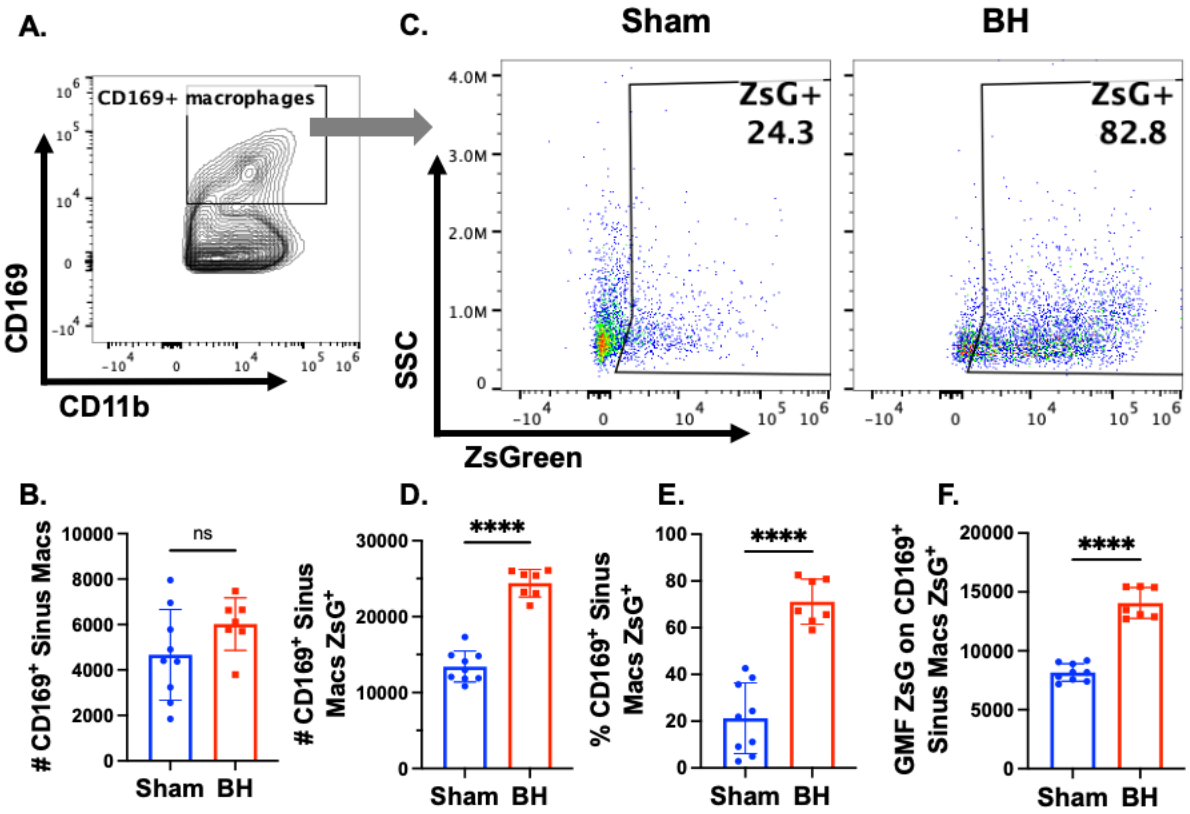

Figure 3-4. BH increases ZsG tumor antigen acquisition by CD169$^+$ LN-resident sinus macrophages. A. Representative flow plot of CD169$^+$ macrophages pre-gated on CD11b$^+$F4/80$^-$ cells in the TDLNs. **B.** Quantification of flow data for the number of CD169$^+$ sinus macrophages in the TDLNs of Sham and BH cohorts. **C.** Representative scatter plots showing ZsG presence in CD169$^+$ macrophages. Frequencies shown are of the CD169$^+$ macrophage population. **D.** Quantification of the number of CD169$^+$ sinus macrophages ZsG$^+$. **E.** Bar graph showing the proportion of CD169$^+$ macrophages that are ZsG$^+$. **F.** Quantification of the geometric mean fluorescent intensity (GMF) of ZsG on ZsG$^+$ CD169$^+$ macrophages. (n=7-9) Unpaired t test with Welch's correction: ns = non-significant, **** P<0.0001; ROUT Outliers analysis with Q=0.1%. Mean ± SD.

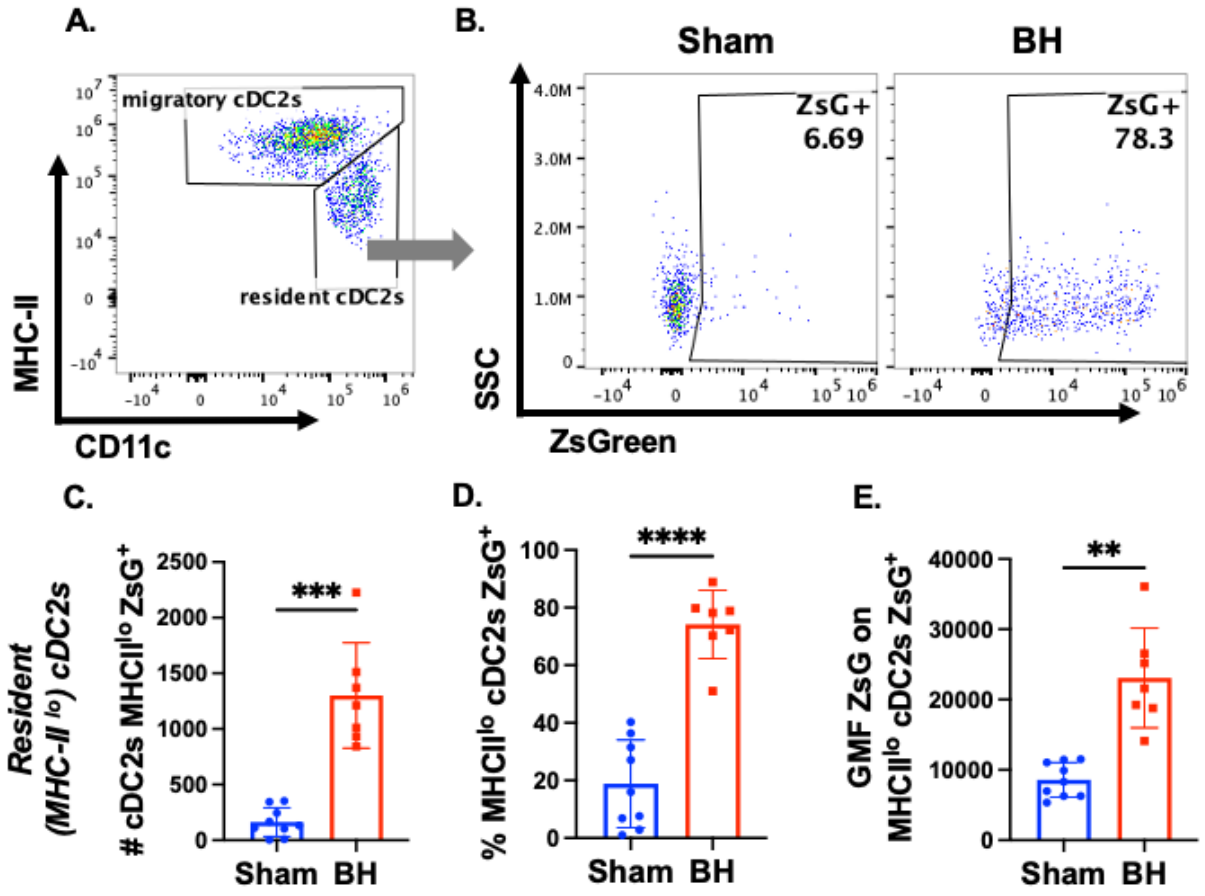

Figure 3-5. BH increases ZsG antigen presence in LN-resident (MHC-II^{lo}) cDC2s. A. Representative flow plot of migratory & resident cDC2s pre-gated on CD11c^{+}MCH-11^{+} F4/80^{-}CD11b^{+} cells in the TDLNs. **B.** Representative scatter plots showing ZsG presence in LN-resident cDC2s in Sham and BH cohorts. Frequencies shown are of the parent population. **C.** Quantification of flow data for the number of ZsG^{+} LN-resident cDC2s in the TDLNs. **D.** Bar graphs showing the proportion of LN-resident cDC2s that are ZsG^{+}. **E.** Quantification of the GMF of ZsG on ZsG^{+} LN-resident cDC2s. (n=7-9) Unpaired t test with Welch's correction: ** P<0.01, *** P<0.001, **** P<0.0001; ROUT Outliers analysis with Q=0.1%. Mean ± SD.

Boiling histotripsy does not alter CCR7 expression on cDCs

Given that the migration of cDCs from the periphery to draining lymph nodes is dependent on the chemotactic axis of the CCR7 receptor and its ligands CCL19 and CCL21[4,101] we sought out to determine whether BH impacted CCR7 expression on cDCs. If BH-induced antigen presence in the TDLNs is due to cDC migration, we might expect to observe an increase in the CCR7^{+} cDCs in the ZsG^{+} population following BH. When we examined CCR7 expression

on cDCs in the TDLNs 24 h following BH (Figure 3-6A), we found that there was no difference in the number or proportion of cDC1s or cDC2s that we $CCR7^+$(Figure 3-6B-C & F-G, respectively). We also observed no change in the GMF of CCR7 on cDC1s or cDC2s, indicating that BH is not altering the amount of CCR7 being displayed on the surface of cDCs (Figure 3-6D & H). Interestingly, the proportion of $CCR7^+$ ZsG^+ cDC1s –which from our prior work we know ZsG^+ cDC1s are significantly elevated in the BH cohort[75] – was significantly reduced after BH, and a similar trend was observed in the ZsG^+ cDC2s (Figure 3-6E & I, respectively); indicating that the increase in ZsG presence in cDCs in the TDLN is not consistent with a CCR7-dependent migration of cDCs from the treated tumor. In conjunction with our findings in the previous section – i.e. the localization of tumor antigen in the lymphatic sinuses, and the acquisition of ZsG by LN-resident cells typically enriched in areas of lymphatic endothelium – these results imply that the mode of antigen accumulation in the TDLNs post BH treatment is the result of lymphatic drainage of cell-free antigen rather than DC-mediated trafficking from the ablated tumor to the TDLNs.

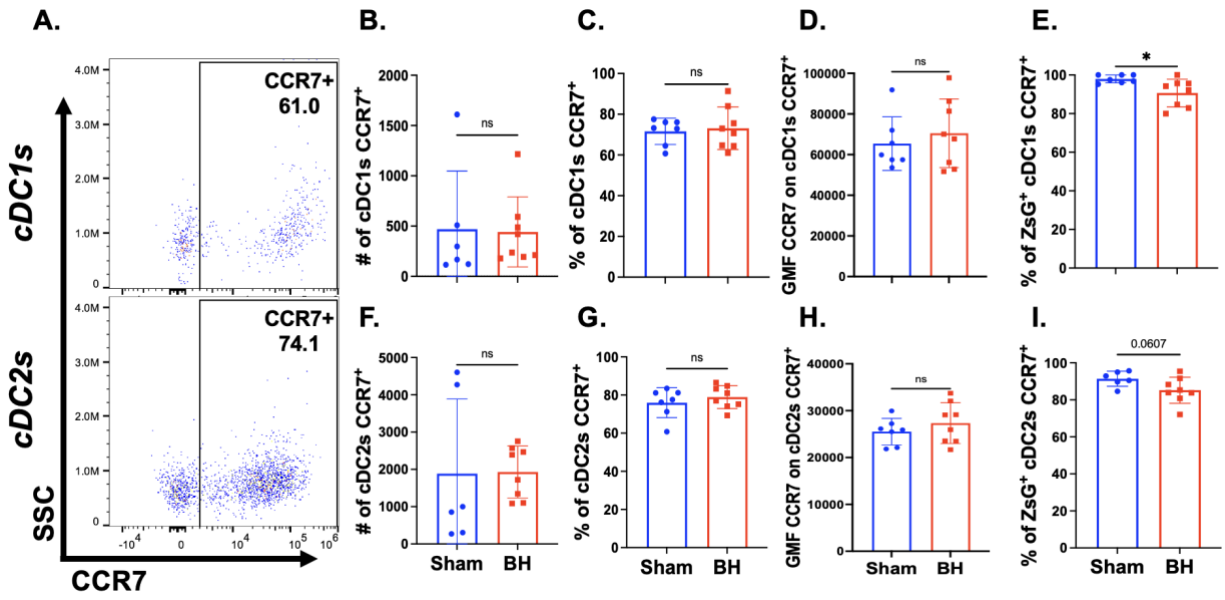

Figure 3-6. BH does not alter CCR7 expression on cDCs. A. Representative flow plots showing CCR7 expression on cDC1s (top) and cDC2s (bottom) in the TDLNs. Frequencies shown are of the parent population. **B & F.** Quantification of the number of CCR7$^+$ cDC1s (**B**) and cDC2s (**F**). **C & G.** Bar graph showing the proportion of cDC1s (**C**) and cDC2s (**E**). that are CCR7$^+$. **D & H.** Quantification of the GMF of CCR7 on CCR7$^+$ cDC1s (**D**) and cDC2s (**H**). **E & I.** Bar graph showing the proportion of ZsG$^+$ cDC1s (**E**) and ZsG$^+$ cDC2s (**I**). that are CCR7$^+$. (n=7-8) Unpaired t test with Welch's correction: ns = non-significant, ∗ P<0.05; ROUT Outliers analysis with Q=0.1%. Mean ± SD.

BH induces early phenotypic activation and trends towards increased expansion of melanoma specific CD8$^+$ T-cells

We have consistently observed that BH treatment results in a bolus of tumor antigen dissemination in the TDLNs and the upregulation of costimulatory molecules on APC that engulf the tumor antigen. This finding, in conjunction with evidence of abscopal tumor control[75], suggest that BH may enhance T-cell activation. To test this, we utilized PMEL T-cell receptor (TCR) transgenic mice that recognize the mouse homologue of human glycoprotein (hgp)-100, an antigen highly expressed by human malignant melanoma cells[105]. About 2 h prior to Sham or BH treatment, CellTrace Violet (CTV) labeled CD8$^+$ T-cells were adoptively transferred into B16-ZsG tumor-bearing mice, and TDLNs were assessed by flow cytometry 24 h post treatment

(Figure 3-7A). We distinguished the PMEL $CD8^+$ T-cells based on their expression of V-beta chain 13 (Vβ13) and the mismatched allele Thy1.1 (Figure 3-7B). The proportion of PMELs that express both the canonical activation markers CD69[106] and CD25[107] ($CD69^+CD25^{+)}$ was significantly higher in the BH cohort compared to the Sham controls (Figure 3-7C-D). Additionally, the GMF of CD69 on PMELs was significantly higher in the BH treated cohort (Figure 3-7E). Taken together, these findings indicate that BH treatment is resulting in the early activation of tumor-specific $CD8^+$ T-cells. As both cDC1s and cDC2s are capable of cross-presenting antigen to $CD8^+$ T-cells[5], we next assessed whether the increased number of phenotypically activated PMELs ($CD69^+CD25^+$) correlated with the number of tumor antigen containing (ZsG^+) cDC1s or cDC2s. We found that there is a strong correlation ($R^2 = 0.6489$) with ZsG^+ cDC1s, and a moderate correlation ($R^2 = 0.5691$) with ZsG^+ cDC2s (Figure 3-7F & G, respectively); indicating that the higher number of tumor-antigen acquiring cDCs present after BH therapy may improve the likelihood of these ZsG^+ cDCs to encounter tumor-specific $CD8^+$ T-cells.

Given that we observed elevated activation frequency of PMEL $CD8^+$ T-cells following BH therapy, we next investigated whether BH resulted in increased expansion of these T-cells in the TDLNs. We were able to distinguish divided versus undivided PMELs based on the intensity of CTV. As a dye, CTV will dilute and become less fluorescently intense as the PMELs divide. FTY720 - a sphingosine-1-phosphate receptor agonist that blocks T cell emigration from lymphoid tissues[108] – was used to prevent emigration of activated PMEL from the LNs. Each mouse was bled to confirm the efficacy of FTY720. When we examined CTV dilution on PMELs from the Sham and BH cohorts (Figure 3-8H), we found a strong trending increase in the number of PMELs that had divided in the BH TDLNs compared to the Sham controls (Figure 3-

8I). Notably, two samples in the BH group did not mirror the response of the rest of the cohort (Figure 3-8J&K, respectively). However, the qualitative B-mode imaging indicated that these tumors received comparable cavitation as the others, suggesting that limited antigen release was not responsible for the lack of PMEL response. The strong trend noted in PMEL activation argues for further studies and/or a more quantitative measurement of cavitation efficacy to fully test the hypothesis that BH treatment induces tumor-specific T-cell expansion.

This elevated phenotypic activation of the PMEL $CD8^+$ T-cells post BH is not entirely specific to the TDLNs. Although we did not detect a difference in the number or proportion of $CD69^+CD25^+$ PMELs (Figure 3-8A-B) in the non-tumor draining, contralateral LNs (cLNs; axillary & brachial LNs on the left, non-tumor-bearing side), we did observe an increase in CD69 expression on PMELs in the cLNs following BH (Figure 3-8C). However, the expression level of CD69 on PMEL was lower in the cLN compared to the paired TDLN (Figure 3-8D). Similarly, while we found that cLN PMELs in the BH cohort underwent more proliferation than the Sham controls (Figure 3-8E-G), the fluorescence intensity of CTV on PMELs in cLNs was significantly higher than that of the PMELs in their paired TDLNs (Figure 3-8H). This suggests that while tumor-specific $CD8^+$ T-cells are acutely most activated in the TDLNs, where they directly encounter antigens and DAMPs released by BH-, there is some systemic PMEL activation resulting from BH treatment. This systemic effect is independent of tumor antigen accumulation post BH as we have previously shown BH does not increase ZsG presence in cLNs[75]. More direct experiments would have to be conducted to definitively assess the functional capabilities of the PMEL $CD8^+$ T-cells activated in non-draining lymph nodes.

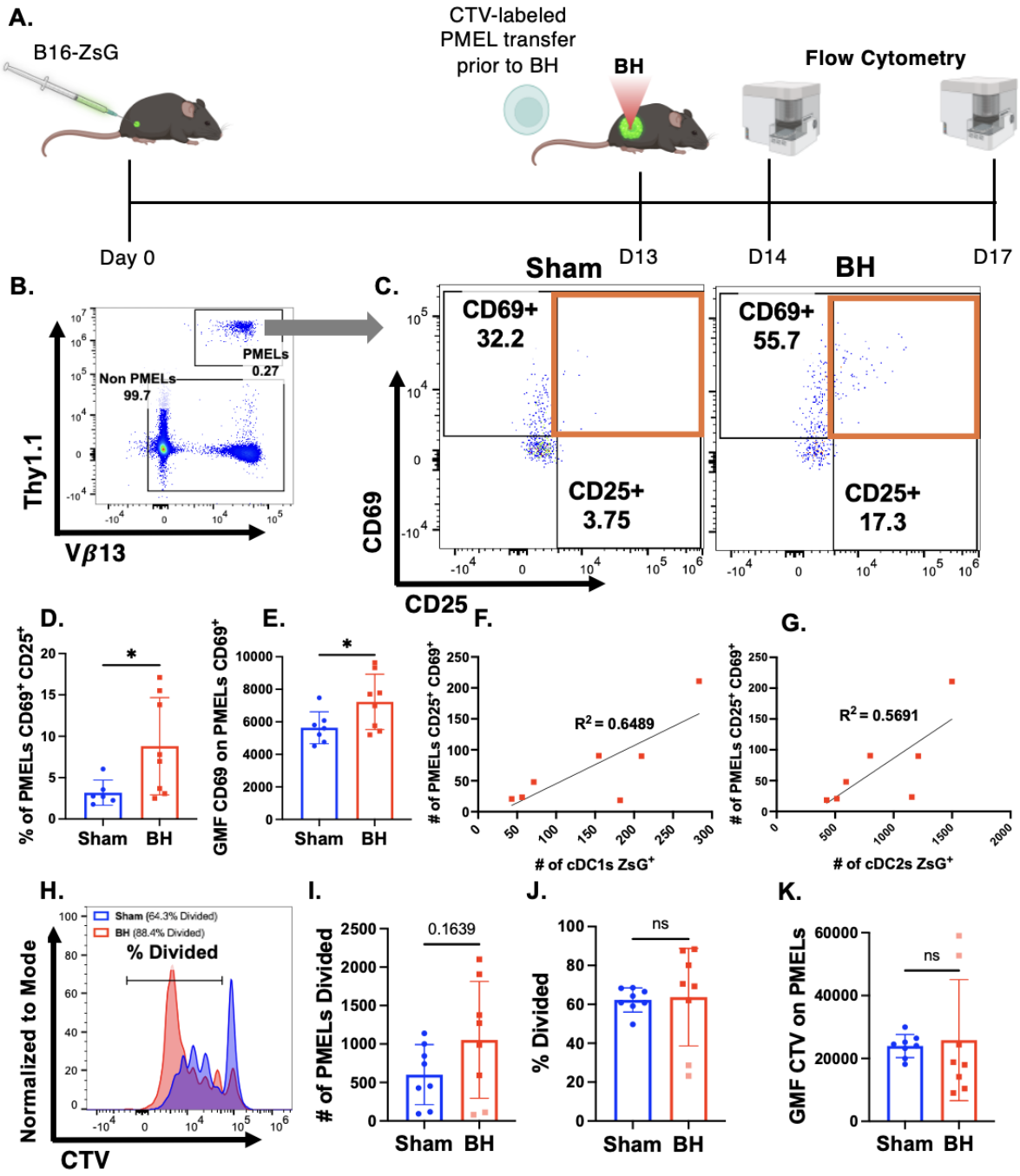

Figure 3-7. BH induces early phenotypic activation and trends towards increased expansion of melanoma specific CD8⁺ T-cells restricted to the TDLNs. A. Schematic for experimental timeline from tumor initiation to PMEL CD8⁺ T-cell transfer preceding BH or Sham treatment followed by 24 h (d14) and 96 h (d17) flow cytometry analysis. **B.** Representative flow plot of PMEL TCR transgenic T-cells (Thy1.1⁺Vβ13⁺) & endogenous "Non-PMEL" CD8⁺ T-cells pre-gated on CD3⁺CD8⁺ cells in the TDLNs. Frequencies shown are of the parent population. **C.** Representative flow plots showing CD69 and CD25 expression on PMELs in Sham and BH cohorts 24 h post treatment. Frequencies shown are of the parent population. **D.** Bar graph showing the proportion of PMELs that are CD69⁺CD25+ at 24 h timepoint. **E.** Quantification of the GMF of CD69 on CD69⁺ PMELs at 24 h. **F&G.** Linear regression correlation between the number of CD69 ⁺CD25 ⁺ PMELs and the number of ZsG⁺ cDC1s **(F)** or ZsG⁺ cDC2s **(G)** at the 24 h timepoint. **H.** Histogram showing CTV staining on PMELs 96 h post BH or Sham treatment. **I**. Bar graph showing the number of PMELs that had divided by the 96 h timepoint. **J.** Bar graph showing the proportion of PMELs that had divided by 96 h**. K.** Quantification of the fluorescence intensity of CTV on the PMELs at 96 h. (n=7-8) Unpaired t test with Welch's correction: ns = nonsignificant, ∗ P<0.05; Mean ± SD **(D-E, I-K)**. Simple linear regression model **(F&G)**. ROUT Outliers analysis with Q=0.1%.

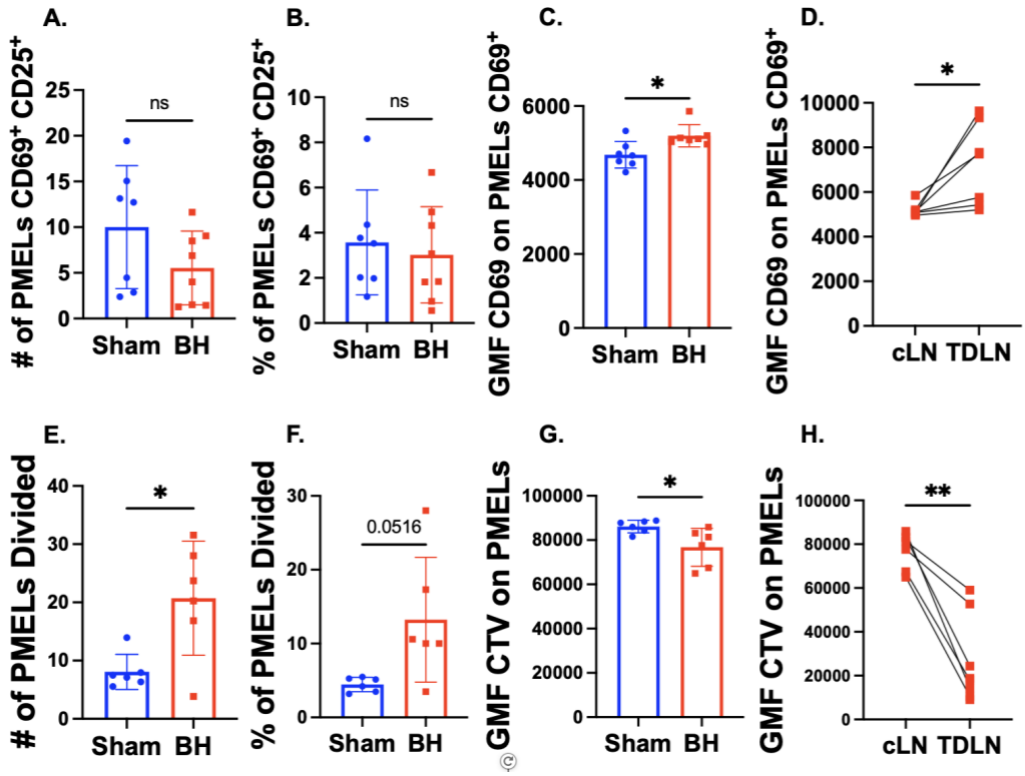

Figure 3-8. BH-induced activation and expansion of PMEL CD8$^+$ T-cells is also observed, to a lesser degree, in cLNs. A. Quantification of the number of PMELs that are CD69$^+$CD25$^+$ in the non-tumor draining, contralateral LNs (cLNs; Axillary & Brachial LNs on the left, non-tumor-bearing side). **B.** Bar graph showing the proportion of PMELs in the cLNs that are CD69$^+$CD25$^+$. **C.** Quantification of the GMF of CD69 on CD69$^+$ PMELs in the cLNs. **D.** GMF CD69 on CD69$^+$ PMELs from paired cLN and TDLNs. **E.** Bar graph showing the number of PMELs in the cLNs that had divided by the 96 h timepoint. **F.** Bar graph showing the proportion of PMELs that had divided by 96 h. **G.** Quantification of the fluorescence intensity of CTV on the PMELs at 96 h. **H.** GMF CTV on PMELs from paired cLN and TDLNs. (n=6-8) Unpaired t test with Welch's correction: ns = nonsignificant, ∗ P<0.05; Mean ± SD **(A-C & E-G).** Paired t test: ∗ P<0.05, ∗∗ P<0.01 **(D&H).** ROUT Outliers analysis with Q=0.1%.

Impeding cDCs migration does not hinder antigen acquisition or tumor-specific T-cell expansion

We have shown that mechanically ablating melanoma tumors with BH acutely leads to the accumulation of tumor antigen in the TDLNs. In the Sham (steady-state), the presence of tumor-antigen in the TDLNs is dependent on cDC migration via the CCR7 chemotactic axis[4].

Because cDCs have been observed to traffic to the draining LNs as early as 16 h following a mechanical insult[109], we tested whether BH-induced antigen presence in the TDLNs requires cDC migration. Given that we found no changes in CCR7 expression on cross-presenting cDC1s or cDC2s following BH (Figure 3-6), and that most of the ZsG antigen post BH appears to localize to the lymphatic sinuses (Figure 3-3), we hypothesized that CCR7-mediated cDC trafficking is not necessary for BH-induced tumor antigen deposition in the TDLNs. To test this, we utilized an anti-CCR7 blocking antibody to impede cDC migration. Following the 3-dose regimen of 10 μg/dose displayed in Figure 3-10A, we found that **α**CCR7 effectively reduced the number and proportion of migratory cDC1s and cDC2s in the TDLNs (Figure 3-9A-F), while not impacting the number of LN-resident cDCs (Figure 3-9G&I). While decreases in both migratory cDC subsets was observed, as expected **α**CCR7 treatment had a more profound reduction on the migratory $CD103^+$ cDC1s compared to the $MHC\text{-}II^{hi}$ cDC2s (Figure 3-9C&E). When we performed pairwise analysis on CCR7-expressing cDC1s and cDC2s within the same TDLNs, we found that cDC1s express significantly more CCR7 than the cDC2s. Therefore, we hypothesize that the differential effects of CCR7-blockade could be due to different amounts of CCR7 displayed on the surface of cDC1s versus cDC2s.

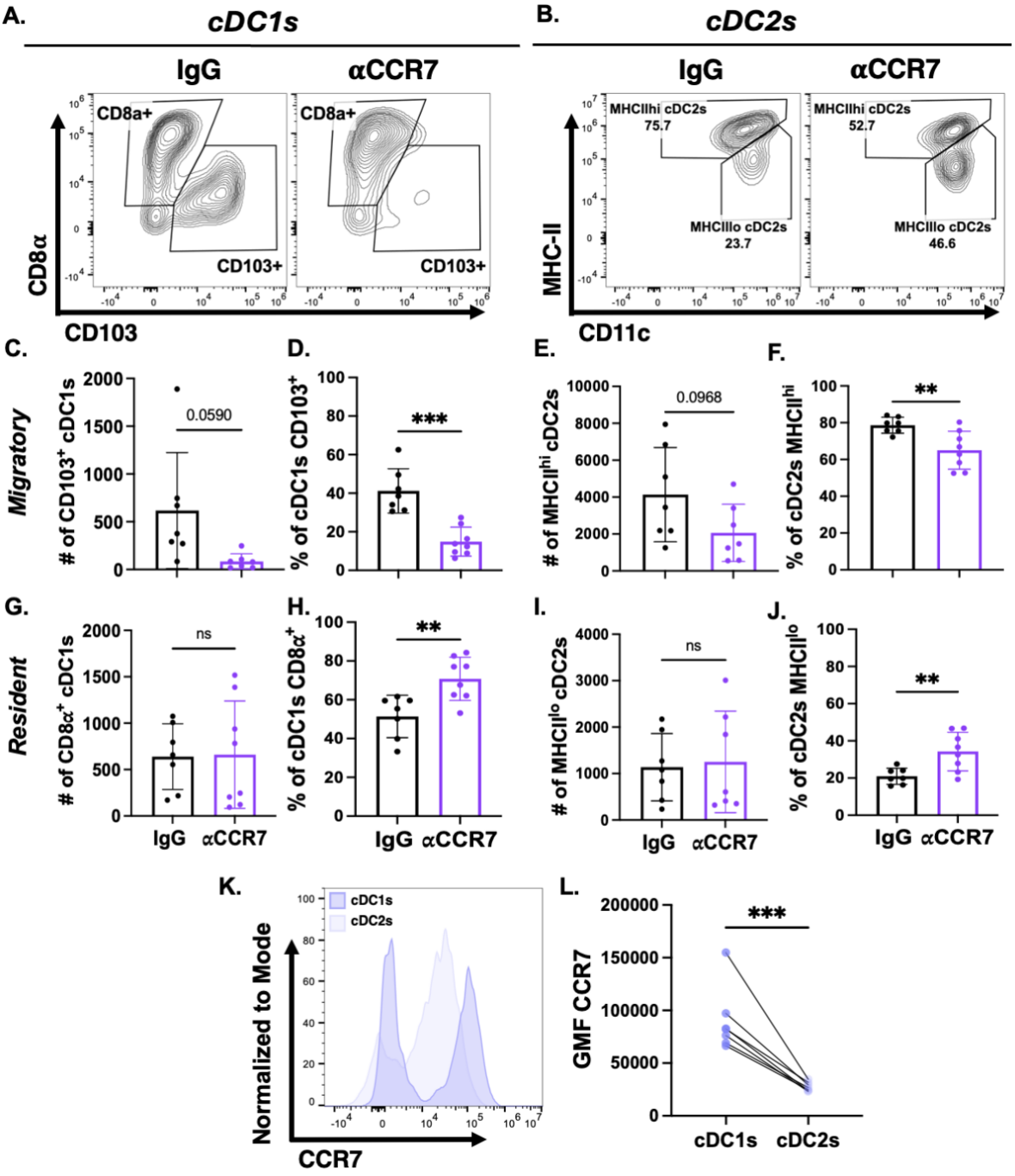

Figure 3-9. αCCR7 effectively reduces migratory cDC presence in TDLNs – predominately cDC1s – without impacting LN-resident cDC. A. Representative flow plots of migratory ($CD103^+$) & LN-resident ($CD8\alpha^+$) cDC1s after **α**CCR7 or isotype control IgG administration; pre-gated on $CD11c^+MCH\text{-}11^+$ $F4/80^-XCR1^+$ cells in the TDLNs. **B.** Representative flow plots of migratory ($MHC\text{-}II^{hi}$) & resident ($MHC\text{-}II^{lo}$) cDC2s after **α**CCR7 or IgG administration; pre-gated on $CD11c^+MCH\text{-}11^+$ $F4/80^-CD11b^+$ cells in the TDLNs. **C&E**. Quantification for the number of migratory cDC1s **(C)** or cDC2s **(E)**. **D&F**. Bar graphs showing the proportion of cDC1s **(D)** or cDC2s **(F)** that are migratory. **G&I**. Quantification for the number of LN-resident cDC1s **(G)** or cDC2s **(I)**. **H&J**. Bar graphs showing the proportion of cDC1s **(H)** or cDC2s **(J)** that are LN-resident. **K.** Histogram showing CCR7 expression on cDC1s and cDC2s in steady-state LNs. **L.** GMF CCR7 on paired $CCR7^+$ cDC1s and $CCR7^+$ cDC2s. (n=7-8) Unpaired t test with Welch's correction: ns = nonsignificant, ** $P<0.01$, *** $P<0.001$; Mean ± SD **(C-J).** Paired t test: *** $P<0.001$ **(L).** ROUT Outliers analysis with Q=0.1%.

We thus tested whether preventing cDC migration would impact tumor antigen presence in cDCs post BH. 3-doses of αCCR7 were administered prior to BH or Sham treatment (Figure 3-10A). In the face of CCR7-blockade, BH still resulted in an increase in the proportion of migratory and LN-resident cDCs that contain ZsG tumor antigen (Figure 3-10B-D). This demonstrates that the tumor antigen bolus observed in the TDLNs acutely post BH is independent of CCR7-mediated cDC trafficking of antigen from the TME. To understand whether cDC migration is required for PMEL expansion that we had observed after BH (Figure 3-7H-K), CTV labeled PMEL $CD8^+$ T-cells were adoptively transferred in prior to Sham or BH (Figure 3-11A). Utilizing the dilution of CTV as a proxy for PMEL proliferation, we assessed PMELs that had and had not undergone division (Figure 3-11B), and we observed that even in the presence of αCCR7 blockade, a significantly greater number and proportion of PMELs underwent division when comparing the BH cohort to the Sham controls (Figure 3-11C&F). This notion was also verified by the significant reduction in the GMF of CTV on PMELs isolated from BH TDLNs (Figure 3-11E) – suggesting that more of these T-cells had proliferated. Surprisingly, when we examined the number of PMELs that had not undergone division (i.e not activated), we found that there was no difference between the Sham and BH groups. This implies that rather than T-cell activation and expansion post BH being the result of increased antigen presence in the TDLNs, it may be that the quality of the tumor antigen is enhanced by BH. Although we are observing an increase in tumor antigen acquiring cDCs following BH, there is an equal number of non-divided, not activated PMELs post BH compared to the Sham cohorts. Therefore, the increase PMEL activation observed post BH may be the result of these T cells encountering cDCs that have engulfed and presented a more immunogenic antigen brought about by the mechanical ablation. This hypothesis requires future studies to directly test and assessing

whether BH treatment alters the immunogenicity of ZsG antigen is an active area we are currently pursuing. In all, these findings suggest that the bolus of tumor observed in the TDLNs following mechanical destruction with BH is the result of passive drainage of antigen from the TME, which can induce tumor-specific T-cell expansion independent of cDC migration.

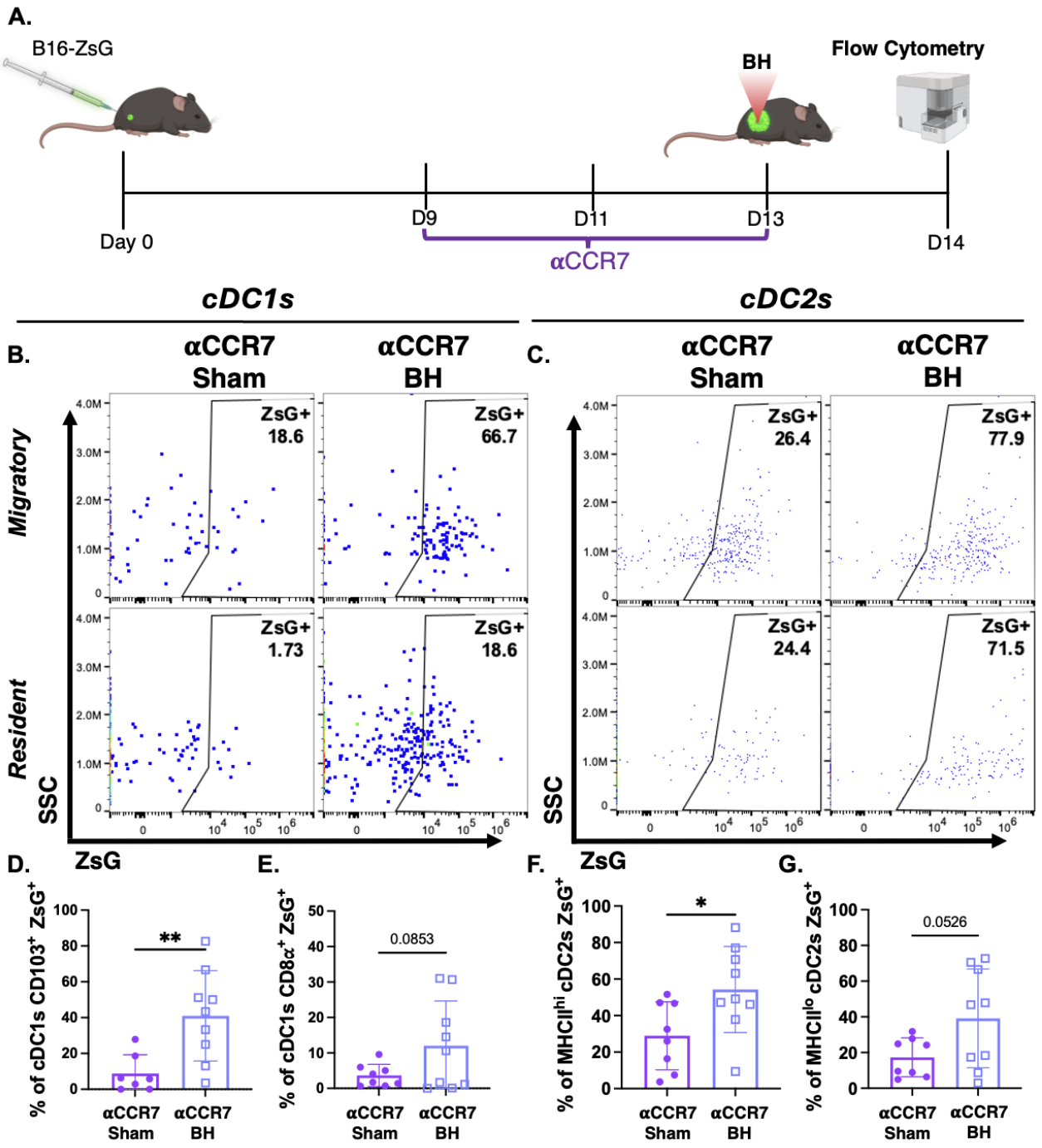

Figure 3-10. Increased antigen acquisition by migratory and LN-resident cDCs was still observed post BH in the presence of αCCR7 blockade. A. Schematic for experimental timeline from tumor initiation to **α**CCR7 blockade preceding BH or Sham treatment followed by 24 h flow cytometry analysis of the TDLNs. **B.** Representative flow plots of ZsG presence in migratory (top) and LN-resident (bottom) cDC1s. Frequencies shown are of the parent population. **C.** Representative flow plots of ZsG presence in migratory (top) and LN-resident (bottom) cDC2s. Frequencies shown are of the parent population. **D&E**. Bar graphs showing the proportion of migratory **(D)** or resident **(E)** cDC1s that are ZsG^+. **F&G**. Quantification for the proportion of migratory **(F)** or resident **(G)** cDC2s that are ZsG^+. (n=8-9) Unpaired t test with Welch's correction: ∗ $P<0.05$; Mean ± SD**.** ROUT Outliers analysis with Q=0.1%.

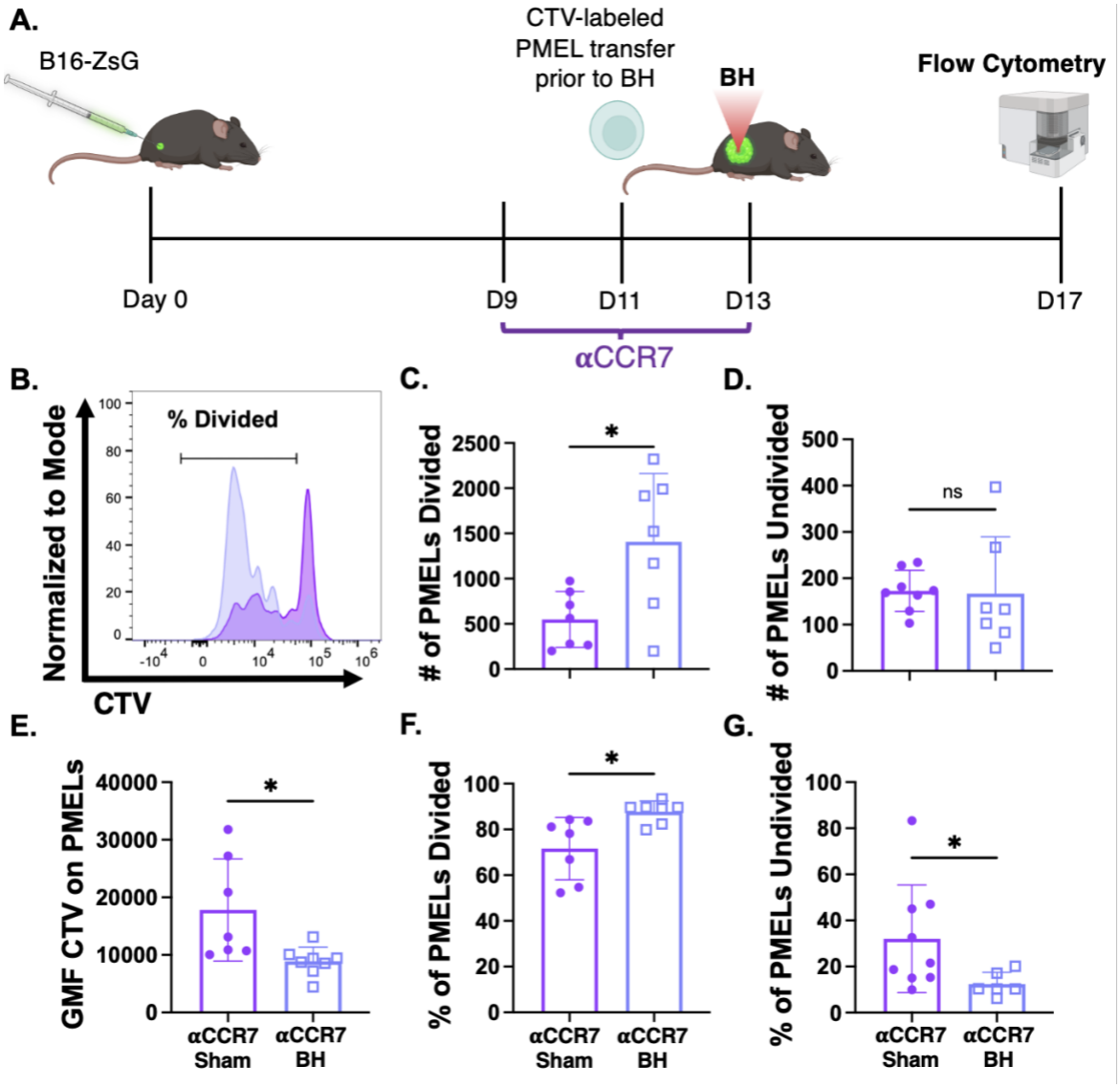

Figure 3-11. αCCR7 blockade does not hinder BH-induced tumor-specific T-cell expansion. **A**. Schematic for experimental timeline from tumor initiation to **α**CCR7 blockade, to PMEL $CD8^+$ T-cell transfer preceding BH or Sham treatment followed by 96 h flow cytometry analysis of the TDLNs. **B.** Histogram showing CTV staining on PMELs 96 h post **α**CCR7 blockade+BH or **α**CCR7 blockade+Sham treatment. **C&D**. Bar graphs showing the number of PMELs that had divided **(C)** or not divided **(D)**. **E.** Quantification of the fluorescence intensity of CTV on the PMELs at 96 h. **F&G**. Bar graphs showing the proportion of PMELs that had divided **(F)** or not divided **(G)**. (n=7-8) Unpaired t test with Welch's correction: ns = nonsignificant, ∗ $P<0.05$; Mean ± SD**.** ROUT Outliers analysis with Q=0.1%.

A repeat of the activation and enhanced proliferation observed post BH was attempted, however, no difference in phenotypic activation or expansion of the T-cells between the Sham

and BH cohorts was detected. However, we encountered confounding factors that may have impeded BH-induced PMEL activation. For most of these studies, we utilized PMEL mice that were around 2 months in age, but for this repeat, we had isolated $CD8^+$ T-cells isolated from PMELs that were 10 months in age. we observed no difference in phenotypic activation or expansion of the T-cells between the Sham and BH cohorts. It is known that T-cells from 10-month-old mice are metabolically deficient and carry out reduced cytolytic functions upon TCR stimulation compared to younger T-cells 2-month-old[110]. This could explain the lack of response to BH-stimulus. Nonetheless, these aged T-cells are not anergic, as they can still respond in the positive control setting of anti-CD40, poly:ICLC and gp100 vaccination. This suggests that the older T-cells may need a more potent stimulation and stronger interaction with cDCs to become activated. Previously, we have shown that even though BH increases the activation status of cDCs in the TDLNs, this activation and upregulation of CD86 is to a much lesser degree than that induced by the immunostimulant polyI:CLC[75] – a mimic of the DAMP double-stranded RNA. In addition, the effects of PMEL activation status at 24 h only reproduced in the absence of FTY720. This is not entirely surprising given that FTY720 has been shown to hinder T-cell activation and effector function[111–113]. Similarly, vaccination was able to overcome activation suppression by FTY720. Altogether, while these experiments did not recapitulate previous findings of BH-induce effects on tumor-specific T-cells, they do shed light on a limitation of this therapy and the potential for combinatorial treatment regimens, potentially with TLR stimulation, to further enhance cDC activation so that a more consistent and optimal T-cell response is obtained.

DISCUSSION

While we had previously established that mechanical ablation via BH acutely induces the dissemination of tumor antigen to the TDLNs, it was unknown where within the LNs this antigen accumulated and how the antigen was transported to the TDLNs. This information is important when considering BH's role as a cancer therapeutic as the cells that acquire and present antigen to T cells are intrinsically influential in the subsequent T cell response. Understanding which cDC subset is best positioned to acquire antigen post BH, whether these antigen-positive cDCs undergo sufficient activation to be able to successfully cross-present tumor antigen to $CD8^+$ T-cells, and whether BH treatment can bypass cDC trafficking of tumor antigen to the TDLNs would provide fundamental and novel knowledge about BH-induced immunity.

By utilizing IF microscopy, we were able to visualize the spatial distribution of ZsG tumor antigen in the TDLNs following BH – providing the first evidence of liberated antigen concentrating around the periphery of the LNs post treatment, colocalizing with the lymphatic sinus endothelium (Figure 3-3). This notion was further substantiated when we examined ZsG presence in subcapsular $CD169^+$ macrophages and LN-resident cDC2s, which are enriched in these lymphatic sinus regions[6,103] (Figures 3-4 &3-5). In the B16-ZsG model, the engulfment of ZsG by cDCs has previously been associated with the concomitant engulfment of shared melanoma antigens gp100 and tyrosinase[9]. As gp100 and tyrosinase proteins both exceed 70 kDa, we would predict that if these antigens were cell-free and passively draining to the TDLNs post BH, they would localize around the periphery of the LN as they would be too large to enter the conduit network. This is consistent with our IF staining. ZsG is 26 kDa, therefore, on its own, it could diffuse deep within the LNs. The fact that majority of the fluorescent protein remains

confined to the lymphatic sinuses suggests that ZsG is acting as model tumor antigen – arriving as particular matter, potentially coupled with larger proteins.

We also considered the immunogenicity of a disseminated bolus of antigen on tumor-specific T-cells in the TDLN by examining the phenotypic activation state and expansion of PMEL $CD8^+$ T-cells post BH. We found that mechanical ablation via BH results in increased activation status of PMELs (Figure 3-7D-E), which correlates with the number of tumor antigen positive cDC1s and cDC2s (Figure 3-7F&G, respectively). While cDC1s are known to directly cross-present antigen to $CD8^+$ T-cells, cDC2s have only thought to do so in the context of antigen-antibody complexes or soluble antigen[5]. Additionally, this acquisition of tumor cell antigen by subcapsular $CD169^+$ macrophages may be critical for the initiation of a $CD8^+$ T-cell response, as these cells have been shown to be required for $CD8^+$ T-cell priming with antigens derived from dead cells[104]. In the future, to confirm which of these APCs are best able to elicit tumor-specific T-cell activation and expansion after BH, we will sort these APC subsets from the TDLNs of BH-treated mice, and co-culture them with PMEL or tyrosinase-related protein 2 (TRP-2) $CD8^+$ T-cells to determine which APC can cross-present to the T cells. In addition, we can test whether BH-induced PMEL activation is dependent on cDCs and/or subcapsular macrophages by utilizing genetic models – $Zbtb46^{dtr}$ and $CD169^{dtr}$ mice, respectively. Zinc finger and BTB domain containing 46 (Zbtb46) is a transcription factor selectively expressed by cDCs and their committed progenitors[114], while CD169 is selective for subcapsular macrophages. These populations can be eliminated with the administration of diphtheria toxin in these murine models. Moreover, because the LN is a complex and organized network of various immune cell subsets, there may be overlap or interplay in eliciting $CD8^+$ T-cell activation across subsets. For instance, if subcapsular macrophages are required for T-cell activation induced by

BH therapy, is that due in part to follicular B-cells? Positioned at the edge of the B-cell follicles, subcapsular macrophages can present antigen to follicular B-cells, which can then carry antigen to the B-cell/T-cell border within the LN (Carrasco). We have previously reported B-cells acquiring a significant amount of ZsG tumor antigen – more so than any other APC subset – in the TDLNs post ablation with BH. Therefore, future studies will also need to be performed to address the importance to subcapsular macrophages and B-cell antigen handoff in BH-induced immunity and the role of immune complexes in directing antigen to cDC2s.

Mechanical ablation has been shown to elicit anti-tumorigenic immune responses[75,79,81], and in some contexts, $CD8^+$ T-cell presence was elevated in treated and abscopal tumors. This is in line with our observation of PMEL activation and proliferation in the cLNs of the BH cohort (Figure 3-8). Because we did not detect the presence of ZsG tumor antigen within the cLNs post BH, we hypothesize that the PMELs seeding these LNs may be responding to endogenous self-antigen present derived from melanocytes – not just those that have undergone malignant transformation. The inflammatory nature of BH may be releasing PAMPs and DAMPs that enter circulation and could be inducing the systemic activation. However, the degree of phenotypic activation of the PMELs residing in the cLNs is far lower than that of the PMELs in the TDLNs (Figure 3-8D&H). Future studies, such as killing assays taking the PMELs sorted from cLNs or TDLNs and coculturing them with the B16-ZsG, are needed to determine if there is a functional difference between these PMEL populations.

If BH is inducing systemic tumor-specific T-cell activation, why are the effects of tumor growth control and lengthened survival not sustained? Maybe these activated T-cells are not making their way into the tumors following mechanical ablation. This would occur if the vasculature were not compatible with T-cell infiltration[115]. Alternatively, if the activated T-cells

were infiltrating into the tumor, they may be becoming exhausted due to the immunosuppressive TME and chronic antigen stimulation. Given that the trafficking of tumor antigen by cDCs from the TME to the TDLNs is normally dependent on the chemotactic axis of the CCR7 receptor and its ligands, CCL19 and CCL21[4,101], we needed to impede the CCR7 axis to inhibit cDC trafficking without perturbing LN-resident cDC subsets to determine the mode of antigen accumulation in the TDLNs following BH. We were able to achieve this by administering three doses of **α**CCR7 blocking antibody (Figure 3-9). When given prior to BH treatment, we found that BH still resulted in increased proportions of both migratory and LN-resident cDCs engulfing ZsG tumor antigen even with **α**CCR7 inhibiting cDC trafficking (Figure 3-10). Additionally, we still observed PMEL expansion in the BH cohorts even in the presence of **α**CCR7 blockade (Figure 3-11). These finding suggest that the tumor antigen bolus observed in the TDLNs post BH is independent of CCR7-mediated cDC trafficking from the TME, and cDC trafficking is not required to elicit tumor-specific T-cell expansion following BH. This indicates that LN-resident cells are capable of initiating adaptive immune activation in response to mechanical insult of a subcutaneous tumor, which results in the liberation cell-free antigen, bypassing the traditional mode of cDC-mediated presentation of antigen from the periphery to secondary lymphoid structures However, we acknowledge the approach used here to impede cDC migration does have technical caveats. Although **α**CCR7 significantly reduced the number of migratory cDCs, some of these cells remain. To confirm these findings, a genetic approach should be taken to eliminate migratory cDCs entirely, and test whether ZsG antigen is observed in the TDLNs post BH in the complete absence of migratory cDCs. We did attempt a study of antigen trafficking in $CCR7^{-/-}$ mice, which are devoid of migratory cDCs[4], and we found no difference in ZsG presence in the TDLNs of $CCR7^{-/-}$ Sham and $CCR7^{-/-}$ BH cohorts. However, upon harvesting of

the TDLNs, we noticed that the CCR7$^{-/-}$ LNs were physically smaller than aged matched C57Bl/6 wildtype (WT) mice, and fewer PMELs seeded into the CCR7$^{-/-}$ TDLNs when compared to the WT TDLNs. In addition, CCR7$^{-/-}$ mice have been shown to have increased fibrosis and collagen build-up along their lymphatic vessels and walls. This results in reduced lymphatic flow and increased vessel permeability[116]. Therefore, the whole body CCR7$^{-/-}$ model does not allow us to distinguish whether reductions in ZsG antigen presence in the TDLNs are the result of loss of cDC migration or defects in lymphatic vasculature. It is just as likely that we did not observe a bolus of ZsG antigen to the TDLNs post BH in this model due to impeded lymphatic drainage rather than the loss of migratory cDCs. Because of these limitations, we are proposing the development of mixed bone marrow chimera (BM) mice, equal parts CCR7$^{-/-}$: Zbtb46^{dtr}. By utilizing BM from the Zbtb46^{dtr} mice, we can ensure presence of a complete immune system with CCR7-expressing cDCs during animal development and tumor progression. Then prior to BH treatment, diphtheria toxin will be administered to deplete cDCs derived from Zbtb46^{dtr} BM – thus leaving behind only CCR7 $^{-/-}$cDCs[117].

In conclusion, our findings demonstrate that mechanically ablating melanoma tumors with BH results in the liberation and drainage of cell-free antigen to the TDLNs, where it localizes to the lymphatic sinuses. CCR7-mediated cDC migration is not responsible for the bolus of antigen observed following BH, nor the tumor-specific T-cell expansion that occurs post treatment. While we have described evidence of PMEL activation and expansion post BH as well as slight abscopal control of the B16ZsG model[75], BH as a monotherapy is not curative. Here, we have identified areas of potential intersection with combinatorial immune-based therapies. While we consistently see an enhanced upregulation of costimulatory molecules on cDCs that have engulfed tumor antigen after BH, indicative of their activation, the variability in PMEL

stimulation suggests that this is an area of improvement to better leverage the efficacy of BH. One explanation may come from the discrepancies in the immunological consequences observed in studies where BH-induced primary tumor control is either achieved or not. This will be expanded on in the following chapter.

Chapter Four: The effects of boiling histotripsy on antigen acquisition and activation of antigen presenting cells in the melanoma tumor microenvironment.

INTRODUCTION

In the previous chapter, as well as prior published work[75], we determined that BH increases tumor antigen presence in the TDLNs acutely, and that the tumor-derived antigen is acquired by cDCs and associated with cDC activation. However, we did not understand how BH was impacting the presence of APCs and acquisition of tumor-derived antigen in the TME itself shortly after treatment, and the duration of any such effects of BH. This information is crucial for our knowledge of why BH as a monotherapy is not curative. Earlier we highlighted the prognostic implications of immune cell subsets in tumors. For instance, dendritic cell signatures are associated with longer patient survival[118], while macrophage presence in early-stage melanoma is linked to reduced survival time[119]. Additionally, it has been suggested that to stimulate a robust $CD8^+$ T-cell adaptive immune response against a tumor, cDCs in the TME are required to provide a secondary co-stimulation signal to the T-cells[11]. Therefore, understanding how BH is impacting these APCs will provide insight into whether APC activation and/or their phagocytic potential following BH are rate limiting steps of the Cancer Immunity Cycle – hindering a robust antitumoral immune response. While others have assessed immune cell presence in tumors at various timepoints following mechanical ablation[79,81,120,121], no one has examined tumor antigen liberation and acquisition by APCs in the TME. Examining whether antigen is being sequestered by suppressive phagocytic cells in the TME post BH, or acquired by cDCs in melanoma tumors, and if cDCs in this environment are more tolerogenic and suppressed

– making them less capable of being activated even if they have engulfed tumor antigen – are what he sought to define.

Here, we compared the immunological consequences of BH-induced tumor debulking of murine melanoma in situations where tumor control was or was not initially achieved by BH. We found that the efficacy and destructive nature of BH acutely impacts the immune compartment within the TME. In the tumors where outgrowth was inhibited, significant reductions were observed in APC subsets – including cDC1s, cDC2s, and macrophages – while no differences in APC presence was seen in the non-debulked setting. The debulking phenotype was also associated with increased ZsG antigen acquisition, and elevated cDC1 activation, while tumors that received mechanical ablation that did not constrain tumor growth favored cDC2 activation. Altogether, these findings suggest that the parameters of the sound waves being used to induce BH and mechanical destruction of solid tumors could be tuned to better elicit cDC1: $CD8^+$ T-cell activation, which may prove beneficial in promoting adaptive immune-mediated control of tumors.

RESULTS

Conserved BH parameters does not lead to consistent debulking of primary, subcutaneous melanoma tumors

We have previously reported that BH induces tumor antigen dissemination to the TDLNs, enhances antigen acquisition and activation of cDCs in the TDLNs, and antigen presence in TDLN is independent of cDC migration from the TME to the TDLNs[75]. Here, we performed studies to understand whether tumor antigen acquisition was unique to the TDLNs, and/or whether cDCs and other APCs such as macrophages were responding to the mechanical insult

and bolus of antigen present in the TME following BH. To begin addressing these unknowns, we examined the effects of BH on B16-ZsG melanoma tumors using conserved FUS parameters [Operational frequency (f_0 = 2.5 MHz); peak-negative pressure (PNP = -21 MPa); pulse length (3 ms); pulse repetition frequency (PRF = 4 Hz); sonication time = 10 s/point; treatment spacing = 1 mm; plane separation = 2 mm] (Figure 4-1A). It is of note that in our prior publication[75], we were using a different treatment transducer with an operational frequency of 3.8 MHz. This transducer has since been replaced, and all the subsequent studies presented here utilized this new transducer. Although the tumor model remained consistent and the average tumor volumes on the day of BH treatment (day 13) across experiments was comparable (Figure 4-1B&D, C&E), we observed discrepancies in the level of tumor-debulking following the BH regimen. While all four of these studies were performed within one year of each other, we noticed that half of the experiments resulted in near significant tumor growth differences between BH and Sham cohorts (Figure 4-1B&C), while the other two studies resulted in no difference in outgrowth (Figure 4-1D&E). The outgrowth curves do not extend past day 17 because these cohorts were all euthanized for flow cytometry analysis. While the ablative regimen we used for BH treatments is only partially ablative – intending to ablate 20-40% of the tumor, leaving the majority of the tumor tissue viable – it was striking to observe very different effects on primary tumor growth. Additionally, we tested whether B-mode imaging assessment of BH-induced cavitation within the treated tissue provided an indication of whether tumor debulking would be likely to occur as we hypothesized that treatment intensity would correlate with constrain of BH-treated tumor outgrowth. Utilizing Cavitation Scoring – a qualitative metric developed by previous master student Mariia Stepanechko and senior scientist Matthew DeWitt to assess the efficacy of BH treatment via B-mode imaging by monitoring the formation of hyperechoic

lesions – we found that the debulking phenotype does correlate with higher cavitation detection. In the studies where no evidence of tumor control was observed, there was less detectable tissue destruction by B-mode. However, this is a qualitative and subjective measurement. Upon harvesting and physical analysis of the tumors 24 h post BH or Sham treatment, it was evident which tumors received FUS, and which were the Sham controls. Therefore, while the Cavitation Scoring system allows us to begin assigning a metric for BH-induced tissue destruction, future work remains to be done to develop a quantitative measurement ensuring endogenous bubble formation and implosion by BH that is required for tissue fractionation[97].

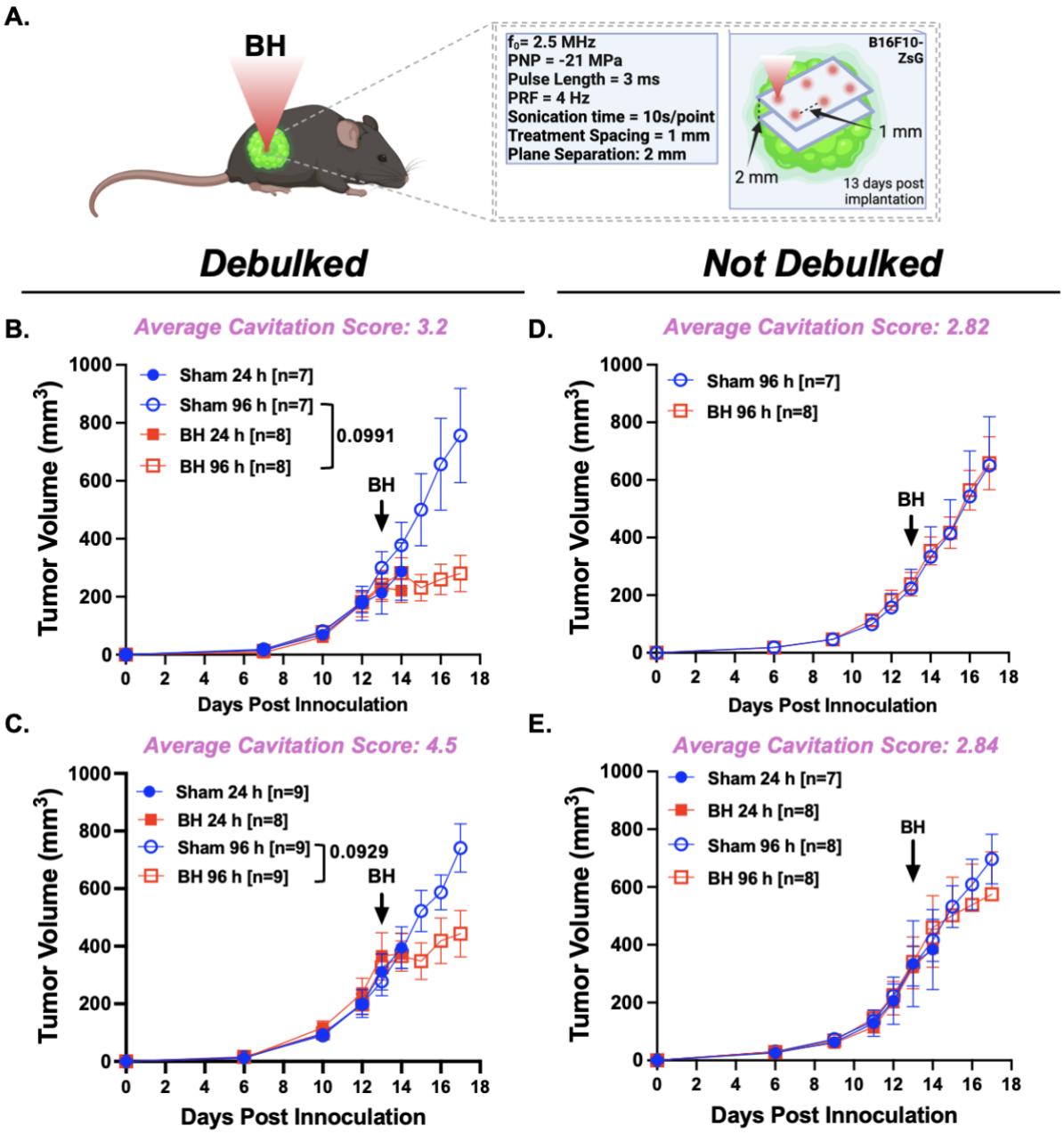

Figure 4-1. Utilizing conserved BH parameters does not lead to consistent debulking of primary, subcutaneous melanoma tumors. A. Schematic for conserved boiling histotripsy treatment parameters. **B-D.** Average tumor growth curves for B16-ZsG tumor-bearing mice treated with Sham or 1mm-spaced BH on day 13 from four separate experiments within a 1-year period. 24 h and 96 h denote harvest timepoints post BH treatment in which these cohorts were taken down for subsequent analysis. (Mixed-effects model; statistics comparing averages on day 17) All points represent mean ± SEM.

The debulking phenotype is associated with reduced APC presence acutely in the TME

As previously discussed, the presence of immune cell subsets in melanoma can have prognostic implications[16,17,118]. Given that we noticed differences in the effectiveness of BH at inducing primary tumor control, we next wanted to understand whether the level of debulking resulted in alterations to the immune cell presence in the TME. When we examined B16-ZsG tumors 24 h post BH or Sham treatment (Figure 4-2A-E), we found that in the debulked setting, when tumor control was observed, there was a significant reduction in the number and the proportion of cDC1s, cDC2s, and macrophages (Figure 4-2F-G, J-K, N-O). However, no reduction or difference was observed between Sham and BH cohorts in the experiments where debulking was not evident (Figure 4-2 H-I, L-M, P-Q). Interestingly, in both mechanically ablated settings, when we examined the tumors 96 h post treatment, there was no difference in cDC1, cDC2, or macrophage presence in the TME when compared to the Sham controls (Figure 4-3) – suggesting that these APCs are quickly able to repopulate the TME in the debulked setting. Together this data indicates that the efficacy and destructive nature of BH acutely impacts the immune compartment within the TME.

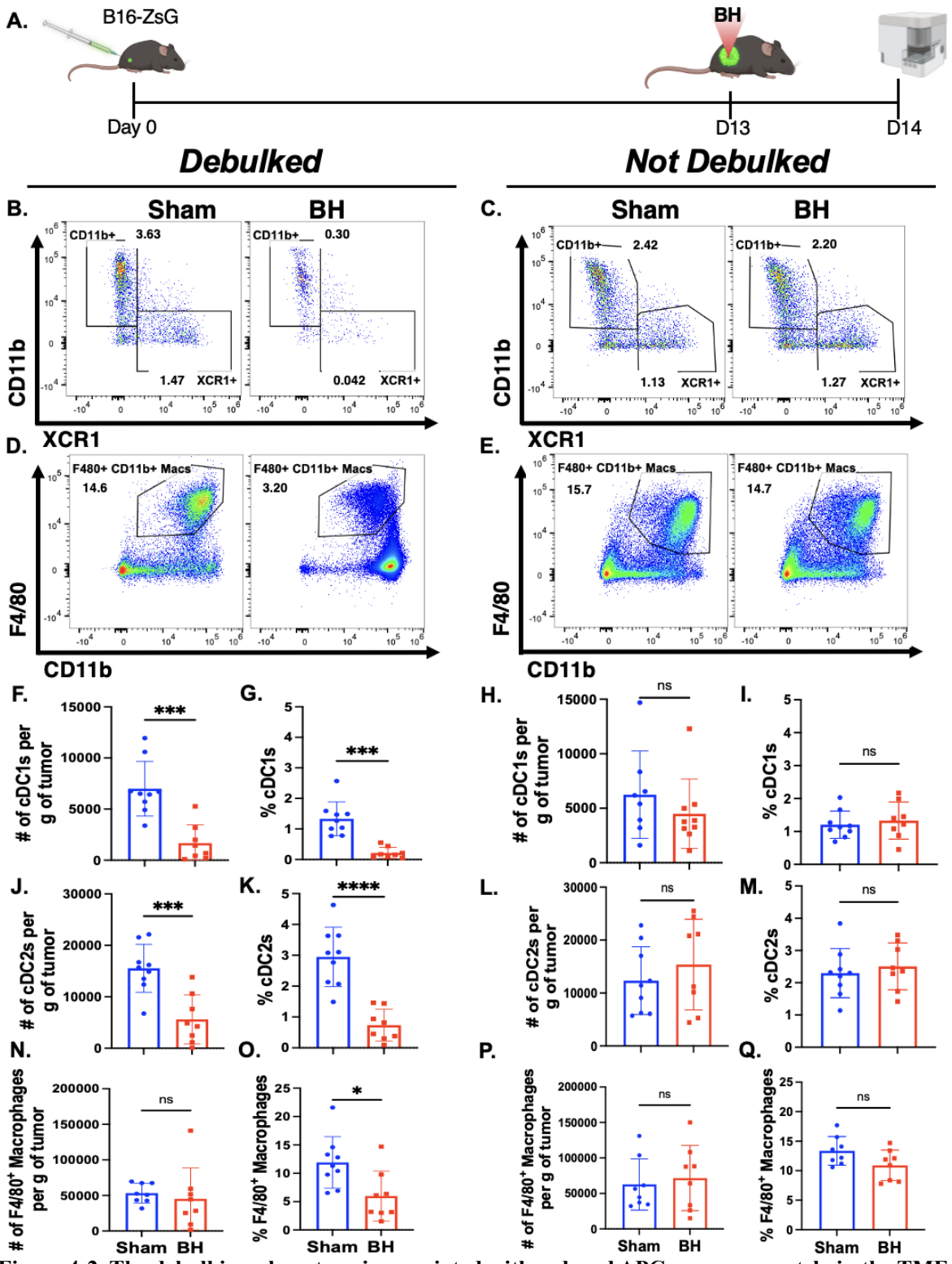

Figure 4-2. The debulking phenotype is associated with reduced APC presence acutely in the TME. A. Schematic for experimental timeline from tumor initiation to BH or Sham treatment followed by 24 h flow cytometry analysis of the tumors. **B&C.** Representative flow plots of cDC1 and cDC2 presence in the TME in debulked **(B)** and not debulked **(C)** experiments. Frequencies shown are of Live/CD45$^+$ population. **D&E.** Representative flow plots of F4/80+ macrophage presence in the TME in debulked **(D)** and not debulked **(E)** tumors. Frequencies shown are of Live/CD45$^+$ population. **F&H.** Quantification for the number of cDC1s per g of tumor. **G&I.** Bar graphs showing the proportion of Live/CD45$^+$ cells in the TME that are cDC1s. **J&L.** Quantification for the number of cDC2s per g of tumor. **K&M.** Bar graphs showing the proportion of Live/CD45$^+$ cells in the TME that are cDC2s. **N&P.** Quantification for the number of F4/80$^+$ macrophages per g of tumor. **O&Q.** Bar graphs showing the proportion of Live/CD45$^+$ cells in the TME that are F4/80$^+$ macrophages. (n=8-9) Unpaired t test with Welch's correction: ns = nonsignificant, ∗ P<0.05, ∗∗∗ P<0.001, ∗∗∗∗ P<0.0001; Mean ± SD. ROUT Outliers analysis with Q=0.1%.

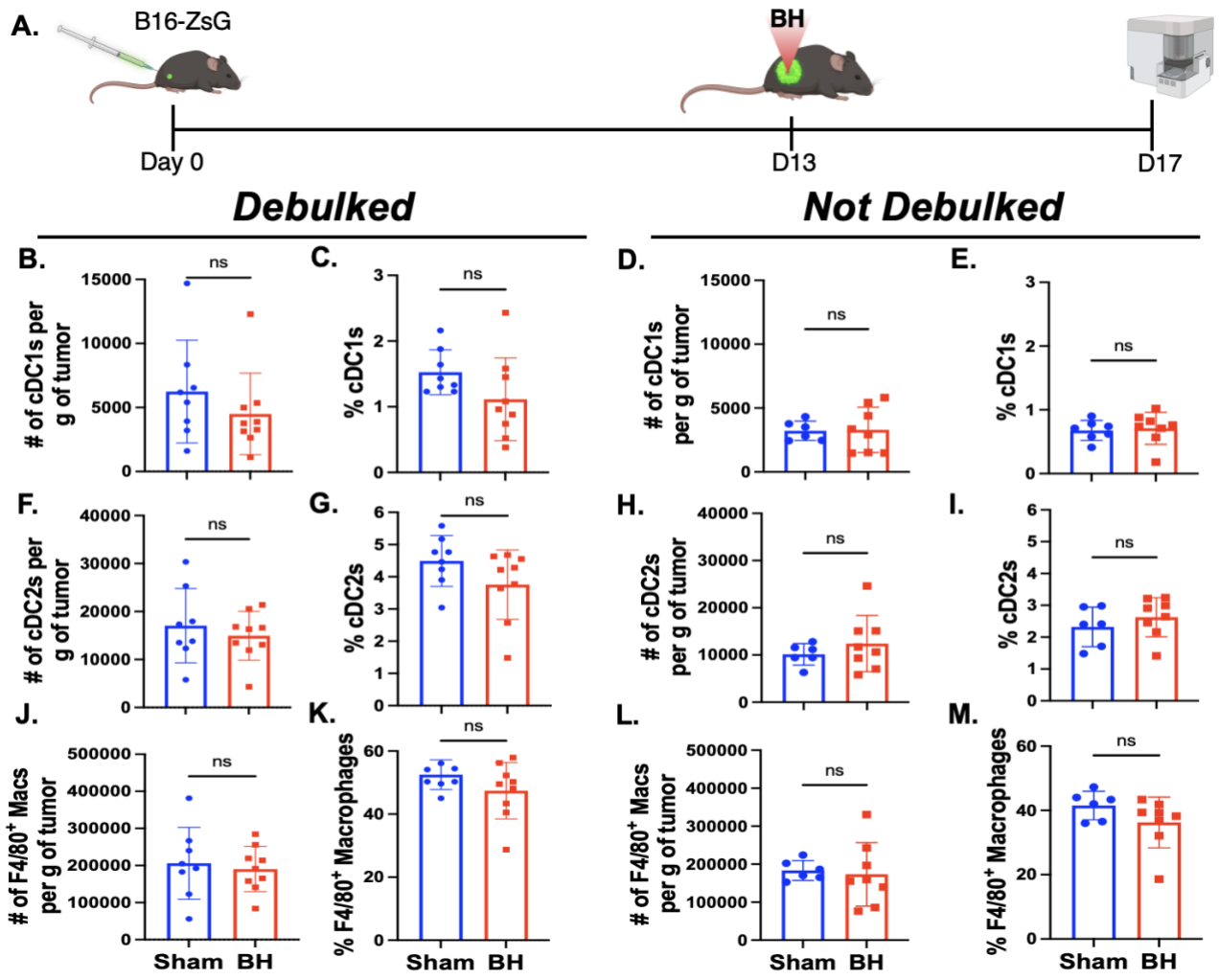

Figure 4-3. By 96 h post BH, no reduction is observed in APC presence in the TME. A. Schematic for experimental timeline from tumor initiation to BH or Sham treatment followed by 96 h flow cytometry analysis of the tumors. **B&D**. Quantification for the number of cDC1s per g of tumor. **C&E**. Bar graphs showing the proportion of Live/CD45$^+$ cells in the TME that are cDC1s. **F&H**. Quantification for the number of cDC2s per g of tumor. **G&I**. Bar graphs showing the proportion of Live/CD45$^+$ cells in the TME that are cDC2s. **J&L**. Quantification for the number of F4/80$^+$ macrophages per g of tumor. **K&M**. Bar graphs showing the proportion of Live/CD45$^+$ cells in the TME that are F4/80$^+$ macrophages. (n=7-8) Unpaired t test with Welch's correction: ns = nonsignificant; Mean ± SD**.** ROUT Outliers analysis with Q=0.1%.

Increased tumor antigen acquisition is associated with BH-induced primary melanoma debulking

While our prior work established that BH induces the dissemination of ZsG tumor antigen to the TDLNs, whether BH-mediated tissue destruction influences the acquisition of antigen by APCs in the TME following mechanical insult has not been determined. Given that

we have observed a bolus of ZsG antigen in the TDLNs post BH, we predicted that this antigen is also available in the TME. Understanding which cells are acquiring this antigen is important because if the antigen is being sequestered by highly phagocytic, pro-tumorigenic cells – such as TAMs which can cross-present antigen to both $CD8^+$ and $CD4^+$ T-cells and promote their terminal exhaustion[122] – and not making its way into cDCs, then the likelihood of initiating an adaptive immune response could be hindered. To begin addressing antigen uptake, we again utilized the B16-ZsG model. However, quantifying ZsG acquisition in the TME possesses challenges not previously observed when examining the LNs. We found that if we analyze the tumor samples with the ZsG^+ gate used to define antigen presence in the LNs, which is based on LNs from a naïve, non-tumor-bearing mouse, the majority of all Live/$CD45^+$ cells, including non-phagocytic CD8+ T cells are deemed positive (Figure 4-4A). To better refine our gating strategy and circumvent the problem of every immune cell subset appearing to contain ZsG, we chose to utilize a biologically negative control – $CD8^+$ T-cells as $CD8^+$ T-cells are not phagocytic. Upon further analysis, it became apparent that each individual tumor sample contained a unique shift in ZsG intensity (Figure 4-4B). Therefore, an individual gate is drawn on the tumor-resident $CD8^+$ T-cells for each sample, and this gate serves as the internal control for cell subsets analyzed within that particular tumor (Figure 4-4B&C). The increased intensity of ZsG correlates with the physical size of the tumor (Figure 4-4D). It is of note that the ZsG^+ gate drawn on the $CD8^+$ T-cells is done so using contour plots closest to the majority of the population. This is due to some samples experiencing a spread in ZsG staining on the $CD8^+$ T-cell population, which can be seen in Figure 4-4B with outliers falling in the ZsG^+ gate even though this population should be entirely biologically negative. We confirmed by ImageStream analysis that the ZsG fluorescence in $CD8^+$ cells in B16-ZsG tumors was present in a distinct punctate pattern, with limited side

scatter (SSC) complexity (Figure 4-5A); potentially suggesting fragmented pieces of fluorescent antigen stuck to the surface of these cells – most likely a result of processing and the release of tumor antigens post cell lysis. This ZsG composition was dissimilar to $CD11b^+$ cells in these tumors, which had diffused presence of ZsG throughout the entire cell consistent with phagolysosomes, with more visible and complex SSC – indicative of granules within the cells – as well as noticeable blebbing structures in the brightfield channels (Figure 4-5B). Altogether, this data suggests that utilizing $CD8^+$ T-cells as a biological control for our ZsG tumor antigen acquiring gate is sufficient to define antigen acquisition by APCs.

Given this gating strategy, we examined whether the level of BH-induced debulking of the primary tumor impacts antigen acquisition by APCs in the TME. We found that in the debulked tumor setting, BH significantly increased the proportion of cDC1s, cDC2s, and macrophages that contained ZsG tumor antigen 24 h post treatment (Figure 4-6B-E). This increase was dependent on successful debulking, as no differences in ZsG consumption were observed in these APCs in the non-debulked tumors (Figure4-6F-I). Interestingly, these significant proportional increases in ZsG capture found in the debulked tumors persisted, and were still observed in the cDC2s and macrophages present 96 h post BH (Figure 4-7C-D) – a trending increase seen in the cDC1s (Figure 4-7B). Similarly to the 24 h timepoint, there was no difference between the BH and Sham cohorts in the non-debulked setting (Figure 4-7E-G). Unfortunately, we cannot compare the GMF of ZsG on ZsG^+ APCs across samples because of the unique shifts between samples in ZsG intensity. Therefore, we cannot conclude whether BH is resulting in changes to the amount of antigen these cells are consuming on a per cell basis. Future studies are needed to optimize this staining approach, and quench external ZsGreen presence to avoid the shifts observed in ZsG intensity from sample to sample. Additionally, the

ImageStream system can be further employed to confirm external versus internal ZsG presence with an anti-ZsGreen fluorescent antibody to tag non-endocytosed antigen. These findings indicate that only in the setting when BH treatment induces tumor destruction at a level that results in constrain primary tumor outgrowth do we observe elevated tumor antigen acquisition by cDCs and macrophages in the TME. Furthermore, this data highlights that tumor antigen released following mechanical ablation is not being entirely sequestered by TAMs as both the remaining cDC1s and cDC2s experience proportional increase in ZsG acquisition at 24 h, and even when the number of cDCs in the debulked setting return to the Sham baseline at 96 h, the increased frequency of ZsG is still present; suggesting that BH in the debulked setting is having a sustained impact on tumor antigen acquisition by cDCs and macrophages.

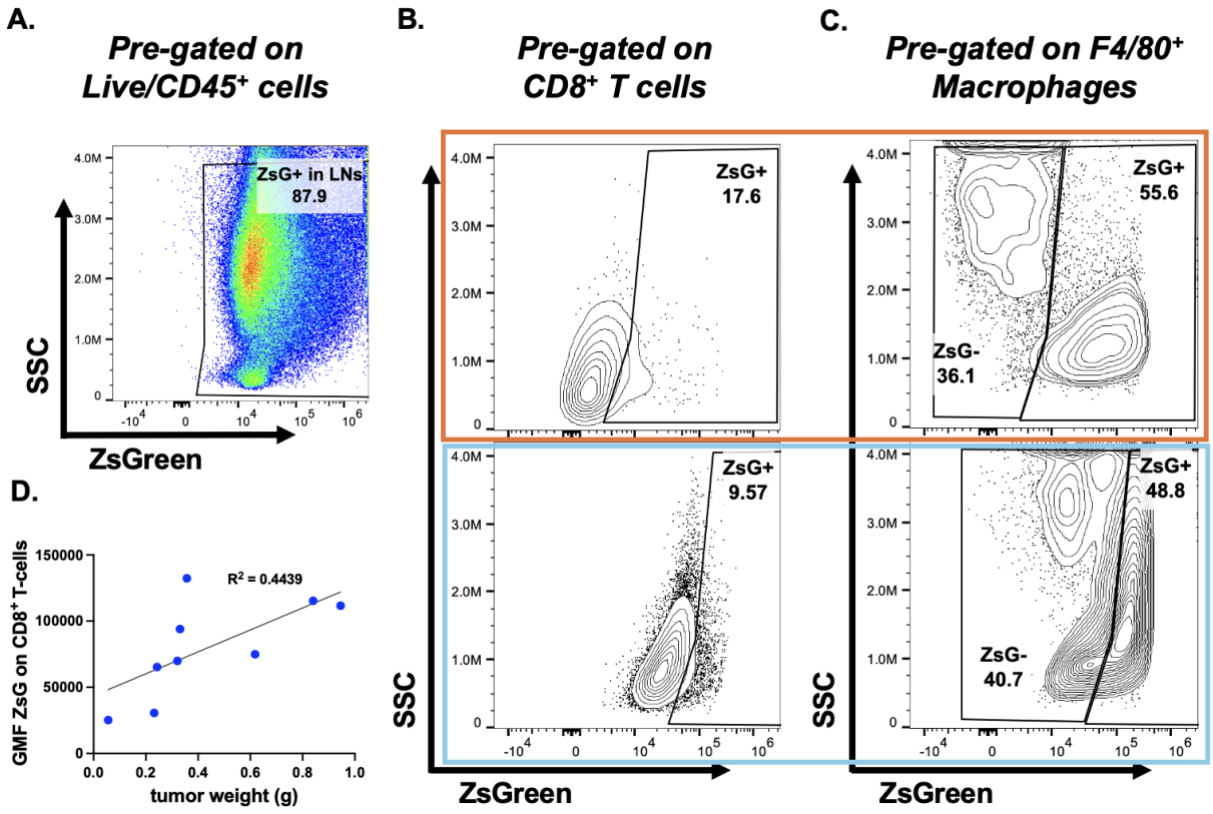

Figure 4-4. Identifying ZsGreen in the TME requires individualized gating on CD8$^+$ T-cells as a biologically negative control. A. Representative flow plot of the ZsG gate used in the TDLNs based on a naïve non-tumor-bearing control on Live/CD45$^+$ cells in the TME. **B.** Representative flow plots of CD8$^+$ T-cells being used to set the ZsG$^+$ gate for each sample. **C.** Representative scatter plots showing ZsG presence in F4/80$^+$ macrophages. The orange and blue boxes represent matched samples from the same tumor. **D.** Linear regression correlation between the GMF of ZsG on CD8$_+$ T-cells and tumor weight (g) in the Sham untreated cohort. Simple linear regression model.

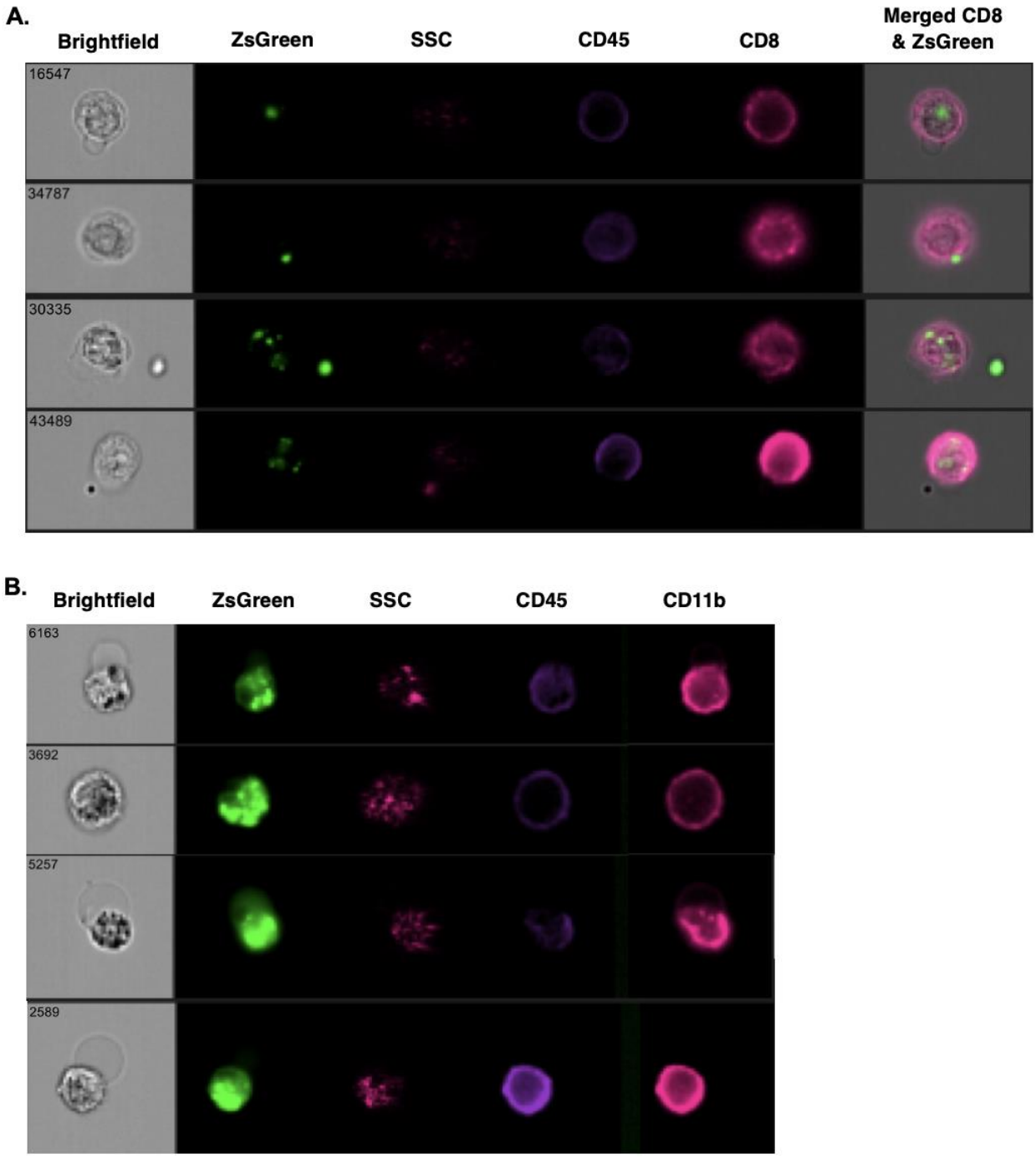

Figure 4-5. ImageStream microscopy showing distinct ZsGreen presence on $CD8^+$ and $CD11b^+$ immune cells in the TME. A. Representative images of $CD45^+CD8^+$ cells from B16-ZsG tumors displaying punctate ZsGreen. Pre-gated on live cells. **B.** Representative images of $CD45^+CD11b^+$ cells from B16-ZsG tumors displaying diffuse ZsGreen. Pre-gated on live cells.

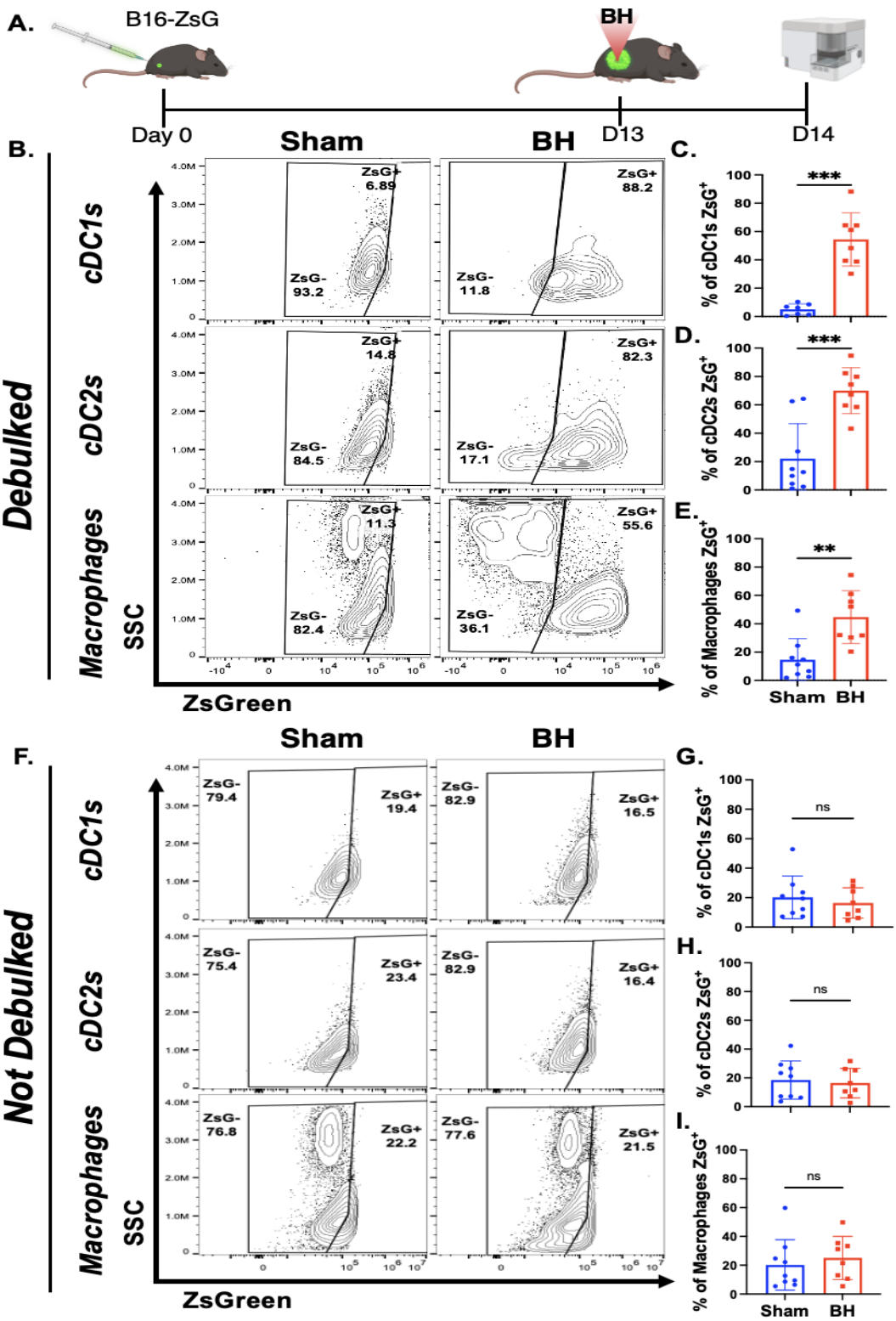

Figure 4-6. Increased tumor antigen acquisition is associated with BH-induced debulking of primary melanoma. **A.** Schematic for experimental timeline from tumor initiation to BH or Sham treatment followed by 24 h flow cytometry analysis of the tumors. **B.** Representative flow plots from an experiment where tumor debulking was observed post BH, showing ZsG presence in cDC1s (top), cDC2s (middle) & macrophages (bottom) in the TME of Sham and BH cohorts. Frequencies shown are of the parent population. **C-E.** Quantification of flow data in the debulked setting for the proportion of cDC1s, cDC2s & macrophages that are ZsG^+, respectively. **F.** Representative flow plots from an experiment where no tumor debulking was observed post BH, showing ZsG presence in cDC1s (top), cDC2s (middle) & macrophages (bottom) in the TME of Sham and BH cohorts. Frequencies shown are of the parent population. **G-I.** Bar graphs of flow data in the non-debulked setting for the proportion of cDC1s, cDC2s & macrophages that are ZsG^+, respectively. (n=8-9) Unpaired t test with Welch's correction: ns = nonsignificant, ** $P<0.01$, *** $P<0.001$; Mean ± SD. ROUT Outliers analysis with Q=0.1%.

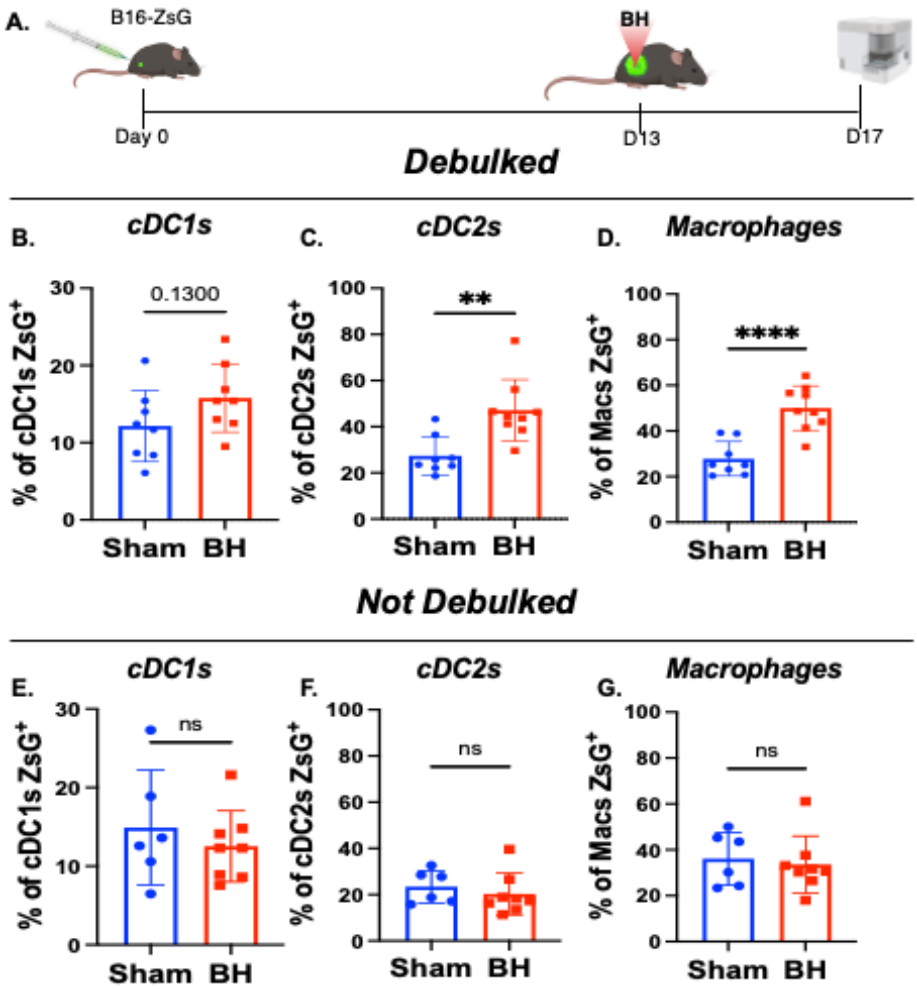

Figure 4-7. Increased tumor antigen acquisition persists when BH-induced debulking is observed. A. Schematic for experimental timeline from tumor initiation to BH or Sham treatment followed by 96 h flow cytometry analysis of the tumors. **B-D.** Quantification of flow data in the debulked setting for the proportion of cDC1s, cDC2s & macrophages that are ZsG^+, respectively. **E-G.** Bar graphs of flow data in the non-debulked setting for the proportion of cDC1s, cDC2s & macrophages that are ZsG^+, respectively. (n=8-9) Unpaired t test with Welch's correction: ns = nonsignificant, ** P<0.01, **** P<0.0001; Mean ± SD**.** ROUT Outliers analysis with Q=0.1%.

Varying degrees of cDC phenotypic activation is observed in BH treated melanoma tumors

We have previously reported that BH induces cDC activation in a tumor antigen dependent manner in the TDLNs. We had specifically focused on cDC activation as they are the professional APCs capable of eliciting a robust T-cell response[2]. Interestingly, the relationship between ZsG acquisition and cDC activation was observed in both the debulked and non-

debulked setting, and it is of note that the expansion of tumor-specific $CD8^+$ T-cells we described in chapter three (Figure 3-7H-K & Figure 3-11B-G) was also seen in the setting of non-tumor debulking. This suggests that BH – even if not resulting in mass tumor destruction – is still an immunogenic insult capable of enhancing cDC activation. We thus tested whether BH resulted in cDC activation in the TME, and whether the degree of debulking impacted the level of cDC activation. We first examined tumors by flow cytometry, assessing the level of expression of CD86 on the cDCs as CD86 is a co-stimulatory molecule upregulated on the surface of cDCs as the undergo activation and maturation. We found that when tumor debulking was observed, CD86 was significantly unregulated on the surface of cDC1s in these tumors (Figure 4-8B-C), and a greater proportion of tumoral cDC1s were activated post BH – expressing high level of CD86 and MHC-II (Figure 4-8D). No differences in activation were observed on the cDC2 population (Figure 4-8B, E-F). Contrary to the debulked tumors, in intact tumors no CD86 elevation was seen on the cDC1s, while the cDC2s experienced increased CD86 intensity and $CD86^{hi}MHC\text{-}II^{hi}$ expression following BH (Figure 4-8G-K). We next examined whether BH-mediated cDC activation is dependent on ZsG antigen acquisition. Differing from what we had previously reported in the TDLNs, we found equivalent elevation of CD86 occurred after BH in both ZsG^+ and ZsG^- cDCs. (Figure 4-9B-E). Similarly, both ZsG^- and ZsG^+ cDC2s are activated after BH in the non-tumor outgrowth-controlled setting (Figure 4-9N-Q). No differences in activation are observed in BH cohorts from either tumor setting 96 h post treatment.

As the TME can be highly immunosuppressive, we hypothesized the cDCs in the TDLNs would undergo a greater level of activation when responding to the liberated tumor antigen post BH, compared to cDCs residing in the TME. To address this hypothesis, we compared the level of CD86 expressed on the surface of both antigen positive and non-antigen positive cDCs from

paired tumors and TDLNs. In most instances, we were surprised to observe that the cDCs in the TMEs expressed a greater or equal to amount of CD86 when compared to the cDCs found in their respective TDLNs (Figure 4-10A-E, G-H) – suggesting that cDCs in the TME are just as capable of becoming phenotypically activated as cDCs in the TDLNs. Further studies will need to be done to confirm functionality and capability of activating T-cells for both tumoral and TDLN cDCs.

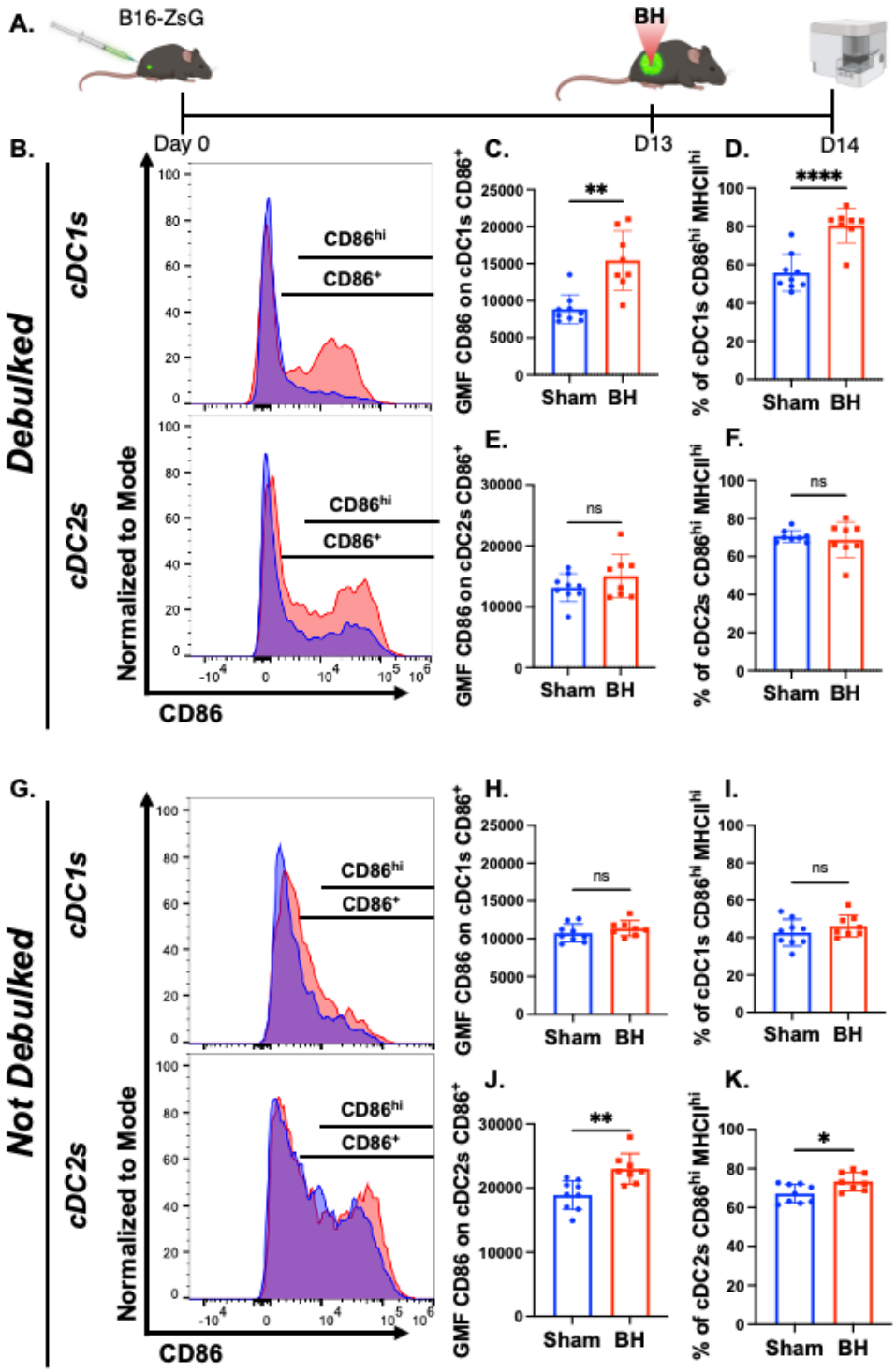

Figure 4-8. Tumor debulking by BH is associated with elevated phenotypic activation of cDC1s, while cDC2s are impacted by mechanical ablation when no debulking is observed. A. Schematic for experimental timeline from tumor initiation to BH or Sham treatment followed by 24 h flow cytometry analysis of the tumors. **B.** Histograms showing CD86 intensity on cDC1s (top) and cDC2s (bottom) after treatment with BH or Sham control in the debulked setting. **C.** Bar graph quantifying the GMF of CD86 on total cDC1s $CD86^{+}$ in the TME. **D.** Quantification for the proportion of cDC1s appearing phenotypically activated ($CD86^{hi}MHCII^{hi}$) in the TME. **E.** Bar graph quantifying the GMF of CD86 on total cDC2s $CD86^{+}$ in the TME. **F.** Quantification for the proportion of cDC2s appearing phenotypically activated ($CD86^{hi}MHCII^{hi}$). **G.** Histograms showing CD86 intensity on cDC1s (top) and cDC2s (bottom) after treatment with BH or Sham control in the non-debulked setting. **H.** Bar graph quantifying the GMF of CD86 on total cDC1s $CD86^{+}$ in the non-debulked tumors. **I.** Quantification for the proportion of cDC1s appearing phenotypically activated ($CD86^{hi}MHCII^{hi}$) in the TME. **J.** Bar graph quantifying the GMF of CD86 on total cDC2s $CD86^{+}$. **K.** Quantification for the proportion of cDC2s appearing phenotypically activated ($CD86^{hi}MHCII^{hi}$) in the TME. (n=8-9) Unpaired t test with Welch's correction: ns = nonsignificant, ∗ P<0.05, ∗∗ P<0.01, ∗∗∗∗ P<0.0001; Mean ± SD**.** ROUT Outliers analysis with Q=0.1%.

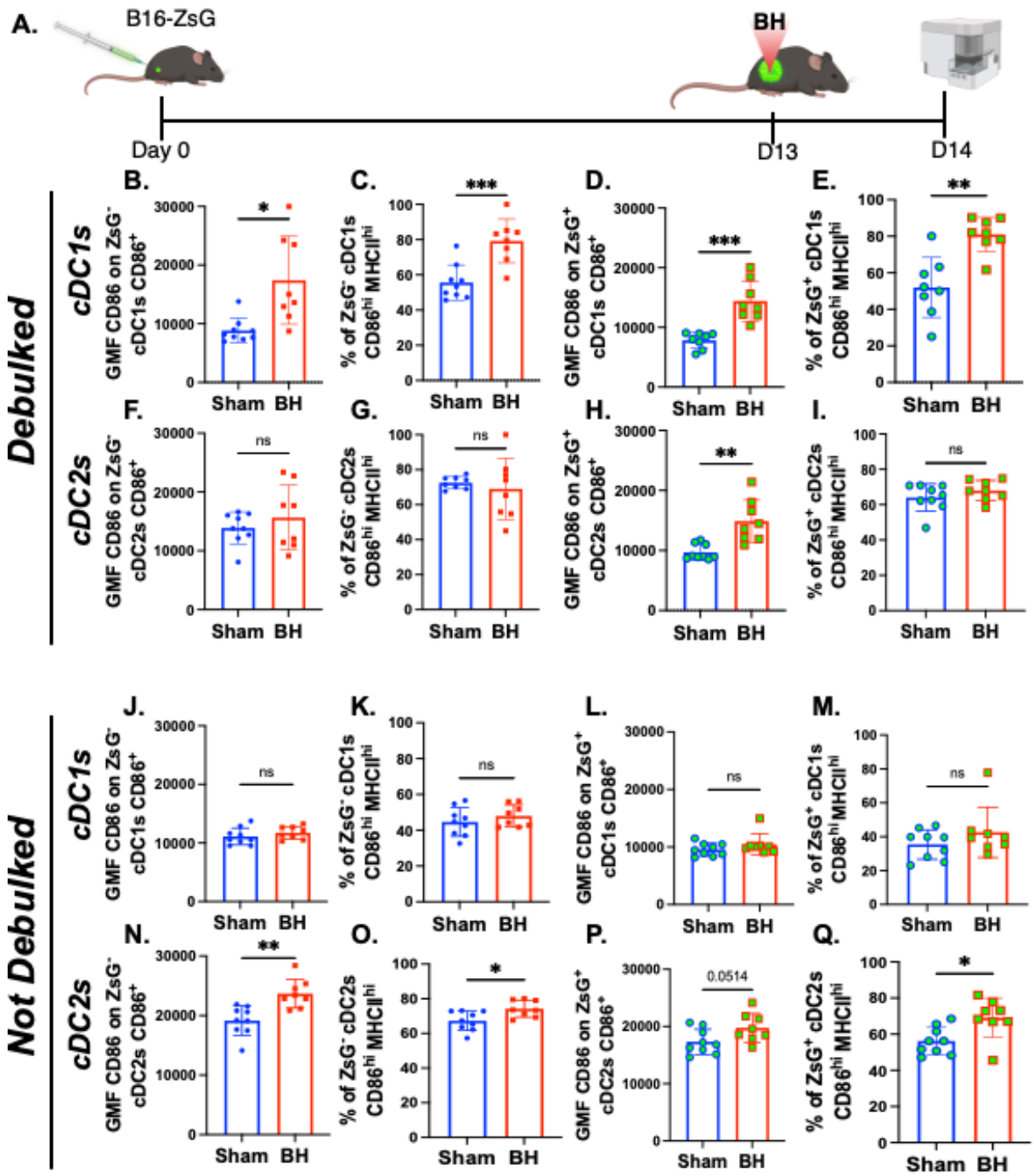

Figure 4-9. When phenotypic activation post BH is observed, it is not dependent on ZsG antigen acquisition. A. Schematic for experimental timeline from tumor initiation to BH or Sham treatment followed by 24 h flow cytometry analysis of the tumors. **B&F.** Quantification for the GMF of CD86 on ZsG^- $CD86^+$ cDC1s **(B)** and cDC2s **(F)**. **C&G.** Bar graphs in the debulked setting showing the proportion of ZsG^- cDC1s **(C)** and ZsG^- cDC2s **(G)** phenotypically activated ($CD86^{hi}MHCII^{hi}$) in the TME. **D&H.** Quantification for the GMF of CD86 on ZsG^+ $CD86^+$ cDC1s **(D)** and cDC2s **(H)**. **E&I.** Bar graphs showing the proportion of ZsG^+ cDC1s **(E)** and ZsG^+ cDC2s **(I)** phenotypically activated ($CD86^{hi}MHCII^{hi}$). **J&N.** Quantification for the GMF of CD86 in the non-debulked tumors on ZsG^- $CD86^+$ cDC1s **(J)** and cDC2s **(N)**. **K&O.** Bar graphs showing the proportion of ZsG^- cDC1s **(K)** and ZsG^- cDC2s **(O)** phenotypically activated ($CD86^{hi}MHCII^{hi}$) in the TME. **L&P.** Quantification for the GMF of CD86 on ZsG^+ $CD86^+$ cDC1s **(L)** and cDC2s **(P)**. **M&Q.** Bar graphs showing the proportion of ZsG^+ cDC1s **(M)** and ZsG^+ cDC2s **(Q)** phenotypically activated ($CD86^{hi}MHCII^{hi}$) in the TME. (n=8-9) Unpaired t test with Welch's correction: ns = nonsignificant, ∗ $P<0.05$, ∗∗ $P<0.01$, ∗∗∗ $P<0.001$; Mean ± SD**.** ROUT Outliers analysis with Q=0.1%.

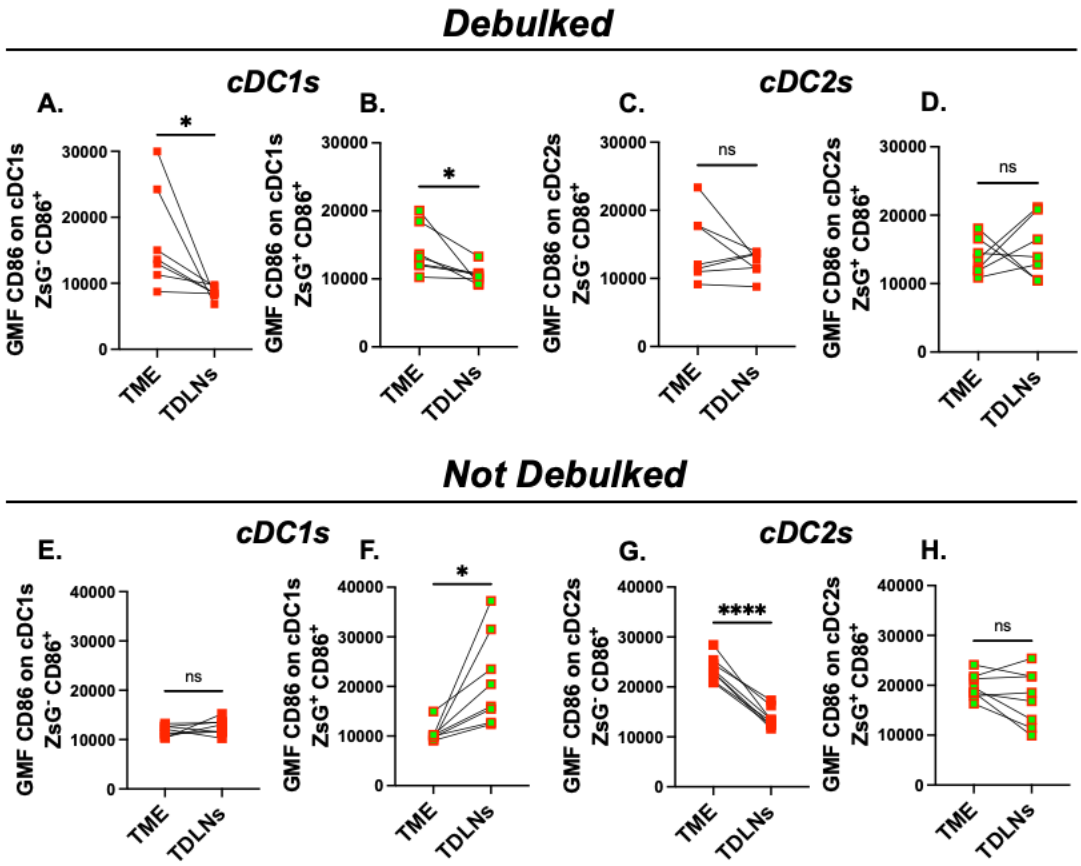

Figure 4-10. cDCs in the TME do not have hindered CD86 activation compared to paired cDCs in the TDLNs. All values are pulled from BH cohorts. **A&E.** GMF CD86 on paired ZsG$^-$ CD86$^+$ cDC1s from matched tumors and TDLNs. **B&F.** GMF CD86 on paired ZsG$^+$ CD86$^+$ cDC1s from matched tumors and TDLNs. **C&G.** GMF CD86 on paired ZsG$^-$ CD86$^+$ cDC2s from matched tumors and TDLNs. **D&H.** GMF CD86 on paired ZsG$^+$ CD86$^+$ cDC2s from matched tumors and TDLNs. (n=7-8) Paired t test: ns = nonsignificant, ∗ P<0.05, ∗∗∗∗ P<0.0001. ROUT Outliers analysis with Q=0.1%.

BH-induced tumor debulking is associated with increased CCR7 expression on cDC1s

When we previously examined the expression of CCR7 – the chemokine receptor involved in cDC migration – on cDCs in the TDLNs, we observed no differences in the BH cohorts compared to Sham controls (Figure 3-6). As this is only one component of cDC trafficking from the TME to the TDLNs, we next tested whether its expression was altered on cDCs in the TME. Similarly to activation status, we found that CCR7 was upregulated only on cDC1s in the setting of tumor-debulking (Figure 4-11B-F). In the non-tumor debulked studies, minimal to no changes were observed. As CCR7 is also upregulated because of cDC activation,

this data further supports that BH regimens that result in tumor growth constrain are inducing the activation of cDC1s in the TME.

In summary, these data suggest that varying efficacy and destruction by BH relates to antigen acquisition by APCs in the TME, and activation of different cDC subsets in the TME, in contrast to the TDLN, is independent of ZsG tumor antigen acquisition; suggesting that DAMPs released in response to mechanical insult by BH is sufficient to induce cDC activation in the TME. These findings are important when thinking about utilizing BH as a partially ablative therapy to induce an adaptive immune response. It suggests that the parameters of the sound waves can be tuned to better elicit cDC1 activation, which may prove beneficial as these cells can directly cross-present tumor antigen to $CD8^+$ T-cells, while cDC2s require antigen-antibody complexes or soluble antigen to cross-present to $CD8^+$ T-cells[5]. The differences in cDC activation may provide a mechanism for understanding why tumor growth is constrained in one setting but not the other.

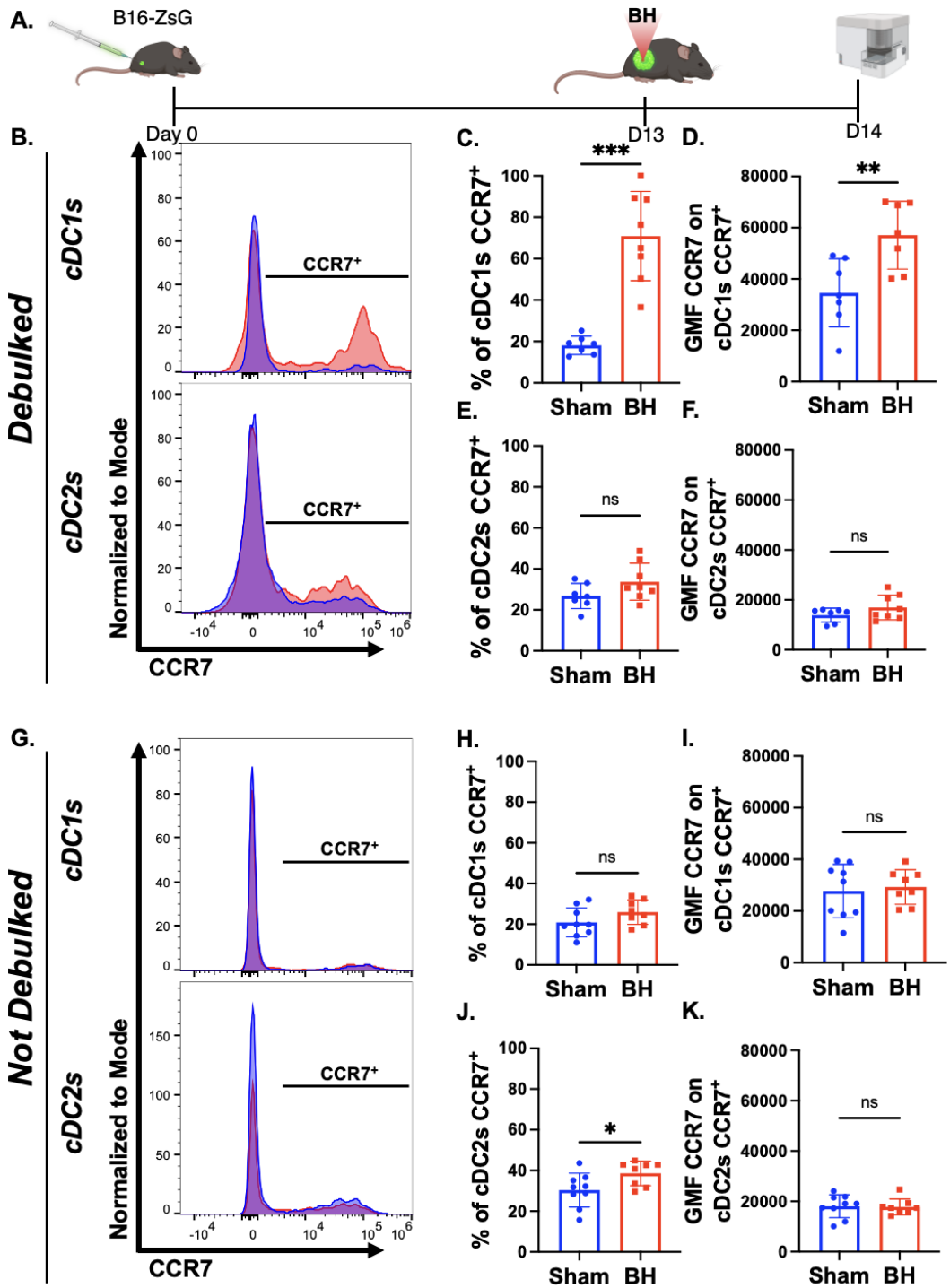

Figure 4-11. BH-induced tumor debulking is associated with increased CCR7 expression on cDC1s. A. Schematic for experimental timeline from tumor initiation to BH or Sham treatment followed by 24 h flow cytometry analysis of the tumors. **B.** Histograms showing CCR7 intensity on cDC1s (top) and cDC2s (bottom) after treatment with BH or Sham control in the debulked setting. **C.** Bar graph quantifying the GMF of CCR7 on total cDC1s CCR7$^+$ in the TME. **D.** Quantification for the proportion of cDC1s CCR7$^+$ in the TME. **E.** Bar graph quantifying the GMF of CCR7 on total cDC2s CCR7$^+$ in the TME. **F.** Quantification for the proportion of cDC2s CCR7$^+$ in the TME. **G.** Histograms showing CCR7 intensity on cDC1s (top) and cDC2s (bottom) after treatment with BH or Sham control in the non-debulked setting. **H.** Bar graph quantifying the GMF of CCR7 on total cDC1s CDCR7$^+$ in the non-debulked tumors. **I.** Quantification for the proportion of cDC1s CCR7$^+$. **J.** Bar graph quantifying the GMF of CCR7 on total cDC2s CCR7$^+$. **K.** Quantification for the proportion of cDC2s CCR7$^+$ in the TME. (n=8-9) Unpaired t test with Welch's correction: ns = nonsignificant, ∗ P<0.05, ∗∗ P<0.01, ∗∗∗ P<0.001; Mean ± SD. ROUT Outliers analysis with Q=0.1%.

DISCUSSION

Given that acquisition and presentation of tumor antigen by APCs to T-cells is intrinsically influential in initiating a T-cell mediated response to cancer, we chose to address gaps in knowledge in the FUS field regarding the impact mechanically ablating tumors with BH has on APC presence, antigen acquisition, and activation states at two respective timepoints relative to the therapy.

Upon treating with BH and monitoring tumor outgrowth, we observed instances where BH-induced primary tumor debulking in some studies, and no evidence of debulking in others (Figure 4-1). The ability of BH to constrain tumor growth correlated with qualitative B-mode imaging assessment of a greater degree of cavitation in the treated tissue. However, this assessment is subjective, and not a direct measurement of endogenous bubble formation and cavitation as the imaging is only displaying hyperechoic lesions resulting from the treatment. The nature of tissue destruction via BH is highly chaotic, and it relies on the formation, oscillation and implosion of endogenous vapor bubbles within the ablative tissue[97]. While passive cavitation detection (PCD) monitoring is commonly used in conjunction with other FUS modalities to measure the oscillation and cavitation of exogenous microbubbles in a controlled setting[123], i.e. when the ultrasonic signals are either applied or not, the current PCD technology available to us cannot detect the formation of endogenous bubbles and monitor their response during BH. This technology remains to be developed.

It has been well established that the presence of APC subsets in the TME have prognostic implications[118,119,124]. By utilizing spectral flow cytometric analysis, we found that the level of tumor debulking induced by BH resulted in profoundly divergent consequences on immune populations in the TME. When BH treatment resulted in tumor control, the number of cDCs

residing in the TME was significantly reduced (Figure 4-2F&J). This effect was not sustained, as the cDC1 and cDC2 populations returned to the Sham baseline by 96 h (Figure 4-3). In contrast, when primary tumor debulking was not induced by BH, there were no alterations in APC presence observed at either the 24 or 96 h timepoints. Interestingly, the number of F4/80$^+$ macrophages was not altered by the ablation (Figure 4-2N). This could be a result of macrophages repopulating the TME faster than cDCs following insult to the tumor, or macrophages may be less sensitive to mechanical stress. Future studies are required to address the dynamics of APC repopulation of the TME, with particular interest to understand whether newly repopulating APCs, specifically the cDC1s, are transcriptionally different than the cDC1s that had been residing in the TME prior to ablation. It has been shown that tumor-residing cDC1s are required for tumor-specific CD8$^+$ T-cell recruitment into the TME[125], and that cDCs in the TME need to provide a secondary co-stimulation signal via CD80/CD86 to promote CD8$^+$ T-cell effector function[11]. However, to be able to achieve the secondary co-stimulation and promote T-cell recruitment, the cDCs must be activated. Not all cDCs in the TME reside there transiently; some are retained in the tumor. Transcriptionally, these retained cDCs develop an exhausted phenotype. They downregulate genes associated with antigen presentation and cDC activation[124]. Therefore, knowing if BH ablation is resulting in the abrogation of exhausted, tumor-retained cDCs, which are then repopulated shortly after treatment with non-immunosuppressed cDCs capable of initiating CD8$^+$ T-cell activation, is important when considering why debulking the primary tumor is observed in some settings but not others.

Given our previous work examining tumor antigen liberation and dissemination to the TDLNs following BH treatment, we investigated whether BH-mediated tissue destruction influences the acquisition of antigen by APCs in the TME. We determined, similarly to the

effects on APC abundance, that the level of primary tumor control dictated whether increased capture of tumor antigen was observed. We found that in the debulked setting, BH significantly increased the proportion of ZsG tumor antigen positive APCs acutely – 24 h following treatment – and most of these effects were sustained through 96 h (Figures 4-6B-E & 4-7B-D). As no differences were found in ZsG consumption by tumoral APCs in the non-debulked tumors (Figures 4-6F-I & 4-7E-G), these increases observed in ZsG acquisition are dependent on tumor control. These findings provide clarity in that antigen liberation through the mechanical ablation of melanoma tumors is not being sequestered from cDCs. The cDCs remaining in the TME as well as those repopulating the TME during the 96-h span post BH can effectively engulf tumor antigen, but tt remains to be determined whether these tumor cDCs can effectively process it. We propose the use of a B16-ZsGminOVA model, which expresses the peptides specific for OT-I and OT-II T-cells, to measure MHC-peptide complexes and cross-presentation by these cDCs in the future.

When the cDC1 population is expanded and activated at the tumor site, therapeutic responsiveness of melanoma to ICB and targeted therapies is improved[126]. We tested whether BH – either in the debulked or non-debulked setting – was providing enough of an inflammatory signal to influence phenotypic activation changes to the cDC populations. 24 h post BH, we observed that in the setting of primary tumor control, CD86 upregulation and activation was promoted almost exclusively in the cDC1 population (Figures 4-8B-F & 4-9B-I), while in the non-debulked setting, activation was only seen in the cDC2 population (Figure 4-8G-K & 4-9J-Q). The effects on activation were transient, as no differences were observed in either BH cohort 96 h following treatment. In both instances, BH-mediated cDC activation is not dependent on ZsG antigen acquisition as equivalent upregulation of CD86 occurred after BH in both ZsG^{+} and

ZsG^- cDCs. This implies that DAMP release from BH-induced tumor-cell lysis is sufficient to promote cDC activation in the TME independent of antigen engulfment. We acknowledge that our proxy used here for cDC activation is entirely phenotypic. Future studies should be performed to analyze the functional capabilities of these tumoral cDC populations.

In conclusion, our findings provide the first pieces of evidence pertaining to the impact of BH on tumor antigen acquisition and APC presence in the TME. Additionally, these results highlight that the varying efficacy and debulking nature of BH induces substantially different immune effects in the TME, particularly as these findings demonstrate that the degree of tumor debulking induced by BH can skew preferential cDC activation. While cDC1s in many different cancer types are associated with improved survival, the presence of cDC2s in tumors have variable associations with treatment response and prognosis [127]. Therefore, having the ability to fine-tune BH intensity, cavitation, and ultimately the level of primary growth control induced, will be essential when determining optimal treatment regimens for this non-invasive therapeutic.

Chapter Five: Attempts to attenuate the myeloid compartment in murine TNBC to advance our understanding of TFUS+GEM-mediated tumor control.

Some of this work is modified from the manuscript "Tissue- and Temporal-Dependent Dynamics of Myeloablation in Response to Gemcitabine Chemotherapy" accepted for publication in *Cells*

Lydia E. Kitelinger, Eric A. Thim, Sarah Y. Zipkowitz, Richard J. Price and Timothy N. J. Bullock

INTRODUCTION

Breast cancer (BrCa) remains the second leading cause of cancer mortality in women. In 2023, about 297,000 new cases of invasive BrCa were diagnosed[37]. This disease is inherently heterogenous. Clinically, the expression of estrogen (ER), progesterone (PR), and human epidermal growth factor 2 (HER2) receptors are used to subdivide BrCa cases—with treatment and prognosis hinging on receptor expression. Triple-negative breast cancer (TNBC) refers to a subgroup of breast tumors lacking ER/PR/HER2 expression. TNBC makes up about 15% of all BrCa cases. Compared to hormone receptor and HER2-positive subtypes, TNBC presents as a more aggressive cancer, with a mortality rate of 40% within 5 years following diagnosis[38,39]. Mortality is often the result of metastatic disease, and patients with TNBC are more likely to experience distant metastatic spread and local recurrence than patients presenting with other BrCa subtypes[40–43,128]. While historically TNBC has lacked targeted drug and antibody treatments that are available for ER/PR$^+$ and HER2$^+$ BrCa, in the last few years, pembrolizumab (anti-PD-1; ant-programmed cell death protein 1) immunotherapy has emerged as a promising neoadjuvant and late-stage therapeutic for TNBC patients whose tumors present with a combined positive score of 10 for PD-L1 expression[44,45]. However, only ≈20–34% of TNBC malignancies

meet this criterion for pembrolizumab treatment[46,47]. As current research studies aim and continue to identify molecular targets of TNBC[129], cytotoxic chemotherapies remain a systemic treatment option for these patients[130].

Chemotherapy was first used in patients with metastatic BrCa in 1976 when Bonadonna et al. showed that combining cyclophosphamide, methotrexate, and fluorouracil as an adjuvant therapy improved patient outcome[131]. In the decades since, the addition of anthracyclines, taxanes, and various combinations of alkylating agents, antimetabolites, antibiotics, and mitotic spindle inhibitors have been explored as treatment regimens for BrCa both in the adjuvant and neoadjuvant settings[132]. One such chemotherapy is gemcitabine (GEM; 2′2′-difluorodeoxycytidine), a pyrimidine antimetabolite agent that incorporates into the DNA of replicating cells. GEM's self-potentiating mechanism allows it to be highly effective at inducing cell cycle arrest and apoptosis of proliferating cells[133–135]. GEM stands out clinically from other chemotherapies because of its tolerability and low side-effect profile[136]. GEM has shown efficacy as a single agent in BrCa therapy[137–142], and its favorable toxicity profile has allowed it to be used in combination with many other antitumor drugs in the context of BrCa[143]. Currently, GEM is being used in the clinic as a third-line treatment for patients with ER^+ metastatic BrCa, and it is used as a first-line treatment of metastatic TNBC when combined with carboplatin and pembrolizumab[44].

In addition to its nucleoside activity, GEM has been reported to have favorable immunologic effects. BrCa malignancies arise when tumor cells acquire resistance to immunosurveillance and evade elimination by the immune system. This is deemed the "escape" phase of cancer progression, and it is commonly associated with the development of an immunosuppressive tumor microenvironment (TME)[18]. Prominent immune cell subsets involved

in pro-tumorigenic immunity are myeloid-derived suppressor cells (MDSCs)[19]. MDSCs—both monocytic (M-MDSCs) and granulocytic (G-MDSCs)—differentiate from immature myeloid cells that undergo high levels of dysregulated myelopoiesis in response to BrCa[49]. Within the 4T1 mammary carcinoma model of TNBC, G-MDSCs are highly prevalent in the TME[88]. MDSCs function as pro-tumorigenic by inhibiting T-cell proliferation and their cytolytic activity[50–52], supporting tumor angiogenesis[53,54], triggering metastasis dissemination[55], and inducing the expansion of other suppressive immune cell populations such as regulatory T-cells (T_{regs})[56] and tumor-associated macrophages (TAMs)[57]. In preclinical BrCa models, GEM has been deemed a myeloablative therapy, as it significantly reduces the presence of GR-1^+ MDSCs[144] in the periphery of tumor-bearing mice without perturbing other immune cell populations like $CD4^+$ T cells, $CD8^+$ T cells, and B cells[145,146]. In the murine 4T1 model, Le et al. showed that GEM acts on suppressive MDSCs that accumulate within mice bearing tumors, and that GEM treatment enhances splenic T-cell expansion and response to antigenic stimuli in vitro[88]. This apparent selective hinderance of MDSCs could be clinically important as MDSC enrichment is associated with poor prognosis in BrCa patients[59]. High levels of circulating MDSCs correlate with liver and bone metastases and higher levels of circulating tumor cells[147], while the presence of tumor-infiltrating lymphocytes (TILs) like $CD4^+$ and $CD8^+$ T cells in tumors is positively correlated with BrCa prognosis[60,61]. Additionally, TNBC tumors have a greater level of MDSC infiltration than non-TNBC samples[55]. A key motivation of these studies lies in the possibility of selectively targeting MDSCs, increasing TIL presence, and ultimately expanding the number of TNBC patients susceptible to anti-PD-1 immunotherapy. Thus, the repurposing of GEM as a chemo-myeloablative therapy could be an attractive option for augmenting immunotherapies.

We have also previously reported that the combination of thermal ablative focused ultrasound (TFUS) with GEM constrained 4T1 TNBC outgrowth and lengthened overall survival in a T-cell dependent manner[84]. We hypothesized that GEM was working to alleviate immunosuppression in the 4T1 TME by depleting MDSCs, resulting in enhanced T-cell cytotoxicity and killing of the tumor cells. We aimed to test this by employing myeloid depleting monoclonal antibodies (mAbs), to determine if the effects of these mAbs with TFUS mimicked the efficacy we observed with TFUS+GEM. Additionally, we wanted to characterize the effects GEM was having as a monotherapy on the immune repertoire in the 4T1 TME because while the myeloablative effects of GEM as a treatment for BrCa have been characterized on peripheral immune cells, there is limited understanding of the impacts GEM has on immune populations found in the TME[144,148]. The incomplete knowledge of the effects GEM has on lymphocytes in the TME is especially important given that the presence of TILs is a positive prognostic factor in predicting disease-free survival for TNBC patients[149]. Understanding the intratumoral immunological effects of GEM as a monotherapy is essential when thinking about patient response and potential drug combinatorial therapies against TNBC.

In performing these studies, we found that myeloid depleting mAbs targeting Ly6G and GR1 – two molecules expressed by MDSC populations – had severe toxicity side effects in the 4T1 model, ultimately, proving lethal even with revised and titrated dosing regimens. These mAbs were also unable to sustain depletion of these myeloid populations, suggesting that emergency myelopoiesis was being induced. In addition to toxicity from the mAb, we had to counteract toxicity from the TFUS therapies – leading us to alter our ablation regimen from that used by *Sheybani et al.*[84] such that less of the tumor received TFUS and leaving more viable malignant tissue remaining. In doing so, we discovered though bulk RNA-sequencing, that

different TFUS ablation intensities induce varying transcriptional changes in the TME. For these reasons, our subsequent studies focused on the role of GEM in the TME of TNBC.

We initially hypothesized that GEM would have myeloablative consequences on MDSCs in the TME, while increasing the presence of TILs in TNBC tumors. We directly compared the impacts of GEM on immune cell presence and functionality in the TME to those found in the periphery. Through bulk-RNA sequencing, we identified immune-related pathways significantly upregulated in TNBC tumors acutely after systemic GEM administration, and we explored whether GEM-mediated constrain of TNBC tumor outgrowth is dependent on the presence of the highly inflammatory cytokine interferon-gamma (IFN-γ). Overall, our findings yield new insights into the tissue- and temporal-dependent immune ablative effects of GEM—a clinically employed chemotherapy. Our findings contrast the current and widely perceived paradigm that this therapeutic is specifically myeloablative.

RESULTS

Antibody approaches to directly deplete MDSC presence in the 4T1 murine TNBC model resulted in aberrant myelopoiesis & lethality

Previous work in our labs performed by Drs. Natasha Sheybani and Aly Witter showed that combinatorial treatment of 4T1 TNBC tumors with TFUS+GEM constrained primary tumor outgrowth and significantly extended the overall survival of tumor-bearing mice. This effect was mediated by T-cells[84]. GEM has been shown to have myeloablative effects on GR-1$^+$ MDSCs in the spleens, blood, and bone marrow of 4T1 tumor-bearing mice[88], so we hypothesized that GEM augments tumor immunity in this setting by alleviating MDSC presence and immunosuppression in the TME. To test the role of MDSCs directing, we aimed to employ mAbs to more specifically deplete these populations and determine whether these mAbs synergize in a similar fashion with

TFUS as GEM did. We utilized anti-Ly6G and anti-GR1 to target the G-MDSC population primarily, as it accounts for majority of total live immune cells in the 4T1 TME (cite gem paper, 31). However, infusion of 100 μg of anti-Ly6G or 250 μg of anti-GR1 into 4T1 tumor-bearing, but not tumor-free Balb/c mice, induced high levels of toxicity. We predicted that because the tumor-bearing mice have increased levels of myelopoiesis resulting in splenomegaly, the administration of high doses of myeloid depleting mAbs induced a toxic amount of cell death. We first performed titration experiments to reduce toxicity, while still ensuring depletion of MDSCs was established. When we compared 3-doses of 25 μg or 50 μg injections of a **α**Ly6G (Figure 5-1A), we found that both doses were able to significantly reduce neutrophil presence in circulation by Complete Blood Count (CBC) analysis (Figure 5-1B-C) when compared to the IgG controls. We then looked at granulocytic cell presence in the tumors and spleens of 4T1 tumor-bearing mice, and we observed that both **α**Ly6G doses significantly lowered the number of granulocytes present in the TME and spleens (Figure 5-1D-E, respectively). Given that there was no difference in the level of depletion with the 25 μg or 50 μg doses of a **α**Ly6G, we opted to proceed with the lower 25 μg dosage. We then compared the efficacy of **α**Ly6G to two different doses amounts of **α**GR1, which has cross reactivity with both Ly6G and Ly6C (Fleming), the differentiation markers of granulocytic and monocytic cells, respectively. Because of this, we hypothesized that **α**GR1 would allow us to target both the G- and M-MDSC populations. When we administered the depleting mAbs in the same 3-dosing scheme used for the **α**Ly6G (Figure 5-1F), we observed no difference in tumor outgrowth (Figure 5-1G). While both mAbs effectively depleted the circulating granulocyte population (Figure 5-1H-I), only **α**GR1 – particularly the higher 75 μg doses – significantly impacted the presence of Ly6C

expressing monocytes and Ly6C^{hi} cells in circulation (Figure 5-1J-M), which we deemed inflammatory monocytes for their high expression of Ly6C[150]

Ultimately, our goal was to prolong depletion of suppressive MDSCs to study their role in conferring TFUS+GEM tumor control and survival advantage. Now that we have a dosing strategy to acutely deplete MDSCs, we next tested whether administering a higher "maintenance" dose of either **α**Ly6G (25 μg or 100 μg) or **α**GR1(25 μg or 100 μg) following established depletion could sustain the loss of granulocytic cells and monocytic cells in the case of **α**GR1 (Figure 5-2A). However, two days following the maintenance dose, there was no difference in the number of granulocytes, monocytes, or inflammatory monocytes in circulation when the mAb cohorts were compared to the IgG controls (Figure 5-2B, D&F, respectively). While proportional alterations within the total live immune cell compartment were observed at this timepoint, they all returned to the baseline IgG levels by D19 (Figure 5-2C, E&G). In addition, we observed some trends of increased granulocyte and inflammatory monocyte cell counts 5 days following that last mAb injection (Figure 5-2B&F); suggesting that accelerated myelopoiesis may be occurring in response to mAb-induced attenuation of the myeloid compartment. When we proceeded with a second maintenance dose on D20, all mice that received any amount of depletion mAbs died shortly after receiving the treatment. Therefore, we were unable to alleviate toxicity or sustain depletion of these myeloid cells by administering larger maintenance doses following primed depletion with the low dose mAbs.

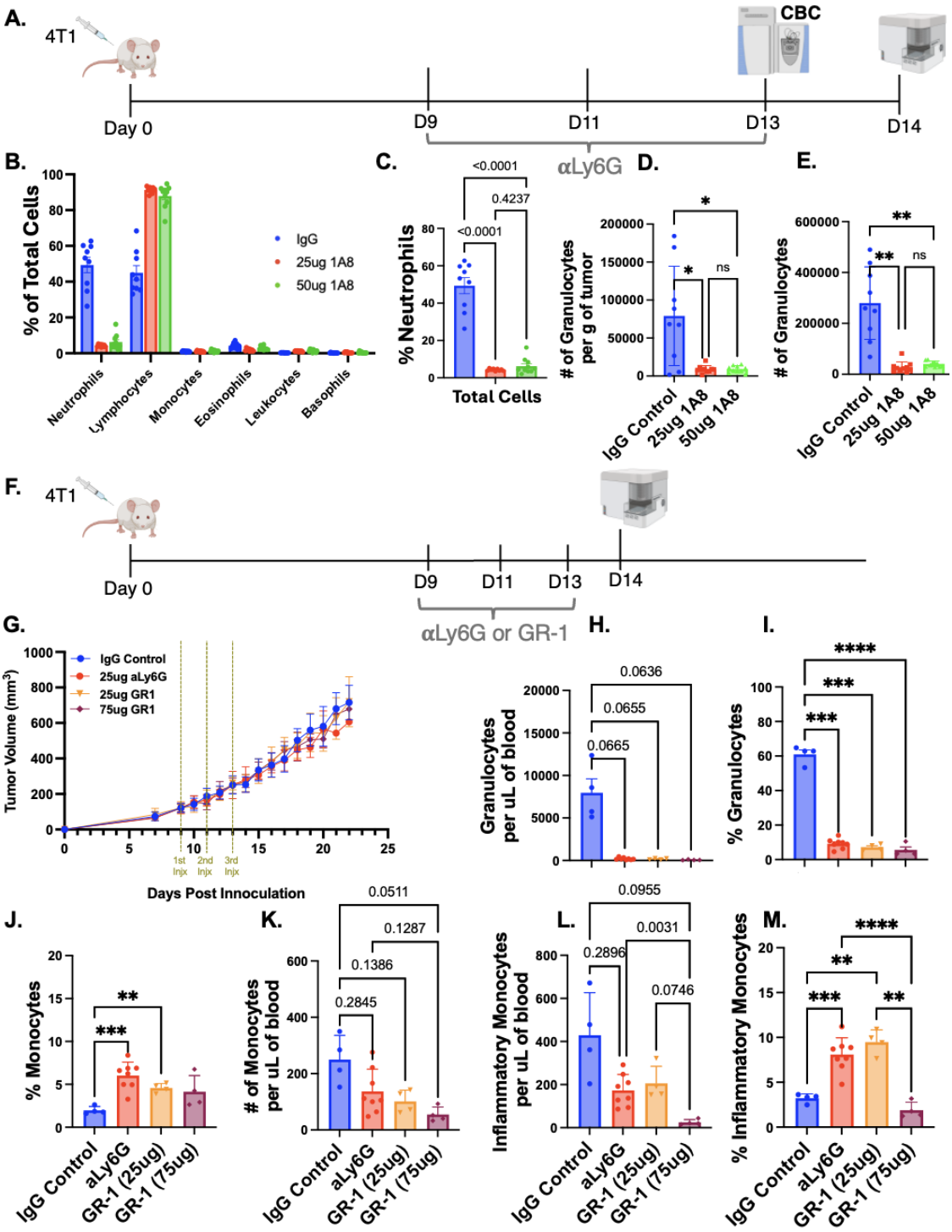

Figure 5-1. Reduced doses of myeloid depleting antibodies can establish depletion acutely, while avoiding toxicity to 4T1 tumor-bearing mice. A. Schematic for experimental timeline from tumor initiation to **α**Ly6G depletion followed by CBC analysis and 24 h flow cytometry analysis of the tumors and spleens. **B.** Summary of CBC with differential proportions following **α**Ly6G administration. **C.** Zoomed in graph of CBC with differential focused on the neutrophil population following **α**Ly6G administration. D&E. Bar graphs showing the number of granulocytes in the tumors **(C)** or spleens **(D)** post **α**Ly6G. (n=8-9) **F.** Schematic for experimental timeline from tumor initiation to **α**Ly6G or GR1 depletion followed by 24 h flow cytometry analysis of the blood. **G.** Average tumor growth curves for mice treated with depleting antibodies [25 µg **α**Ly6G, 25 µg **α**GR1, or 50 µg **α**GR1] or IgG control. **H&I.** Bar graphs showing the number **(H)** and proportion **(I)** of live immune cells in circulation that are granulocytes. **J&K.** Bar graphs showing the number **(J)** and proportion **(K)** of live immune cells in circulation that are monocytes. L&M. Bar graphs showing the number **(L)** and proportion **(M)** of live immune cells in circulation that are Ly6C^{hi} inflammatory monocytes. (n=4-8) One-way ANOVA with Brown-Forsythe correction & multiple comparisons: ns = nonsignificant, * P<0.05; ** P<0.01, *** P<0.001, **** P<0.0001; Mean ± SD. ROUT Outliers analysis with Q=0.1%.

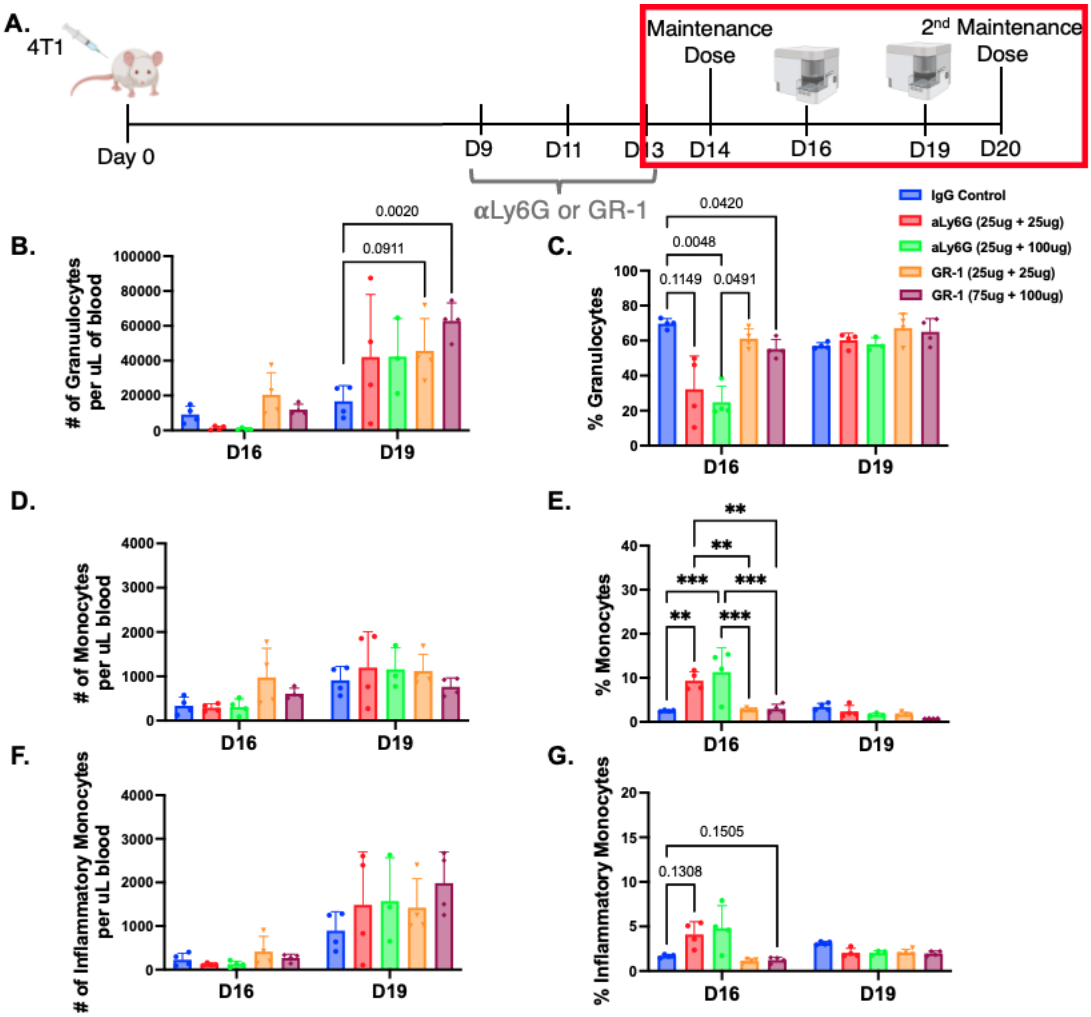

Figure 5-2. Administering a larger maintenance dose of depleting antibodies once depletion had been established with 3-low dose injections did not result in sustained loss of granulocytic or monocytic populations. A. Schematic for experimental timeline from tumor initiation to low dose **α**Ly6G or GR1 depletion D9-D13, followed by a larger maintenance dose on D14 with D16 and D19 bleeds to assess whether depletion is maintained by flow cytometry. **B&C.** Bar graphs showing the number **(B)** and proportion (**C**) of live immune cells in circulation that are granulocytes. **D&E.** Quantification of the number **(D)** and proportion **(E)** of live immune cells in circulation that are monocytes. **F&G.** Quantification of the number **(F)** and proportion **(G)** of live immune cells in circulation that are inflammatory monocytes. (n=4) Mixed effects model with multiple comparisons: ** P<0.01, *** P<0.001; Mean ± SD. ROUT Outliers analysis with Q=0.1%.

Given that the larger maintenance doses proved ineffective in sustaining MDSC depletion and reducing mAb-induced lethality, we then hypothesized whether depletion could be maintained by administering consistent low doses of **α**GR1 (25 µg) every other day from D9-D21 (Figure 5-3A). While there was no significant difference in 4T1 tumor outgrowth between

the IgG and **α**GR1 treated cohorts, the slope of the **α**GR1 growth curve was higher than that of the IgG cohort, suggesting that the **α**GR1-treated tumors were growing faster than the IgG-treated (Figure 5-3B). This is more evident when looking at the individual growth curves where 4/6 tumors in the **α**GR1group experienced larger outgrowth than the IgG tumors (Figure 5-3C-D). When we assessed the presence of $CD11b^+$ myeloid cells in circulation on D16, one week following the start of **α**GR1 administration, we found that there were significantly more myeloid cells in the blood of **α**GR1 treated mice; suggesting that these tumor-bearing mice are overcoming the depletion of MDSCs and inducing emergency myelopoiesis to repopulate these cells. This process is complex and can be driven by inflammatory cytokines – such as TNF-**α**, IL-6, type I and II interferons, IL-1-α/β – as well as TLR signaling and colony stimulating factors, which hematopoietic stem cell expansion and differentiation into immature suppressive myeloid cells[151]. In a last attempt to overcome the effects of the emergency myelopoiesis, we tested whether the optimized **α**Ly6G based combo depletion strategy developed by *Boivin et al*[152] – in which they administered **α**Ly6G everyday with subsequent **α**Rat kappa light chain every other day to accelerate the turnover of *in vivo* **α**Ly6G and increase the speed of targeted cell death – would allow us to maintain depletion of granulocytic cells in in the 4T1 model. While *Boivin et al* had success using this combination approach in sustaining durable depletion of granulocytic cells in lung adenocarcinoma models, this strategy was ineffective in maintaining depletion in the 4T1 TNBC model and eventually proved lethal after 9-10 days of this mAb regimen. Due to the continued lethality and toxicity concerns, as well as the inability to maintain MDSC depletion, we concluded that these mAbs are not an appropriate tool to use in the 4T1 model to study the effects of MDSC presence and their role in TFUS+GEM's therapeutic efficacy.

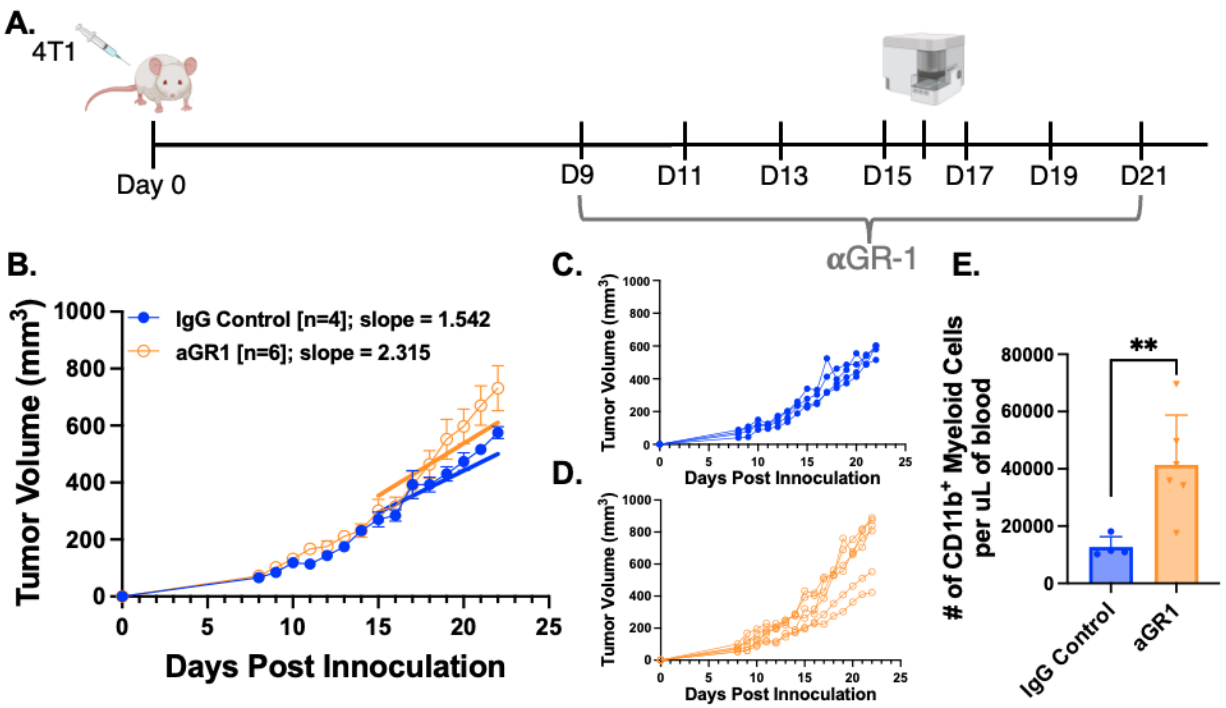

Figure 5-3. Depletion efficacy cannot be maintained by giving consistent low dose injections of αGR1. A. Schematic for experimental timeline from tumor initiation to 25 µg αGR1 depletions every other day beginning on D9-D21, with flow cytometry analysis of blood on D16 **B.** Average tumor growth curves for mice treated with continued 25 µg αGR1, or IgG control. Mean ± SEM **C&D.** Individual tumor growth curves of IgG **(C)** or αGR1 **(D)** treated mice. **E.** Bar graph showing the number of $CD11b^+$ myeloid cells in circulation 7 days post start of antibody administration. (n=4-6) Simple linear regression model on tumor outgrowth from D15-D22 **(B).** Unpaired t test with Welch's correction: ** $P<0.01$; Mean ± SD **(E).** ROUT Outliers analysis with Q=0.1%.

Modifying TFUS+GEM treatment parameters lead to loss of T-cell-mediated control of primary TNBC outgrowth

While we have previously reported that TFUS+GEM dual therapy constrains primary tumor growth and extends survival in mice with TNBC in a T-cell dependent manner[84], the basis of enhanced T-cell control initiated by TFUS+GEM is unclear. First, we sought to test whether $CD8^+$, $CD4^+$, or both T-cell subsets were required for sustained growth control induced by TFUS+GEM. The prior work had utilized a partially ablative TFUS regimen, in which two ablation planes within s.c. 4T1 murine TNBC tumors were treated with 1mm-spaced TFUS. As

we began the subsequent studies, we were experiencing high levels of toxicity with this TFUS regimen. We hypothesized that if we increased the space between ablation points, we could reduce toxicity while maintaining efficacy of the dual therapy's growth control because we would be 1) shortening the amount of time each mouse is undergoing treatment and anesthesia, and 2) reducing the amount of heat being generated and dissipated in the tumors from the continuous, high intensity sound waves. To test this, we performed TFUS utilizing 2mm-, 3mm- and 4mm-speaced ablation regimens, and compared tumor outgrowth to Sham control treated mice. This was done on a GEM background, so that we could determine whether different ablative fractions still synergized with GEM, while minimizing toxicity. While we found that all TFUS+GEM regimens were able to better constrain tumor outgrowth compared to GEM monotherapy alone, the majority of the 2mm-spaced TFUS treated mice had to be euthanized prior to the end point due to morbidity and toxicity issues. They either experienced double hindlimb paralysis or did not regain consciousness following treatment. We hypothesize that the death may be due in part to a cytokine storm resulting from the heating and cell destruction induced. Conversely, the 3mm- and 4mm-TFUS cohorts were healthy – no eye squinting, no reduced activity, well-groomed coats, no weight loss – and experienced a reduced frequency of off target heating effects, such as hindlimb paralysis. When comparing tumor growth between the 3mm- and 4mm- groups, we found that the 3mm-TFUS spacing regimen was better able to control 4T1 outgrowth (Figure 5-4). Therefore, subsequent TFUS experiments were performed utilizing 3mm-spaced regimen.

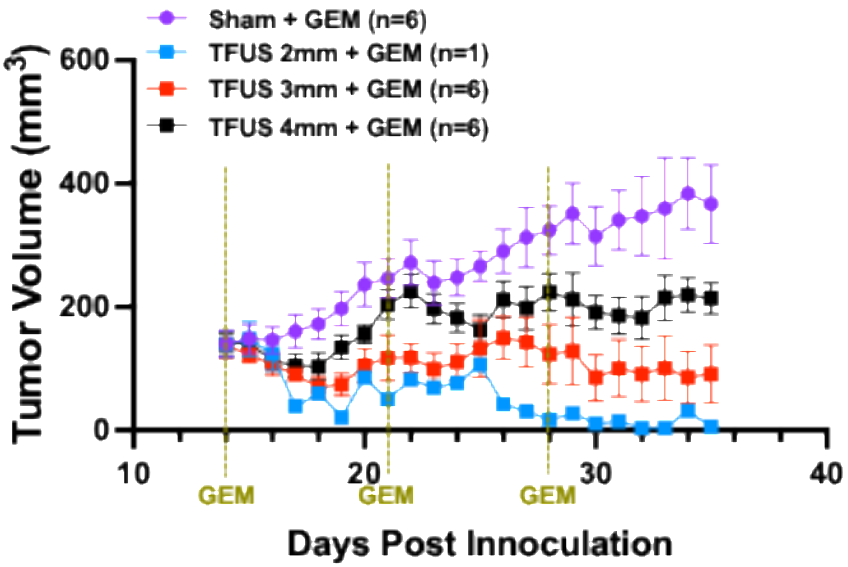

Figure 5-4. Increasing the distance between TFUS treatment points reduces the efficacy of TFUS+GEM mediated growth control. Average tumor growth curves for mice treated with 2mm-, 3mm-, or 4mm-spaced TFUS combined with GEM (1.2mg) treatment given I.P. on days 14, 21 and 28 post inoculation. All points represent mean ± SEM.

Once we had a TFUS+GEM treatment that mimicked the outgrowth observed previously[84], we determined whether $CD8^+$ and/or $CD4^+$ T cells were mediating control of tumor growth and prolonged survival. We found that neither depletion of $CD8^+$, $CD4^+$, or a combination of both T-cell subsets resulted in loss of tumor control by 3mm-spaced TFUS+GEM (Figure 5-5A). It is of note that in this study we used GEM from the vendor Hospira, while the prior studies were done with GEM manufactured by Mylan. When examining the efficacy of GEM as a monotherapy, we noticed that the 3-dose regimen of GEM used here resulted in more sustained tumor growth control and longer median survival than the previous published studies[84]. This suggests that this new source of the chemotherapy may be more potent, and future studies may be required to titrate this brand of GEM so that its efficacy better resembles the preceding findings. Additionally, when we compared the survival curves of T-cell depleted vs T-cell intact TFUS+GEM treated cohorts, we observed significant reductions in survival for tumor-bearing

mice depleted of $CD8^+$ T-cells, but no significant difference in $CD4^+$ alone depleted cohort (Figure5-5B). Because the 4T1 TNBC model spontaneously metastasizes, we hypothesize that 3mm-spaced TFUS+GEM may be alleviating metastatic burden in a $CD8^+$-dependent manner, while constraining primary TNBC by debulking the tumor independent of T-cells. Based on the focal zone of our transducer, we modelled and estimated the ablation fraction, i.e. how much of the tumor we are treating with TFUS, based on the number of ablative points we applied. 1mm-spaced TFUS regimen was estimated to ablate ~20-30% of the tumor, while the 3mm-spaced TFUS regimen ablates only ~5% of the tumor tissue. This significant decrease in ablation fraction, which results in the persistence of a larger proportion of viable tumor cells, could explain why we did not observe a significant difference in survival between the dual-combination 3mm-TFUS+GEM cohort when compared to the Sham+GEM monotherapy group (Figure 5-5B).

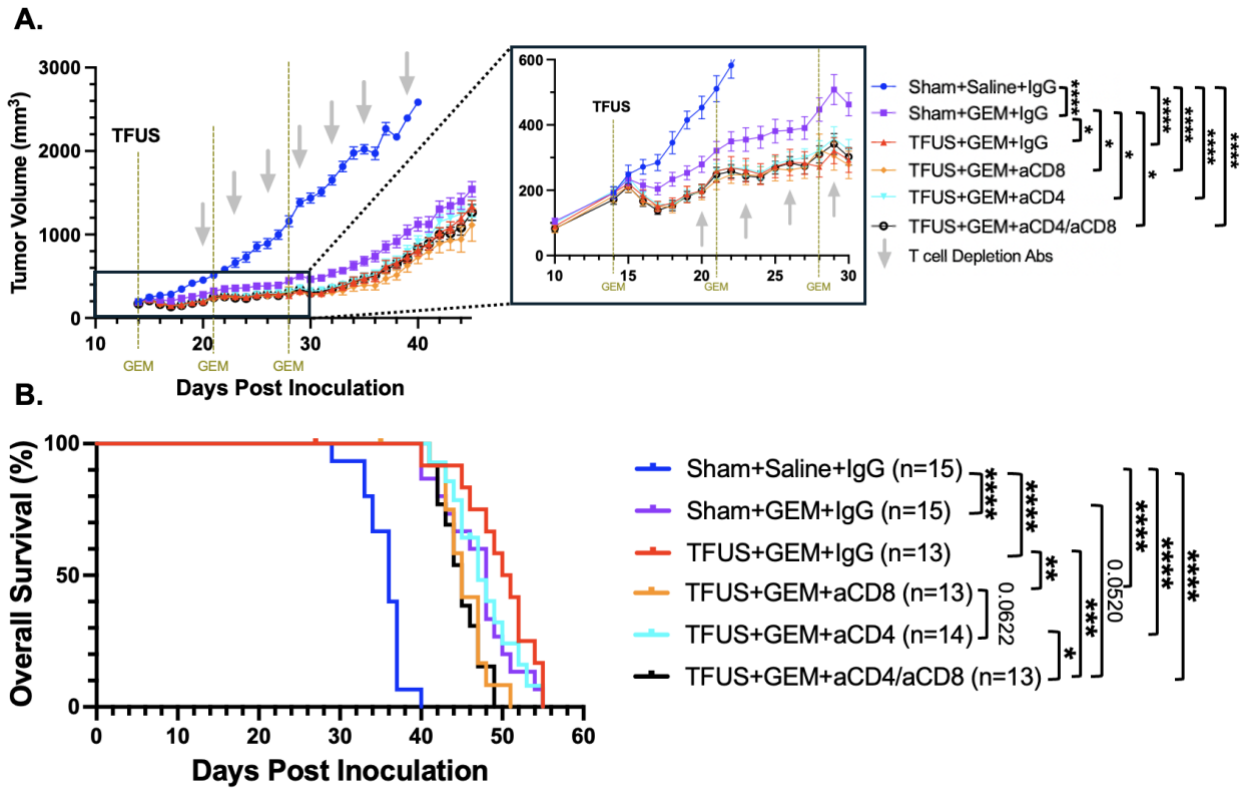

Figure 5-5. 3mm-spaced TFUS+GEM primary tumor control is not mediated by T cells, while survival is significantly shortened in the absence of T cells. A. Average tumor growth curves for mice treated with Sham or 3mm-spaced TFUS combined with GEM (1.2mg) treatment given I.P. on days 14, 21 and 28 post inoculation. 200 µg total of T cell depletion antibodies [anti-CD4 (GK1.5) and anti-CD8 (2.43)] or IgG isotype control was administered on days 20, 23, 26, 29, 32, 35 and 39. (Mixed-effects model: ∗ P<0.05, ∗∗∗∗ P<0.0001). All points represent mean ± SEM. **B.** Kaplan-Meier curve depicting overall survival (significance assessed by log-rank (Mantel-Cox) test: ∗ P<0.05, ∗∗ P<0.01, ∗∗∗ P<0.001, ∗∗∗∗ P<0.0001).

1mm- vs 3mm-TFUS regimens result in differential RNA transcript expression 24 h and 168 h (7 days) post TFUS

The discrepancies we observed between the study described above and those reported in the past, lead us to question whether 1mm-spaced TFUS was inducing a more potent immune response than the less ablative 3mm- TFUS regimen. To test this, we performed RNA-sequencing on 4T1 murine TNBC tumors that had previously been treated with 1mm- or 3mm-spaced TFUS and collected 24h and 168 h (7 days) post TFUS. From this data, we were able to

assess gene expression profiles within these tumors exposed to different ablation fractions. Estimation of the similarities and differences in differentially expressed genes (DEGs) resulting from the two TFUS ablations regimens when compared to their respective Sham controls determined that significantly more genes were differentially expressed by 1mm- TFUS 24 h post treatment (4,225 genes), with only 7% of DEGs being shared between the two TFUS regimens (Figure 5-6A). DEGs persisted in the 1mm-TFUS setting one week post treatment, while less than 0.5% (8/1845) of DEGs were observed in the tumors that received 3mm-TFUS 168 h following treatment (Figure 5-6B). We also performed gene ontology analysis to understand which pathways in the hallmark data set are modulated by 1mm- or 3mm-TFUS when compared to their respective Sham samples sequenced at the time of their individual run (Figure 5-7). When we compared pathways that were conserved (outlined in pink) to pathways that were not both up- or downregulated by 1mm- and 3mm-TFUS, we found that pathways associated with immune activation, such as interferon gamma response and inflammatory response, were upregulated in the 1mm-TFUS cohort (Figure 5-7A) and downregulated in the 3mm-TFUS setting (Figure 5-7B). 1mm-TFUS also downregulated expression of genes associated with TGF-β signaling, which would indicate that at the transcriptional level, 1mm-TFUS may be alleviating immunosuppression through reduced expression of TGF-β related genes. By 168 h post TFUS, we observed that most pathways upregulated following the less ablative 3mm-TFUS regimen were conserved and also upregulated in the 1mm-TFUS setting, while the 1mm-TFUS treated tumors experienced a larger number of transcriptional altered pathways that the 3-mm TFUS tumors when compared to their respective Sham control tumors at this timepoint, 7 days post treatment (Figure 5-8). We performed CIBERSORTx analysis to estimate the immune landscapes of the TNBC tumors treated with the two different TFUS regimens. Acutely (24 h) post therapy,

1mm-TFUS suggested an increased presence of neutrophils in the TME (Figure 5-9A), which were no longer elevated 168 h post treatment (Figure 5-9B). When comparing the 168 h immune landscapes, considerable differences in the immune landscape of the TME emerge. In the 1mm-TFUS cohort, we found a greater proportional presence of resting dendritic cells, but also higher M2-like, pro-tumorigenic macrophage abundance, while $CD4^+$ T cell subsets are expanded in the 3mm-TFUS tumors compared to the 1mm-ablated tumors (Figure 5-9B).

In all, this data suggests that thermally ablating more of the tumor not only results in sustained transcriptional changes within the treated tumors themselves but also may be inducing a more prominent immunological response the TME. However, it is critical to remember that this data is based on differences at the gene expression level. These findings would need to be further validated at the protein and cellular levels to confirm alterations in immune cell phenotypes and functions. Also, although TFUS is a different ablative regimen, these findings again bring up the notion described in chapter four of fine-tuning the high-intense sound waves for more favorable immunological effects.

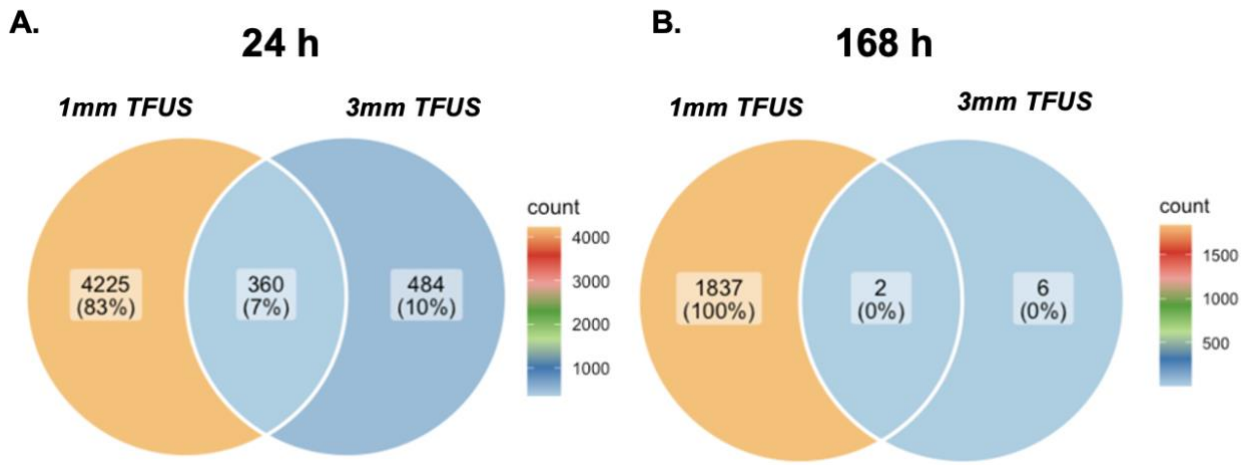

Figure 5-6. 1mm- vs 3mm-spaced TFUS regimens result in differential RNA transcript expression in TNBC tumors 24 h and 168 h (7 days) post ablation. 4T1 tumors were treated with TFUS at either 5% (3mm-spaced) or 20% (1mm-spaced) ablation fraction. Tumors (n=4-8) were excised 24 h or 168 h after TFUS, and RNA was extracted for bulk sequencing by the UVA GATC Shared Resource. UVA Bioinformatics Shared Resource performed data clean up and false-discovery filtering. **A.** Genes that were differentially expressed at >Log2(2) an $p<0.05$ were identified and represented in Venn-diagrams for the 24 h. **B.** Genes that were differentially expressed at >Log2(2) an $p<0.05$ were identified and represented in Venn-diagrams for the 168 h timepoint.

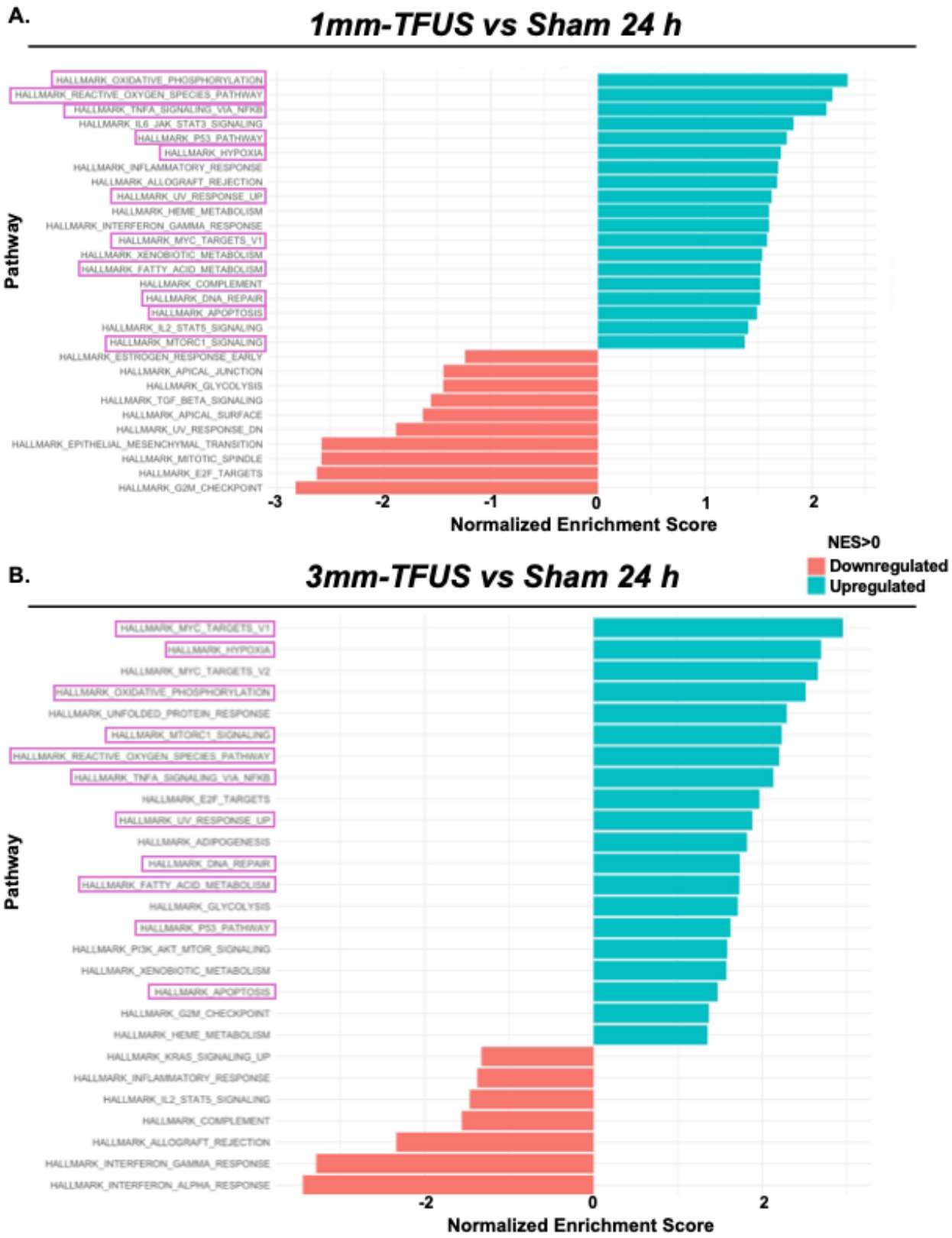

Figure 5-7. 1mm-TFUS upregulates pathways associated with immune activation, while 3mm-spaced TFUS down regulates these pathways. A&B. Gene ontology analysis showing normalized enrichment scores for the hallmark pathways modulated in 1mm-TFUS **(A)** or 3mm-TFUS **(B)** treated tumors compared to their respective Sham control cohort 24 h post treatment. The pink boxes denote conserved pathways between both regimens.

Figure 5-8. A week post ablation, 1mm-TFUS treated tumors have a larger number of differentially expressed pathways when compared to their respective Sham cohort, than the 3-mm TFUS treated tumors. A&B. Gene ontology analysis showing normalized enrichment scores for the hallmark pathways modulated in 1mm-TFUS **(A)** or 3mm-TFUS **(B)** treated tumors compared to their respective Sham control cohort 168 h post treatment. The pink boxes denote conserved pathways between both regimens.

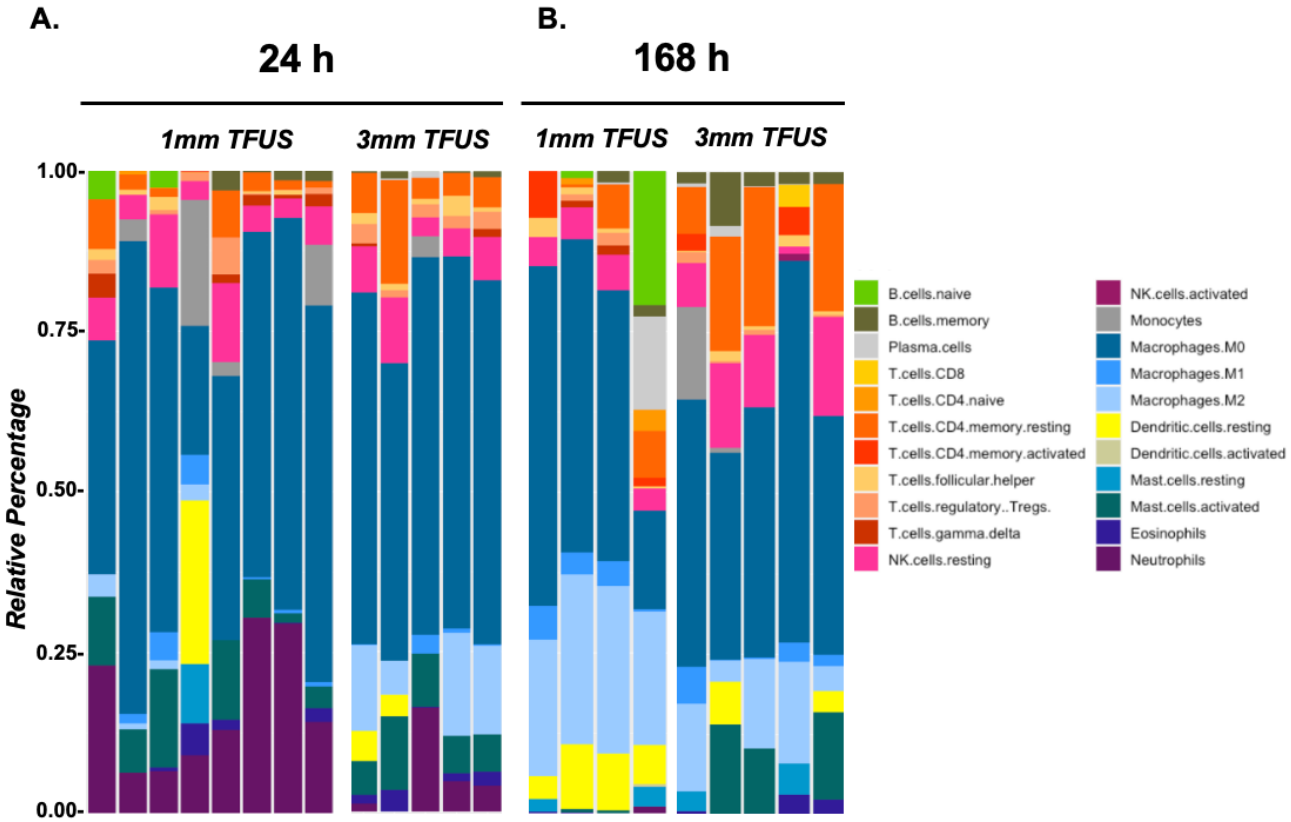

Figure 5-9. CIBERSORTx deconvolution analysis depicts the immune landscape of 4T1 tumors 24 h (A) or 168 h (B) post 1mm- or 3mm-spaced TFUS.

Different brands of GEM induce differential RNA transcript expression in TNBC tumors 24 h and 168 h post systemic administration

In addition to the discrepancies we observed between the different TFUS ablation regimens, we had previously noted dissimilarities between the substituted brand of GEM used in the studies described earlier in this chapter when comparing tumor outgrowth and median survival to the prior published work[84]. To gain insight into the opposing outcomes, we next tested whether the different brands of GEM induced different transcriptional changes in these 4T1 tumors. Through bulk RNA-sequencing, we examined gene expression levels in these TNBC tumors 24 h and 168 h post GEM administration, and visualized similarities and differences in DEGs resulting from GEM treatment when compared to their respective saline

controls. We found that significantly more genes were differentially expressed by the newer Hospira brand of GEM 24 h following administration of the chemotherapy (174 genes), with only 3% of DEGs being shared between the two GEMs (Figure 5-10A), and DEGs persisted in the tumors that received Hospira manufactured GEM one week post treatment (Figure 5-10B), despite equivalent amounts of GEM being provided to the mice. Through gene otology analysis, we were able to observe conserved pathways in the tumors of both GEM treated cohorts that are associated with the administration of a chemotherapeutic agent – such as the upregulation of DNA repair and p53 as well as the downregulation of genes related to the G2M checkpoint and mitotic spindle – indications of cell cycle arrest and cell death. Additionally, there was a significant upregulation 24 h post treatment in immune related pathways such as interferon gamma response and interferon alpha response in tumors that received Hospira manufactured GEM, which were not observed in Mylan GEM treated tumors (Figure 5-11). Interestingly, when we examined these TNBC tumors one week following systemic chemotherapy, immune-related pathways were significantly upregulated by both GEMs; suggesting that the two chemotherapies may both be enhancing immune activation, but the Hospira GEM may be more potent at initiating activation earlier in the TME (Figure 5-12).

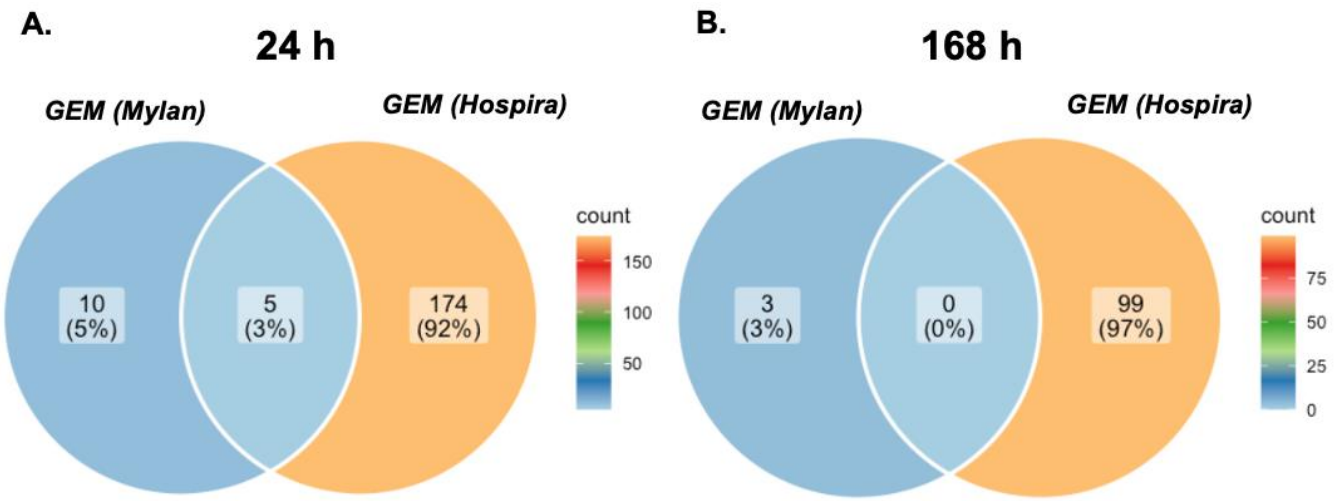

Figure 5-10. Different brands of GEM induced differential RNA transcript expression in TNBC tumors 24 h and 168 h (7 days) post systemic administration. 4T1 tumor-bearing mice received a single i.p. injection of 1.2mg of GEM or saline vehicle control. Tumors (n=4-8) were excised 24 h or 168 h after TFUS, and RNA was extracted for bulk sequencing by the UVA GATC Shared Resource. UVA Bioinformatics Shared Resource performed data clean up and false-discovery filtering. **A&B.** Genes that were differentially expressed at >Log2(2) an $p<0.05$ were identified and represented in Venn-diagrams for 24 h **(A)** and 168 h **(B)** post administration.

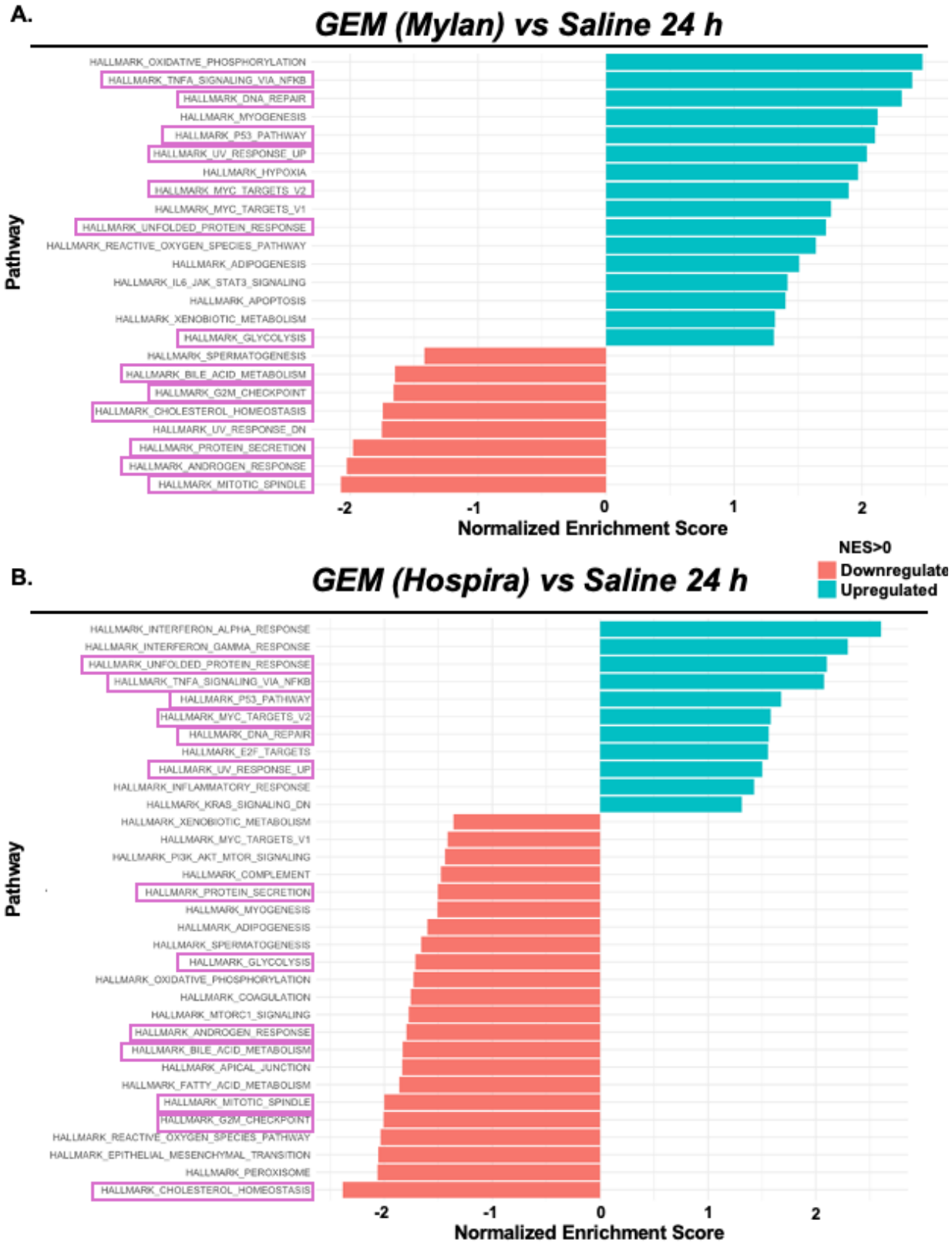

Figure 5-11. While conserved pathways indicative of chemotherapeutic administration are found in both GEM cohorts, Hospira manufactured GEM upregulates pathways associated with immune activation. A&B Gene ontology analysis showing normalized enrichment scores for the hallmark pathways modulated in GEM (Mylan) **(A)** or GEM (Hospira) **(B)** treated tumors compared to their respective Sham control cohort 24 h post treatment. The pink boxes denote conserved pathways between both regimens.

Figure 5-12. Immunological pathways in the TME are upregulated by both GEMs 168 h post administration. A&B. Gene ontology analysis showing normalized enrichment scores for the hallmark pathways modulated in GEM (Mylan) **(A)** or GEM (Hospira) **(B)** treated tumors compared to their respective Sham control cohort 168 h post treatment. The pink boxes denote conserved pathways between both regimens.

The effects of GEM on immune populations in the TME of 4T1 TNBC tumors

Due to the toxicity issues and the inconsistencies that we observed with the myeloid depleting antibodies, the TFUS ablation regimens, and the different brands of GEM chemotherapy, we decided it was important to discern an unanswered question in the field: how is GEM as a monotherapy impacting the immune environment in TNBC? All these subsequent studies were performed using Hospira manufactured GEM.

1. GEM is not acutely myeloablative in the TME

We have previously reported that the combination of GEM and thermally ablative focused ultrasound on 4T1 tumors results in T-cell-dependent control of tumor outgrowth[84]. We hypothesized that GEM augments tumor immunity in this setting, as GEM has been shown to have myeloablative effects on GR-1$^+$ MDSCs in the spleens, blood, and bone marrow of 4T1 tumor-bearing mice[88]. To dissect numerical changes in immune cells because of GEM administration to mice bearing 4T1 breast tumors, we utilized spectral flow cytometry to identify cell populations in both the myeloid and T-cell compartments. Because the 4T1 murine TNBC model was deployed for all experiments in this study, it is henceforth referred to as "tumor" or "BrCa". Consistent with *Le et al.,* when we compared the spleens of GEM treated mice 24, 48, and 96 h post-injection to those of the saline control group, we observed significant reductions in myeloid subsets, including granulocytes (Ly6G$^+$CD11b$^+$), monocytes (Ly6G$^-$CD11b$^+$F4/80$^-$Ly6C$^+$), macrophages (Ly6G$^-$CD11b$^+$F4/80$^+$Ly6C$^-$), and inflammatory monocytes (Ly6G$^-$CD11b$^+$F4/80$^+$Ly6C^{hi}; Figure 5-13). When enumerating the different myeloid populations, we noticed a specific and drastic reduction in the F4/80$^+$Ly6C^{hi} population, which we deemed inflammatory monocytes for their high expression of Ly6C[150]. The effect of GEM in the spleen is acute, as by 96 h, the number of myeloid cells increased, and there was no longer a

decrease in the proportion of all live immune cells (Live/CD45$^+$) that were granulocytes, monocytes, macrophages, or inflammatory monocytes (Figure 5-13Cii,Dii,Eii,Fii, respectively). Additionally, we observed the same acute, myeloablative properties of GEM on circulating immune cells when we performed a time course study in tumor-bearing mice. However, by 168 h (7 days) after GEM administration, cell numbers returned to the baseline control levels (Figure 5-14).

Given that the immunosuppressive myeloid cell compartment is significantly diminished systemically within 24 h after GEM treatment, we hypothesized that GEM aids in constraining TNBC outgrowth and significantly lengthens the overall survival time of tumor-bearing mice by depleting Ly6G$^+$CD11b$^+$ G-MDSCs in the TME (Figure 5-15). However, when we examined both the number and proportion of granulocytic cells in the TME (Figure 5-16A), we observed no decrease in granulocyte number normalized to the weight of the tumors (Figure 5-16Ci), or the percentage of all live immune cells that are granulocytes (Figure 5-16Cii) when comparing the GEM-treated cohort to the saline controls. In fact, the percentage of granulocytic cells in the TME significantly increased 24 and 48 h after GEM treatment (Figure 5-16Cii), suggesting that the chemotherapy is impacting the presence of other immune cells in the TME. Similar to the granulocytic cells, we found that GEM had no effect on the number of monocytes (Figure 5-16Di) or the number of macrophages (Figure 5-16Ei). Although monocytes and macrophages make up a small proportion of the immune cells present in the 4T1 TME, both populations significantly increased 96 h following GEM (Figure 5-16Dii,Eii, respectively). Unlike the other myeloid subsets, GEM significantly depleted the inflammatory monocyte population within 24 h following administration. However, this effect was acute, as the number of F4/80$^+$Ly6C^{hi} cells

present in the tumors of GEM-treated mice was comparable to that of the saline-treated mice 48 and 96 h post-injection (Figure 5-16Fi-ii).

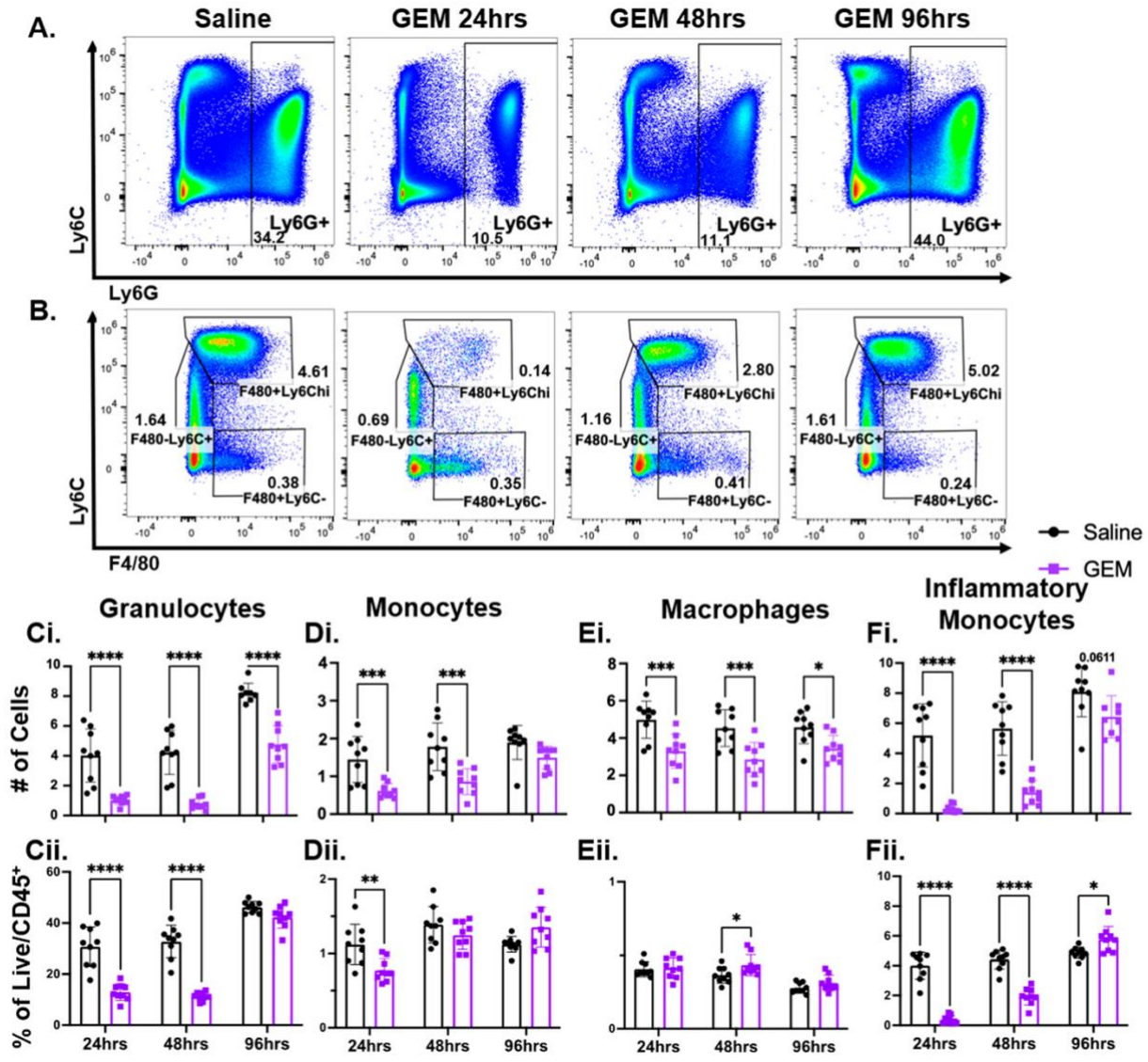

Figure 5-13. Gemcitabine acts as a myeloablative chemotherapy systemically. 350k 4T1 parental cells were inoculated in the right flanks of BALB/c mice. Mice were injected with GEM (1.2mg) or saline I.P. on day 14 post inoculation. Spleens were excised 24, 48 and 96 h post injection **A.** Representative scatter flow plots showing changes in the granulocyte ($CD11b^+Ly6G^+$) population post GEM administration. **B.** Representative flow plots of inflammatory monocytes ($CD11b^+Ly6G^-F4/80^+Ly6C^{hi}$), monocytes ($CD11b^+Ly6G^-F4/80^-Ly6C^+$) and macrophages ($CD11b^+Ly6G^-F4/80^+Ly6C^-$) post GEM injection. All frequencies shown are of the Live/$CD45^+$ population. **C.** Changes in granulocyte number on the order of 10^7 (**Ci**) and proportion (**Cii**) 24, 48 and 96 h post injection. **D.** Changes in monocytes number on the order of 10^6 (**Di**) and proportion (**Dii**). **E.** Changes in macrophages number on the order of 10^5 (**Ei**) and proportion (**Eii**). **F.** Changes in inflammatory monocytes number on the order of 10^6 (**Fi**) and proportion (**Fii**)(n=9) (2way ANOVA with multiple comparisons: ∗ P<0.05, ∗∗ P<0.01, ∗∗∗ P<0.001, ∗∗∗∗ P<0.0001; ROUT Outliers analysis with Q=0.1%). All points represent mean ± SD.

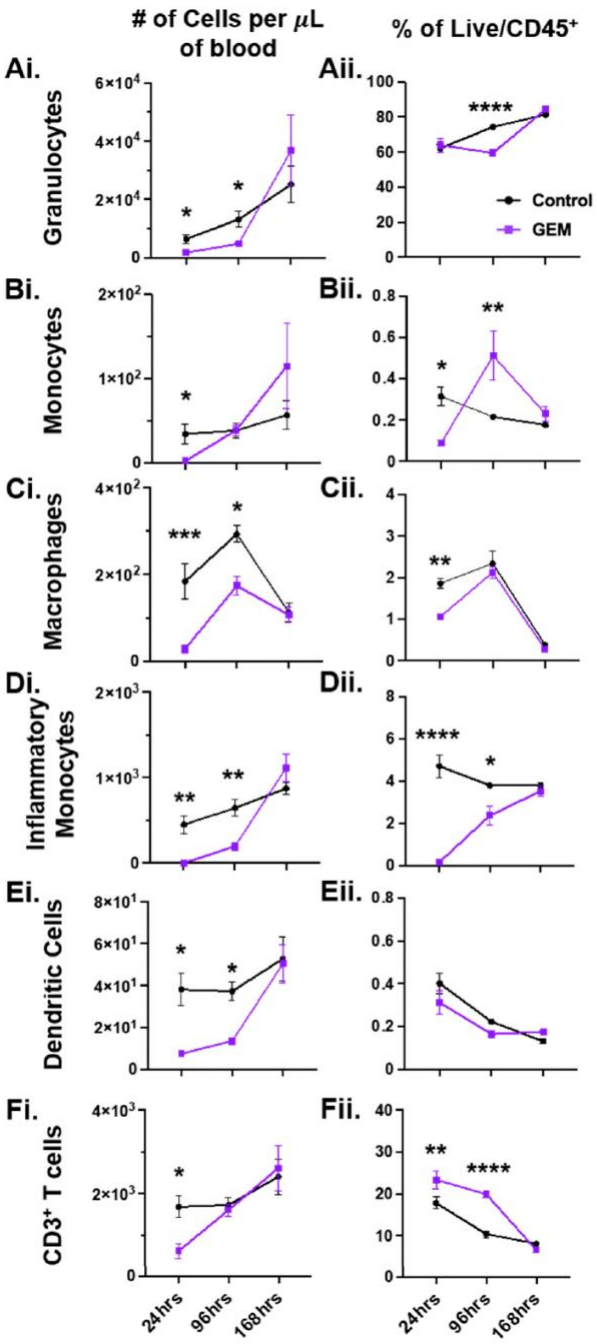

Figure 5-14. Gemcitabine acts as a myeloablative chemotherapy on circulating immune cells. 350k 4T1 parental cells were inoculated in the right flanks of BALB/c mice. Mice were injected with GEM (1.2mg) or control IgG (200μg) I.P. on day 14 post inoculation. Blood was collected 24, 96 and 168hrs (7 days) post GEM. **A.** Changes in granulocyte ($CD11b^+Ly6G^+$) number per μL of blood (**Ai**) and proportion (**Aii**) following GEM administration. **B.** Changes in monocyte ($CD11b^+Ly6G^-F4/80^-Ly6C^+$) number (**Bi**) and proportion (**Bii**). **C.** Changes in macrophage ($CD11b^+Ly6G^-F4/80^+Ly6C^-$) number (**Ci**) and proportion (**Cii**). **D.** Changes in inflammatory monocyte ($CD11b^+Ly6G^-F4/80^+Ly6C^{hi}$) number (**Di**) and proportion (**Dii**). **E.** Changes in dendritic cell ($CD11c^+MHCII^+$) number (**Ei**) and proportion (**Eii**). **F.** Changes in circulating $CD3^+$ T cell number (**Fi**) and proportion (**Fii**) following GEM administration. All frequencies shown are of the Live/$CD45^+$ population. (n=5) (2way ANOVA with multiple comparisons: ∗ P<0.05, ∗∗ P<0.01, ∗∗∗ P<0.001, ∗∗∗∗ P<0.0001; ROUT Outliers analysis with Q=0.1%). All points represent mean ± SEM.

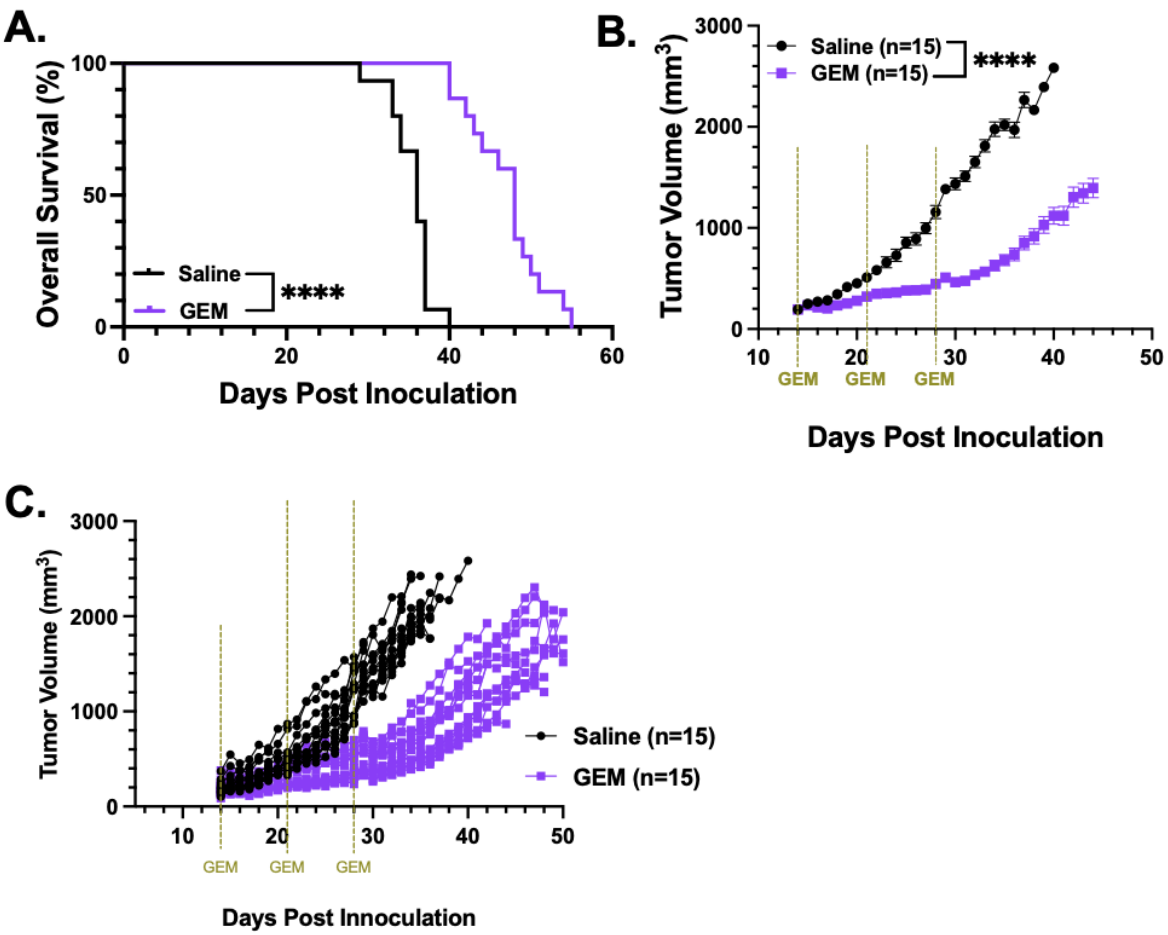

Figure 5-15. Gemcitabine constrains 4T1 tumor outgrowth and significantly improves median survival in tumor-bearing mice. 350k 4T1 parental cells were inoculated in the right flanks of BALB/c mice. Mice were injected with GEM (1.2mg) or saline I.P. on days 14, 21 and 28 post inoculation. **A.** Kaplan-Meier curve depicting overall survival (significance assessed by log-rank (Mantel-Cox) test: **** P<0.0001). **B.** Average tumor growth curves for mice treated with GEM or Saline control. (Mixed-effects model: **** P<0.0001). All points represent mean ± SEM. **C.** Individual tumor growth curves of GEM or Saline treated mice.

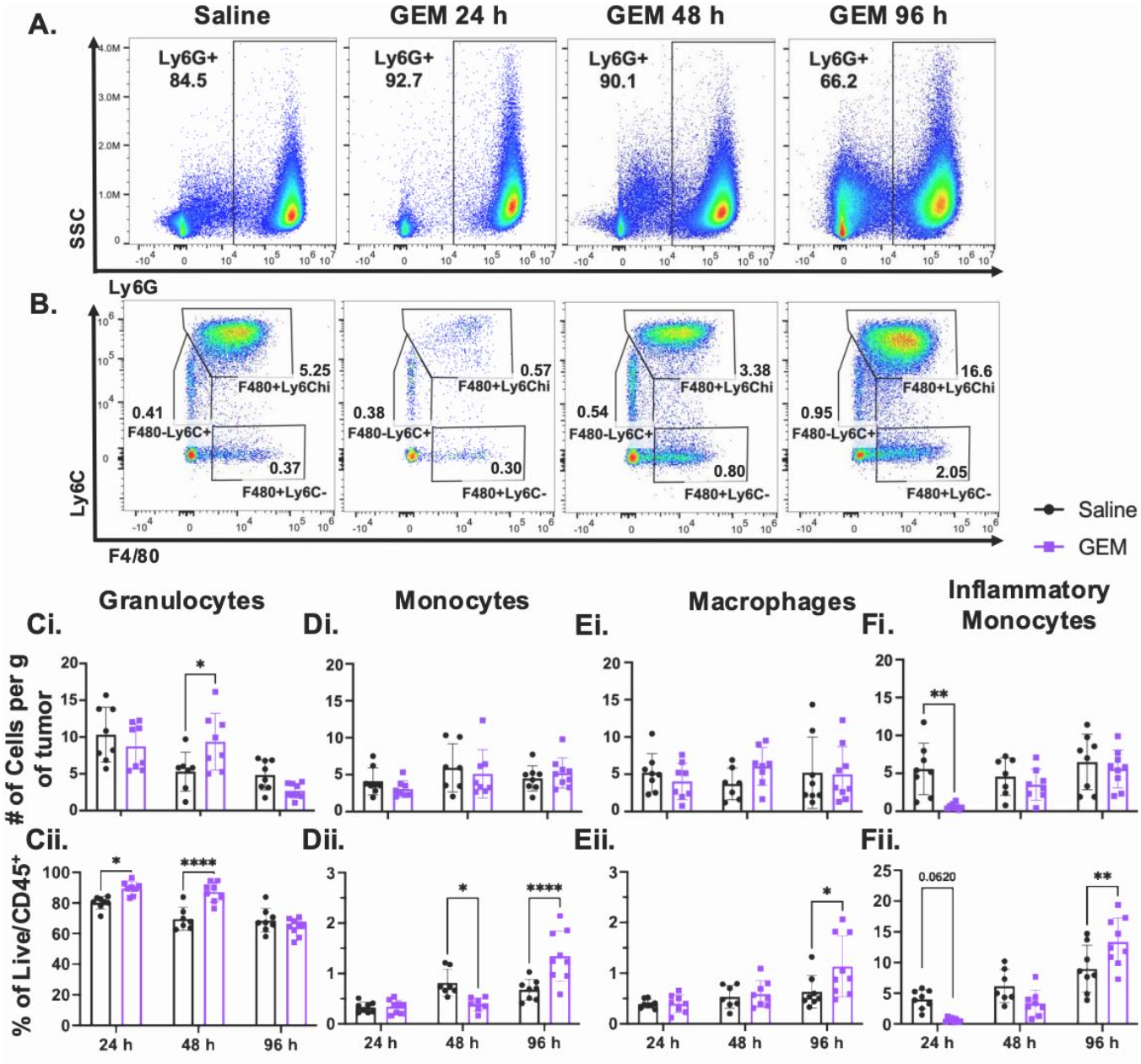

Figure 5-16. Gemcitabine (GEM) does not act as a myeloablative therapy in the 4T1 tumor microenvironment (TME). 350 k 4T1 parental cells were inoculated in the right flanks of BALB/c mice. Mice were injected with GEM (1.2 mg) or saline I.P. on day 14 post inoculation. Tumors were excised 24, 48 and 96 h post injection (**A**). Representative scatter flow plots showing changes in the granulocyte ($CD11b^{+}Ly6G^{+}$) population post GEM administration. (**B**). Representative flow plots of inflammatory monocytes ($CD11b^{+}Ly6G^{-}F4/80^{+}Ly6C^{hi}$), monocytes ($CD11b^{+}Ly6G^{-}F4/80^{-}Ly6C^{+}$) and macrophages ($CD11b^{+}Ly6G^{-}F4/80^{+}Ly6C^{-}$) post GEM injection. All frequencies shown are of the Live/$CD45^{+}$ population. (**C**). Changes in granulocyte number on the order of 10^{5} (**Ci**) and proportion (**Cii**) 24, 48 and 96 h post injection. (**D**). Changes in monocyte number on the order of 10^{3} (**Di**) and proportion (**Dii**). (**E**). Changes in macrophage number on the order of 10^{3} (**Ei**) and proportion (**Eii**). (**F**). Changes in inflammatory monocytes number on the order of 10^{4} (**Fi**) and proportion (**Fii**). (n = 9) (2way ANOVA with multiple comparisons: * $p < 0.05$, ** $p < 0.01$, **** $p < 0.0001$; ROUT Outliers analysis with Q = 0.1%). All points represent mean ± SD.

As an antimetabolite nucleoside analog, GEM acts directly on replicating cells. We predicted that GEM may be preferentially depleting the inflammatory monocytes if the other myeloid subsets are terminally differentiated and the $F4/80^{+}Ly6C^{hi}$ cells are more proliferative. However, when we examined proliferation status with Ki67 staining on tumoral myeloid cells, we found that a high proportion (≈80%) of the granulocytic cells in the TME were $Ki67^{+}$ (Figure 5-17Bii). While the majority of the $Ly6G^{+}CD11b^{+}$ cells were $Ki67^{+}$, their overall presence in the TME was not impacted by GEM. Similar findings were observed in the monocyte and macrophage populations as well (Figure 5-17Cii,Dii, respectively). Therefore, cell replication is not the only factor impacting the ablative effects of GEM on immune cell subsets.

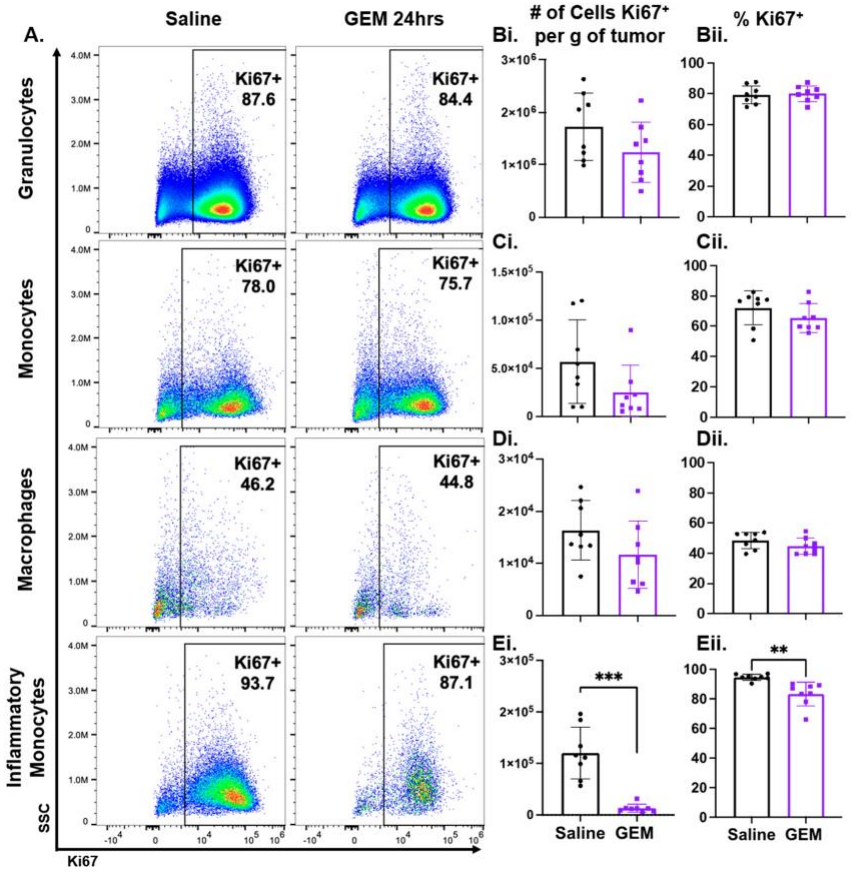

Figure 5-17. Proliferation status of tumoral myeloid subsets & the effects of GEM on these Ki67$^+$ cells. 350k 4T1 parental cells were inoculated in the right flanks of BALB/c mice. Mice were injected with GEM (1.2mg) or saline I.P. on day 14 post inoculation. Tumors were excised 24 post injection **A.** Representative scatter flow plots showing Ki67$^+$ granulocytes, monocytes, macrophages and inflammatory monocytes in saline and GEM treated tumors. All frequencies shown are of the parent population. **B.** Changes in Ki67$^+$ granulocyte number (**Bi**) and proportion Ki67$^+$ (**Bii**). **C.** Changes in Ki67$^+$ monocyte number (**Ci**) and proportion Ki67$^+$ (**Cii**). **D.** Changes in Ki67$^+$ macrophage number (**Di**) and proportion Ki67$^+$ (**Dii**). **E.** Changes in Ki67$^+$ inflammatory monocyte number (**Ei**) and proportion Ki67$^+$ (**Eii**). (n=8) (Unpaired t test with Welch's correction: ∗ P<0.05, ∗∗ P<0.01, ∗∗∗ P<0.001; ROUT Outliers analysis with Q=0.1%). All points represent mean ± SD.

2. GEM significantly lowered the abundance of TILs and dendritic cells in the TNBC TME

A risk of administering systemic chemotherapy to patients in the attempt to promote tumor immunity is the non-specific nature of these drugs, and the potential induction of lymphopenia. In the periphery, GEM has been shown to have limited impact on T cell presence[145,146]. Time course analysis of blood and spleens from tumor-bearing mice that either received GEM or vehicle control confirmed the mild effects of GEM on T cell numbers (Figures 5-14Fi 5-18D-Fi,

respectively). In fact, the proportion of total live immune cells that are T-lymphocytes was significantly higher in the GEM-treated cohort (Figures 5-14Fii and 5-18D–Fii). Because the presence of TILs is correlated with positive prognosis for TNBC patients, we investigated the impact of GEM on the presence of T cells within the tumor. Although GEM has a short tissue half-life in mice (≈3 h)[153], we observed a sustained significant reduction in $CD8\alpha^+$ T cell presence in GEM-treated tumors compared to the saline controls (Figure 5-19A,Di,Dii). Although not as striking, $CD4^+$ helper T cells ($CD4^+FOXp3^-$) and regulatory T cells (T_{regs}; $CD4^+FOXp3^+$) displayed a similar trend in the TME (Figure 5-19B,Ei,Eii). Additionally, the numbers of intratumoral dendritic cells (DCs; $CD11c^+MHCII^+$), which are essential to provide a secondary co-stimulus for T-cell activation[11], are drastically depleted within these tumors (Figure 5-19C,Gi). These findings suggest that while GEM displays positive immunological effects systemically, its impact on anti-tumorigenic immune cells may be hindering its ability to elicit a robust immune response against TNBC.

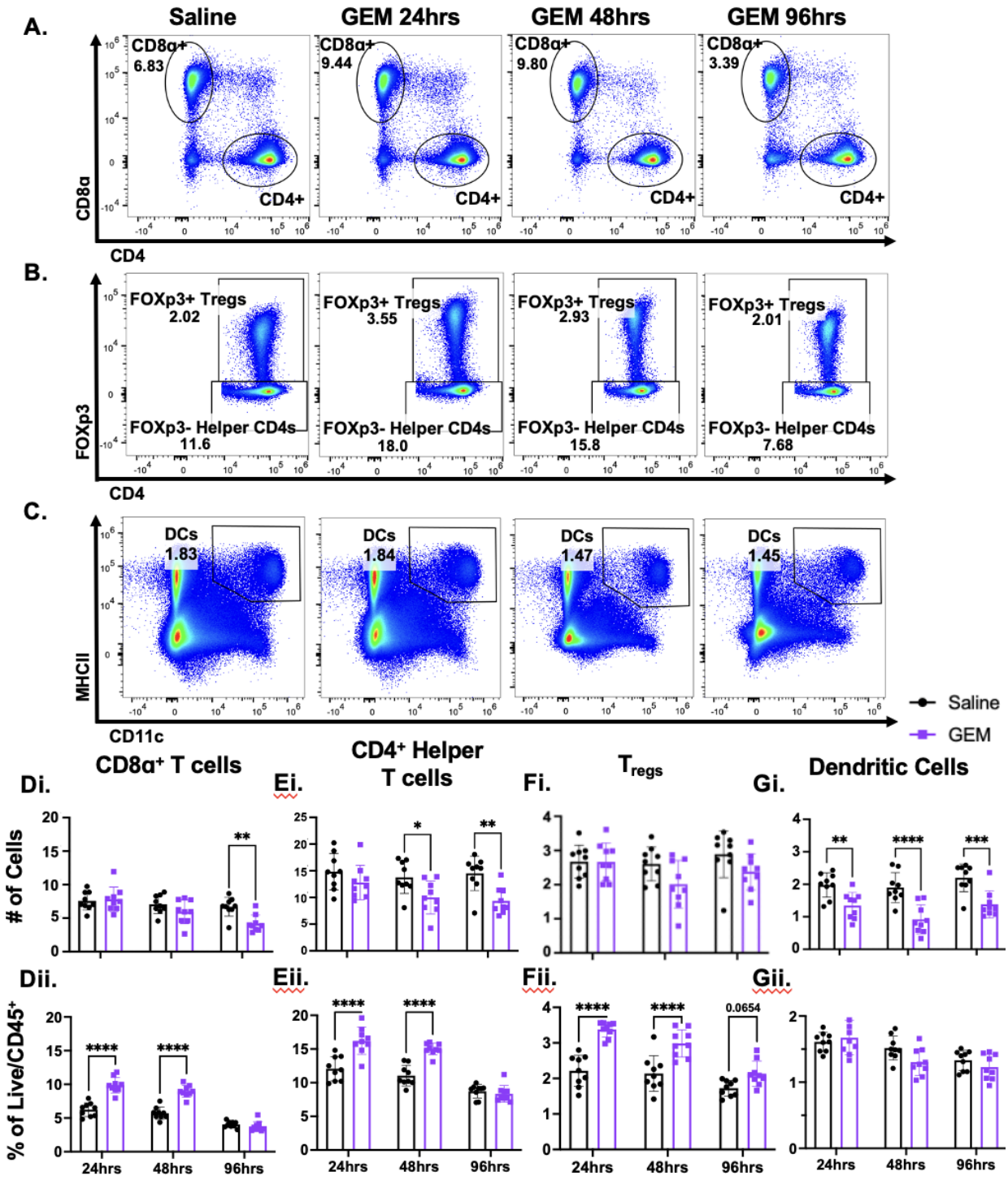

Figure 5-18. The systemic effects of GEM on T cells and dendritic cells are less pronounced than what is observed in the TME. 350k 4T1 parental cells were inoculated in the right flanks of BALB/c mice. Mice were injected with GEM (1.2mg) or saline I.P. on day 14 post inoculation. Spleens were excised 24, 48 and 96hrs post injection **A.** Representative flow plots of $CD8\alpha^+$ T cells ($Ly6G^-$Not DCs $CD3^+CD8\alpha^+$) post GEM injection. **B.** Representative flow plots of $CD4^+$ helper T cells ($Ly6G^-$Not DCs $CD3^+CD4^+FOXp3^-$) and regulatory T cells (T_{regs}; $Ly6G^-$Not DCs $CD3^+CD4^+FOXp3^+$). **C.** Representative flow plots showing changes in dendritic cells ($Ly6G^-CD11c^+MHCII^+$) post GEM administration. All frequencies shown are of the Live/$CD45^+$ population. **D.** Changes in $CD8\alpha^+$ T cell number on the order of 10^6 (**Di**) and proportion (**Dii**). **E.** Changes in $CD4^+$ helper T cell number on the order of 10^6 (**Ei**) and proportion (**Eii**). **F.** Changes in T_{reg} number on the order of 10^6 (**Fi**) and proportion (**Fii**). **G.** Changes in dendritic cell number on the order of 10^6 (**Gi**) and proportion (**Gii**).). (n=9) (2way ANOVA with multiple comparisons: ∗ P<0.05, ∗∗ P<0.01, ∗∗∗ P<0.001, ∗∗∗∗ P<0.0001; ROUT Outliers analysis with Q=0.1%). All points represent mean ± SD.

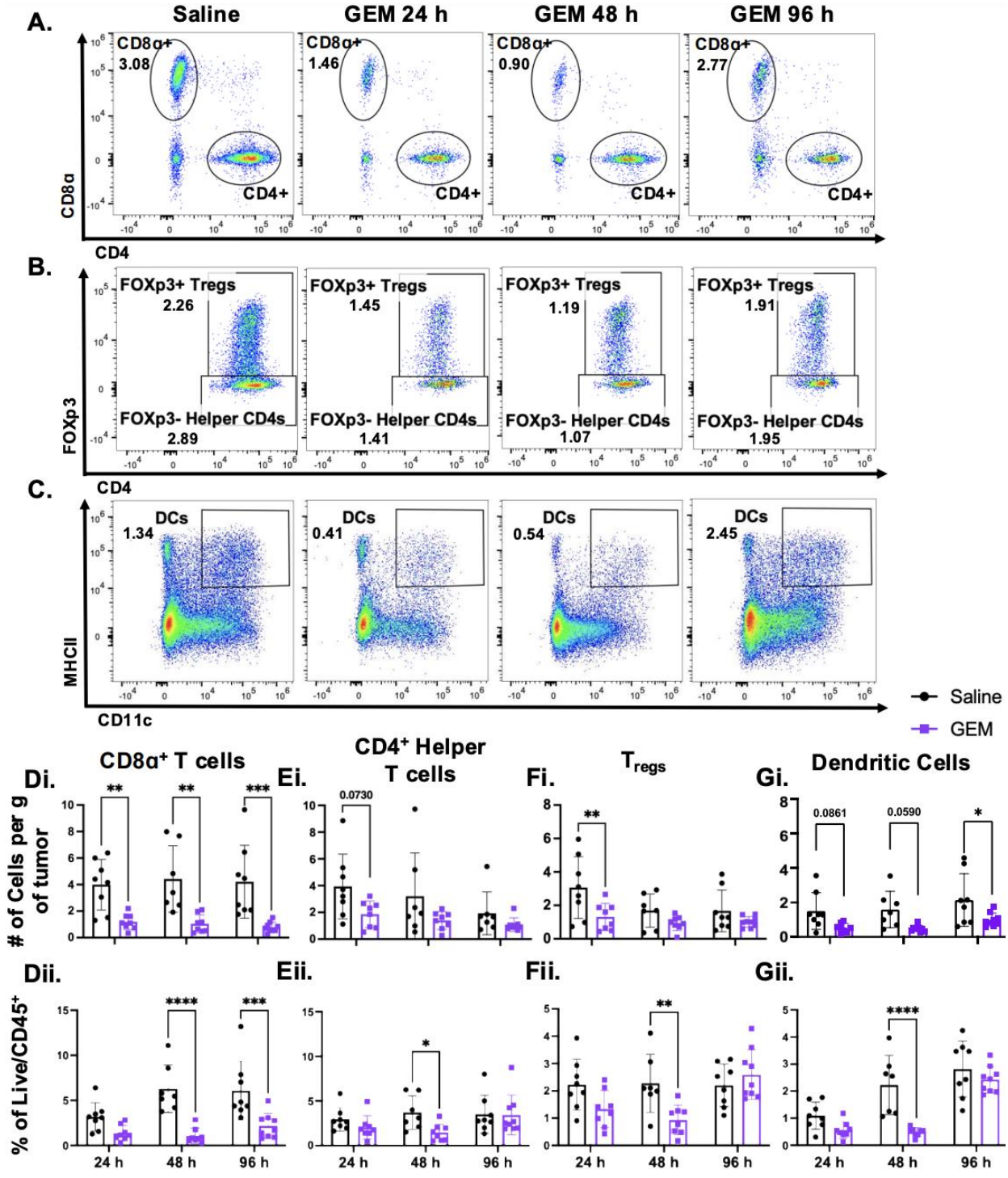

Figure 5-19. GEM significantly lowers the abundance of tumor infiltrating lymphocytes (TILs) and dendritic cells (DCs) in the TNBC TME. 350k 4T1 parental cells were inoculated in the right flanks of BALB/c mice. Mice were injected with GEM (1.2mg) or saline I.P. on day 14 post inoculation. Tumors were excised 24, 48 and 96hrs post injection **A.** Representative flow plots of $CD8\alpha^+$ T cells ($Ly6G^-$Not DCs $CD3^+CD8\alpha^+$) post GEM injection. **B.** Representative flow plots of $CD4^+$ helper T cells ($Ly6G^-$Not DCs $CD3^+CD4^+FOXp3^-$) and regulatory T cells (T_{regs}; $Ly6G^-$Not DCs $CD3^+CD4^+FOXp3^+$). **C.** Representative flow plots showing changes in dendritic cells ($Ly6G^-CD11c^+$ $MHCII^+$) post GEM administration. All frequencies shown are of the Live/$CD45^+$ population. **D.** Changes in $CD8\alpha^+$ T cell number on the order of 10^4 (**Di**) and proportion (**Dii**). **E.** Changes in $CD4^+$ helper T cell number on the order of 10^4 (**Ei**) and proportion (**Eii**). **F.** Changes in T_{reg} number on the order of 10^4 (**Fi**) and proportion (**Fii**). **G.** Changes in dendritic cell number on the order of 10^4 (**Gi**) and proportion (**Gii**). (n=9) (2way ANOVA with multiple comparisons: ∗ P<0.05, ∗∗ P<0.01, ∗∗∗ P<0.001, ∗∗∗∗ P<0.0001; ROUT Outliers analysis with Q=0.1%). All points represent mean ± SD.

3. GEM treatment acutely upregulated genes associated with immune pathways in TNBC tumors

Given that we observed distinct ablative effects of GEM on immune cells present in the TME, we chose to focus on the TNBC tumors themselves and examined what transcriptional changes are occurring in these tumors as a consequence of GEM treatment. Bulk RNA-seq analysis of 4T1 tumors showed that GEM induces the differential expression of genes associated with immune activation 24 h after administration (Figure 5-20A). At this timepoint, Gene Ontology (GO) and Gene Set Enrichment Analysis (GSEA) indicated a significant upregulation of the interferon-gamma (IFN-γ response pathway (Figure 5-20C,E, respectively), which is a hallmark of a type 1 immune response[154]. The strong upregulation of this and other immune pathways such as IFN-α and TNF-α suggests that although GEM is negatively impacting anti-tumoral immune cell populations in the TME, perhaps the cells that remain are being activated. Both the TNF-α and inflammatory response pathways remained upregulated 7 days after GEM injection (Figure 5-20B,D), indicating that this chemotherapy has prolonged transcriptional effects in these tumors.

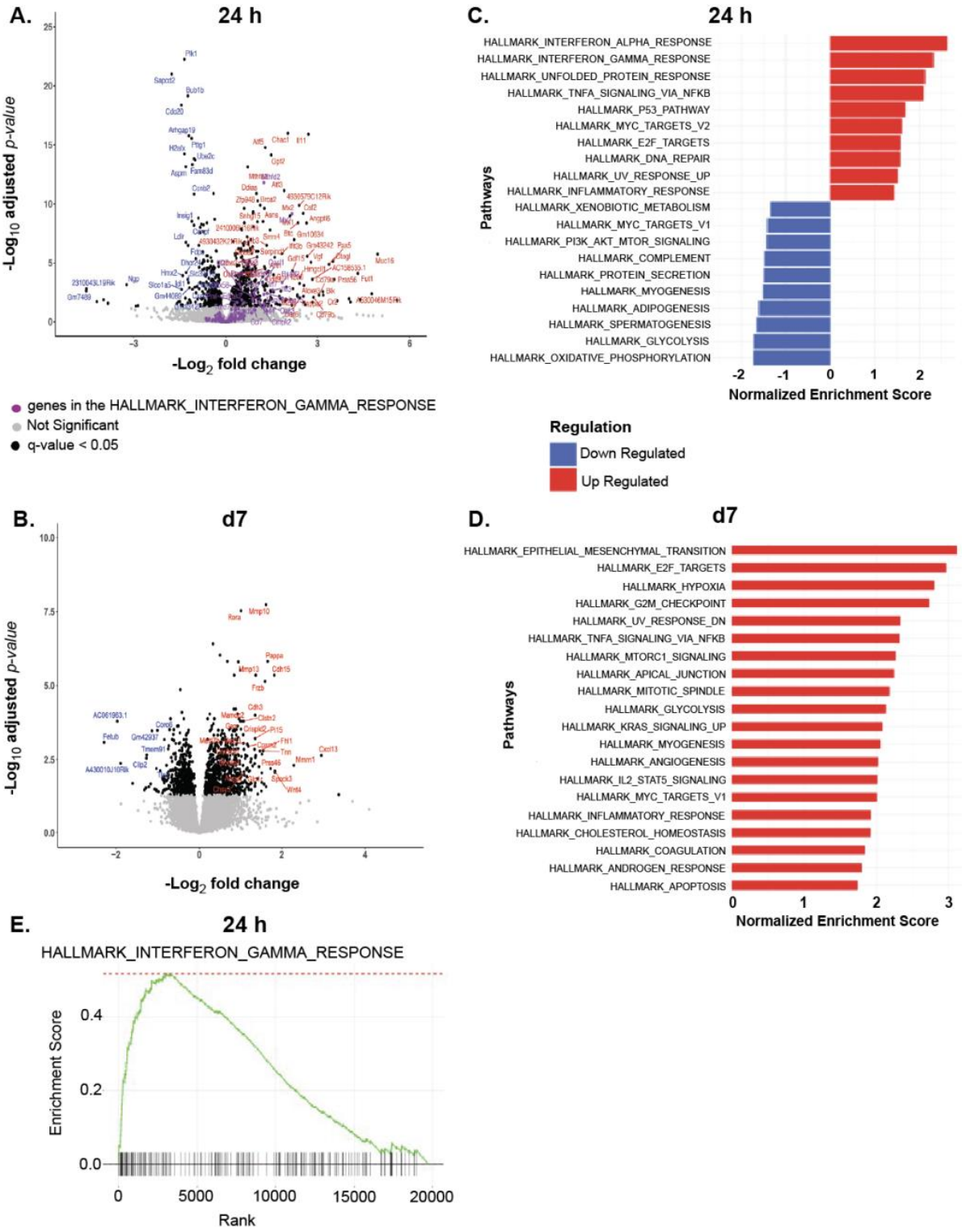

Figure 5-20. GEM treatment acutely upregulates genes associated with immune pathways in triple negative breast cancer (TNBC) tumors. Bulk RNA-seq was performed on 4T1 tumors 24 h and 7 days post systemic (I.P.) injection of GEM (1.2mg) or saline vehicle control. **A & B.** Volcano plots of differentially expressed genes in 4T1 tumors from GEM treated and saline treated mice 24 h (**A**) and 7 days (**B**) post injection. **C & D**. Gene ontology analysis showing normalized enrichment scores for the top 20 hallmark pathways modulated in the GEM cohort compared to the control saline cohort 24 h (**C**) and 7 days (**D**) post injection. **E.** Gene seat enrichment analysis for the "INTERFERON GAMMA RESPONSE" pathway upregulated 24 h after GEM administration.

4. Production of IFN-γ, which is predominately secreted by granulocytic cells in the TME, was altered by GEM

Because changes at the gene transcriptional level do not always correlate with changes at the protein level, we next determined whether the presence of IFN-γ is altered in the 4T1 TME as a result of GEM treatment. By blocking cytokine secretion in vivo with brefeldin A, we were able to quantify changes in IFN-γ levels at various timepoints following the chemotherapy via flow cytometry (Figure 5-21A). Although there was no difference in the number of total live immune cells in the TME that were producing IFN-γ in the GEM-treated cohort compared to the control mice, there was an acute significant increase in the proportion of live/CD45$^+$ cells that were IFN-γ$^+$ (Figure 5-21B,C, respectively). Additionally, we enumerated the amount of IFN-γ being secreted on a per cell basis by analyzing the Geometric Mean Fluorescence (GMF) of IFN-γ on live/CD45$^+$ IFN-γ$^+$ cells, finding that at 96 h, there was a significant increase in the amount of IFN-γ being produced by these cells isolated from tumors exposed to GEM (Figure 5-21D).

When looking only at the total live immune cells staining for IFN-γ, we noticed a distinct positive population of cells, so we next determined which cell subset in the TME is responsible for producing IFN-γ. CD8α$^+$ cytotoxic[155] and Th1 CD4$^+$ T-lymphocytes are known to be a main source of IFN-γ[156]; however, less than 1.5% and less than 0.2% of IFN-γ$^+$ cells were CD8α$^+$ T cells or CD4$^+$ helper T cells, respectively (Figure 5-21Ei,Fi). While there were no changes in the proportion of CD8α$^+$ T cells that were IFN-γ$^+$ (Figure 5-21Eii), there was an increase in the proportion of CD4$^+$FOXp3$^-$ T cells that expressed IFN-γ 24 h after systemic GEM administration (Figure 5-21ii). Only in the CD8α$^+$ T cell population was there an increase in the GMF of IFN-γ at the 96 h timepoint (Figure 5-21Eiii). Surprisingly, the majority (>95%) of IFN-γ$^+$ cells were granulocytes (Ly6G$^+$CD11b$^+$; Figure 5-21Gi). In both murine and human settings, granulocytic

cells have been shown to have the capacity to secrete IFN-γ[157–159], and at the acute 24 h timepoint, GEM treatment increased the proportion of IFN-γ$^+$ cells that were granulocytes and the proportion of granulocytes that express IFN-γ (Figure 5-21Gi,Gii, respectively). Similarly, the amount of IFN-γ being secreted on a per cell basis was significantly increased in IFN-γ$^+$ granulocytes of the GEM cohort 96h following injection (Figure 5-21Giii). We compared these findings in the TME with the effects on GEM on immune cells in the periphery, and we found that GEM significantly decreased both the number and proportion of live/CD45$^+$ cells that were IFN-γ$^+$, with a trending increase in the GMF of IFN-γ (Figure 5-22A–D). In the periphery, granulocytes also make up the majority of IFN-γ$^+$ cells, so alterations in live/CD45$^+$ IFN-γ$^+$ cell numbers are likely the result of the myeloablative nature of GEM previously shown in Figure S2 (Figure 5-22Ei). While changes in IFN-γ GMF were only seen at the 96 h timepoint in the TME, IFN-γ$^+$ granulocytes in the spleens of GEM-treated tumor-bearing mice displayed elevated IFN-γ GMFs at all three timepoints (Figure 5-22Eiii). Altogether, these findings indicate that systemic treatment with GEM results in changes in the secretion and overall presence of the highly immunomodulatory cytokine, IFN-γ.

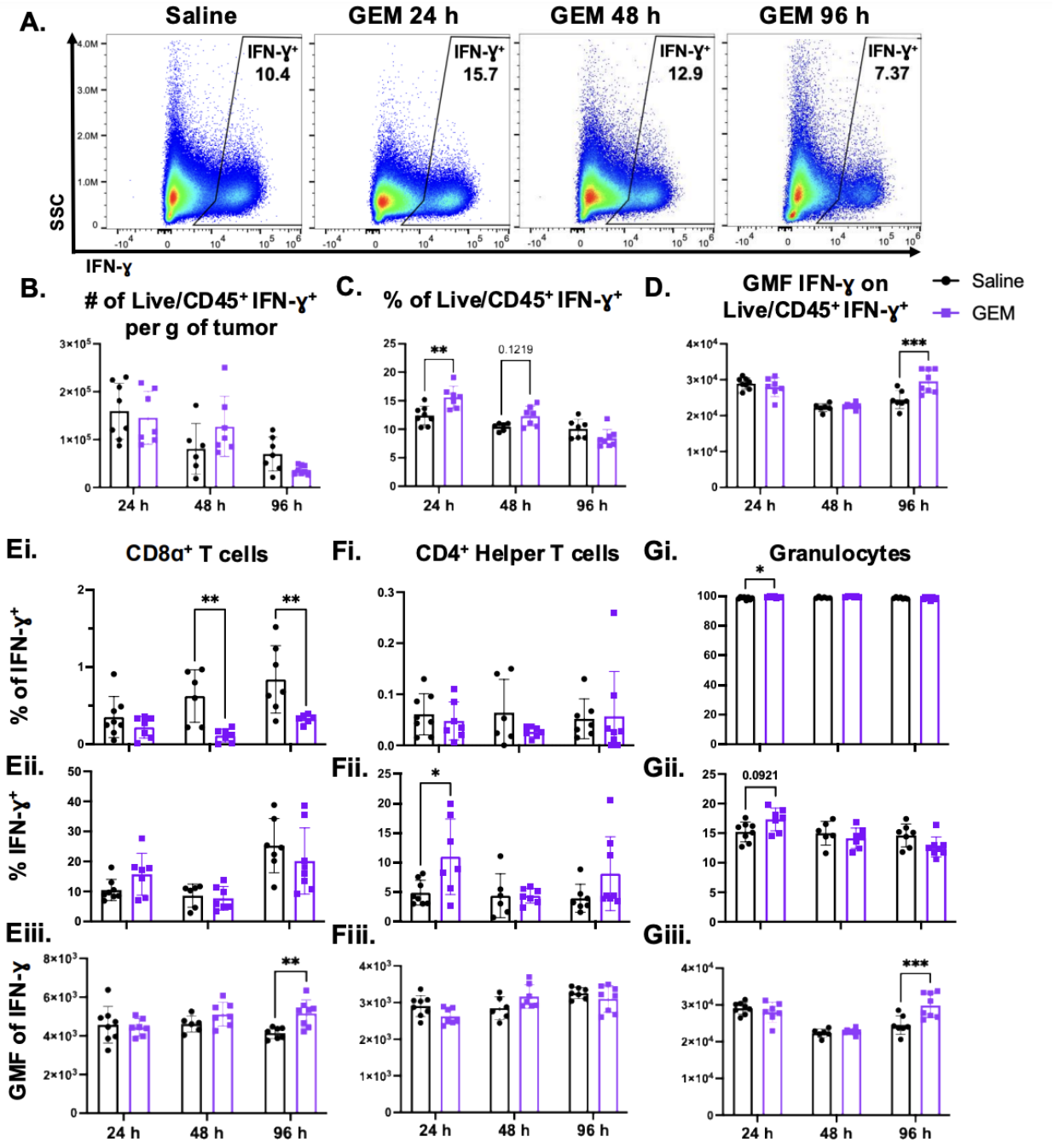

Figure 5-21. Production of IFN-γ, which is predominately secreted by granulocytic cells in the TME, is altered by GEM. 350k 4T1 parental cells were inoculated in the right flanks of BALB/c mice. Mice were injected with GEM (1.2mg) or saline I.P. on day 14 post inoculation. Tumors were excised 24, 48 and 96hrs post injection **A.** Representative flow plots showing changes in the Live/CD45$^+$ IFN-γ$^+$ population following GEM administration. All frequencies shown are of the parent gate. **B.** Change in Live/CD45$^+$ IFN-γ$^+$ cell number. **C.** Change in the proportion of Live/CD45$^+$ cells that are IFN-γ$^+$. **D.** Change in Geometric Mean Fluorescence Intensity (GMF) of IFN-γ on Live/CD45$^+$ IFN-γ$^+$ cells. E. Changes in the proportion of IFN-γ$^+$ cells that are CD8α$^+$ T cells (**Ei**), the proportion of CD8α$^+$ T cells that are IFN-γ$^+$ (**Eii**), and the GMF of IFN-γ on IFN-γ$^+$ CD8α$^+$ T cells (**Eiii**). **F.** Changes in the proportion of IFN-γ$^+$ cells that are CD4$^+$ helper T cells (**Fi**), the proportion of CD4$^+$ helper T cells that are IFN-γ$^+$ (**Fii**), and the GMF of IFN-γ on IFN-γ$^+$ CD4$^+$ helper T cells (**Fiii**). **G.** Changes in the proportion of IFN-γ$^+$ cells that are granulocytes (**Gi**), the proportion of granulocytes that are IFN-γ$^+$ (**Gii**), and the GMF of IFN-γ on IFN-γ$^+$ granulocytes (**Giii**). (n=8) (2way ANOVA with multiple comparisons: ∗ P<0.05, ∗∗ P<0.01, ∗∗∗ P<0.001, ∗∗∗∗ P<0.0001; ROUT Outliers analysis with Q=0.1%). All points represent mean ± SD.

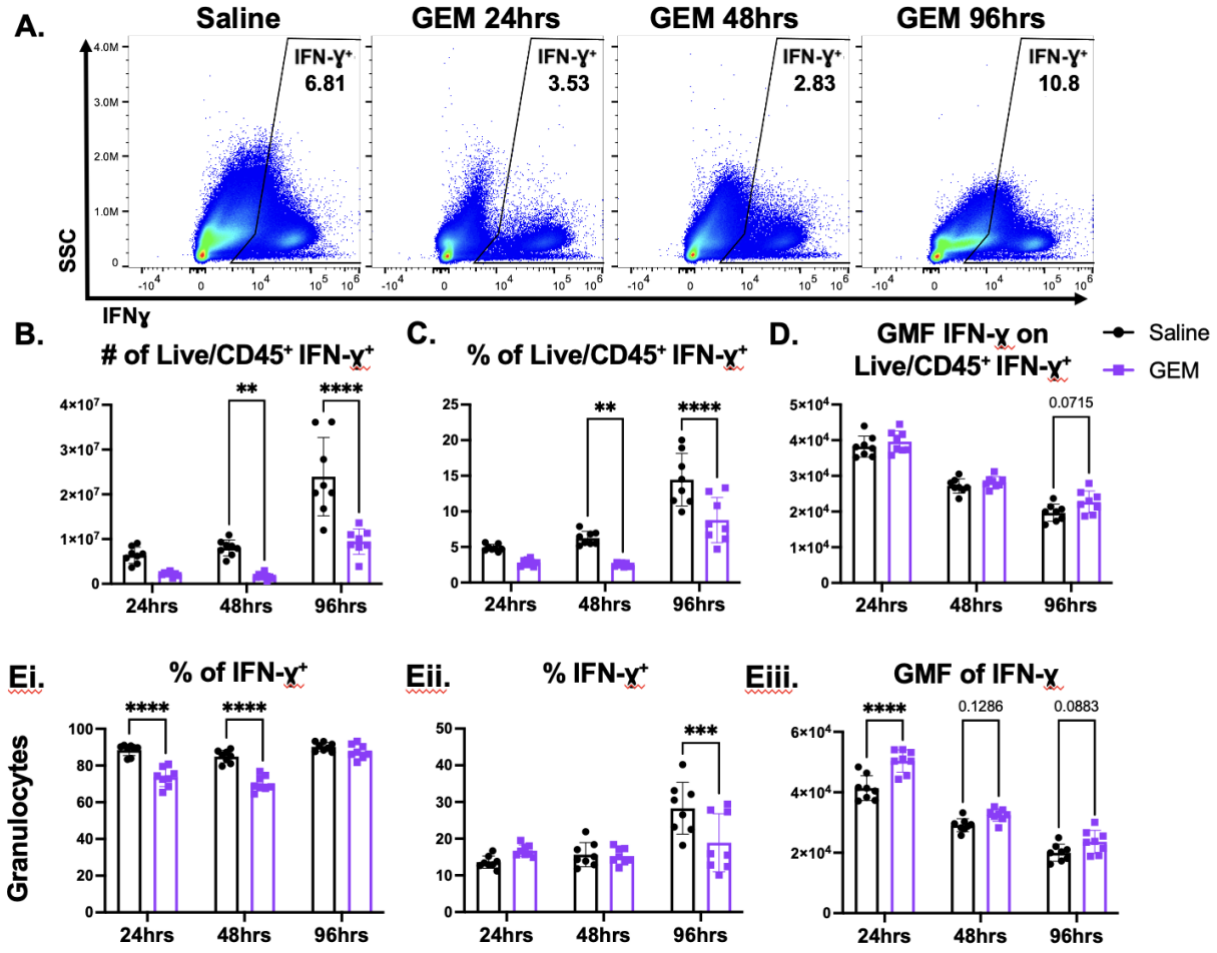

Figure 5-22. GEM-induced effects on IFN-γ production in spleens of TNBC tumor-bearing mice. 350k 4T1 parental cells were inoculated in the right flanks of BALB/c mice. Mice were injected with GEM (1.2mg) or saline I.P. on day 14 post inoculation. Spleens were excised 24, 48 and 96hrs post injection **A.** Representative flow plots showing changes in the Live/CD45$^+$ IFN-γ$^+$ population following GEM administration. All frequencies shown are of the parent gate. **B.** Change in Live/CD45$^+$ IFN-γ$^+$ cell number. **C.** Change in the proportion of Live/CD45$^+$ cells that are IFN-γ$^+$. **D.** Change in Geometric Mean Fluorescence Intensity (GMF) of IFN-γ on Live/CD45$^+$ IFN-γ$^+$ cells. **E.** Changes in the proportion of IFN-γ$^+$ cells that are granulocytes (**Ei**), the proportion of granulocytes that are IFN-γ$^+$ (**Eii**), and the GMF of IFN-γ on IFN-γ$^+$ granulocytes (**Eiii**). (n=8) (2way ANOVA with multiple comparisons: ∗ P<0.05, ∗∗ P<0.01, ∗∗∗ P<0.001, ∗∗∗∗ P<0.0001; ROUT Outliers analysis with Q=0.1%). All points represent mean ± SD.

5. GEM-mediated tumor growth control was not dependent on IFN-γ

We observed that GEM induces alterations to IFN-γ response pathways transcriptionally as well as on the protein level in the TME of TNBC tumors. Next, we examined whether GEM-mediated 4T1 growth inhibition is dependent on IFN-γ. To address this, we co-administered 200

µg of either anti-IFN-γ (BioXCell XMG1.2) or the IgG isotype control with the 3 weekly GEM injections, and tumors were measured daily to assess changes in outgrowth (Figure 5-23A). We found that neutralizing IFN-γ had no impact on GEM-mediated control of 4T1 outgrowth (Figure 5-23B,C), suggesting that the anti-tumoral effects of GEM are independent of IFN-γ.

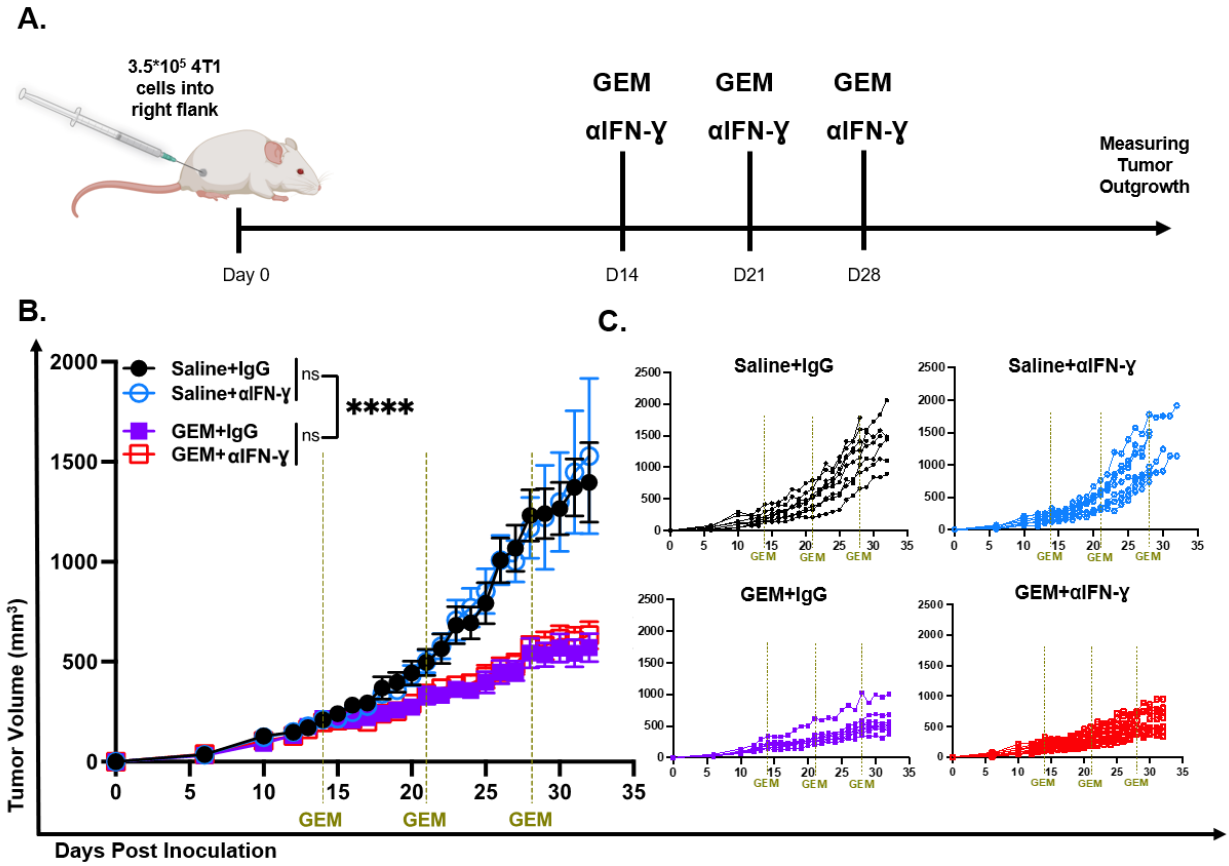

Figure 5-23. GEM-mediated tumor growth control is not dependent on IFN-ɣ. A. Overview of experimental design to evaluate the efficacy of GEM on constraining TNBC primary tumor outgrowth when neutralizing IFN-ɣ. **B.** Average tumor growth curves for mice treated with GEM (1.2mg) or saline I.P. on days 14, 21 and 28 post inoculation + anti-IFN-ɣ (XMG1.2; 200 µg) or + IgG isotype control (200 µg). (Mixed-effects model: **** P<0.0001). All points represent mean ± SEM. **C.** Individual tumor growth curves of GEM and saline + anti-IFN-ɣ (XMG1.2) or + IgG isotype control treated mice.

6. GEM treatment altered arginase 1 expression by myeloid cells in TNBC tumors

We have shown that GEM does not have a significant impact on the presence of most myeloid cell subsets in the TME, so we investigated whether the suppressive function of these cells is altered by GEM. To achieve this, we quantified changes in Arginase 1 (Arg1) expression. Arg1, a hydrolase enzyme involved in the breakdown of L-arginine, has been shown to accumulate in human and murine breast cancer, and its presence is associated with poor prognosis and an enhanced immunosuppressive environment[22]. To first understand the relatedness of IFN-γ and Arg1 expressing myeloid cells, we performed t-distributed stochastic neighbor embedding (tSNE) dimensionality reduction analysis of flow cytometry data derived from the $Ly6G^+CD11b^+$ population (Figure 5-24A). Multigraph color mapping of the tSNE plot displays clear separation between the IFN-γ^+ cells and the $Arg1^+$ cells (Figure 5-24B,C). We concluded that Arg1-expressing cells are discrete from those that express IFN-γ.

We broadly analyzed the expression of Arg1 by total live immune cells in these tumors after treatment with GEM (Figure 5-24D). We observed minimal changes in the number, percentage, and the amount of Arg1 being expressed on a per cell basis within the Live/$CD45^+$ population (Figure 5-24E–G). Because Arg1 is primarily expressed by cells of myeloid lineage in the TME, such as MDSCs and tumor-associated macrophages, we then focused on Arg1 positivity in individual $CD11b^+$ cell subsets. We altered the description of the granulocytic and monocytic cells in the TME to be G-MDSCs ($Ly6G^+CD11b^+Arg1^+$) and M-MDSCs ($CD11b^+$ $Ly6G^-F4/80^-$ $Ly6C^+Arg1^+$), respectively, because of their pathognomonic expression of immunosuppressive Arg1. G-MDSCs compose the largest subset of $Arg1^+$ cells in the TME (70–95%), followed by inflammatory monocytes (5–25%), macrophages (0.53%), and M-MDSCs (0.3-1.5%) (Figure 5-24H–Kii). The trends within the $Arg1^+$ subset mimic the effects of GEM on these immune cell subsets in the TME displayed in Figure 5-16. GEM did not reduce the number or percentage of

G-MDSCs that were Arg1$^+$, however, it acutely reduced the presence of Arg1$^+$ M-MDSCs and macrophages at 24 h (Figure 5-24Hi–Ji and Hiii–Jiii, respectively). This attenuation was not maintained, as the proportion of MDSCs that were Arg1$^+$ returned to baseline by 96 h, while the proportions of Arg1$^+$ macrophages and inflammatory monocytes from GEM-treated tumors increased at the later timepoints (Figure 5-24Jiii, Kiii, respectively). Interestingly, while G-MDSCs comprised the largest subset of Arg1$^+$ cells, they had the lowest GMF of Arg1, indicating that these express the lowest levels of Arg1 on a per cell basis when compared to the other three myeloid subsets (Figure 5-24H-Kiv). Within the M-MDSC and inflammatory monocyte populations, the GMF of Arg1 significantly increased shortly after GEM administration; however, these levels returned to control baseline 96 h after treatment (Figure 5-24Iiv, 6Kiv). The opposite trend was observed within the macrophage compartment (Figure 5-24Jiv). In all, these findings suggest that administering GEM as a therapy for TNBC results in modest changes in the expression of the immunosuppressive enzyme Arg1 in the TME.

Figure 5-24. GEM treatment alters Arginase 1 (Arg1) expression by myeloid cells in TNBC tumors. 350k 4T1 parental cells were inoculated in the right flanks of BALB/c mice. Mice were injected with GEM (1.2mg) or saline I.P. on day 14 post inoculation. Tumors were excised 24, 48 and 96hrs post injection **A.** tSNE dimensionality reduction on granulocytic (Ly6G$^+$CD11b$^+$) cells in the TME. **B.** Multigraph color mapping of IFN-ɣ expression on granulocytic cells in the TME. **C.** Multigraph color mapping of Arg1 expression on granulocytic cells in the TME. **D.** Representative flow plots showing changes in the Live/CD45$^+$ Arg1$^+$ population following GEM administration. All frequencies shown are of the parent gate. **E.** Change in Live/CD45$^+$ Arg1$^+$ cell number. **F.** Change in the proportion of Live/CD45$^+$ cells that are Arg1$^+$. **G.** Change in Geometric Mean Fluorescence Intensity (GMF) of Arg1 on Live/CD45$^+$ Arg1$^+$ cells. **H.** Changes in the number of Arg1$^+$ G-MDSCs (Ly6G$^+$CD11b$^+$) (**Hi**), the proportion of Arg1$^+$ cells that are G-MDSCs (**Hii**), the proportion of G-MDSCs that are Arg1$^+$ (**Hiii**), and the GMF of Arg1 on Arg1$^+$ G-MDSCs (**Hiv**). **I.** Changes in the number of Arg1$^+$ M-MDSCs (CD11b$^+$Ly6G$^-$F4/80$^-$Ly6C$^+$) (**Ii**), the proportion of Arg1$^+$ cells that are M-MDSCs (**Iii**), the proportion of M-MDSCs that are Arg1$^+$ (Iiii), and the GMF of Arg1 on Arg1$^+$ M-MDSCs (**Iiv**). **J.** Changes in the number of Arg1$^+$ macrophages (CD11b$^+$Ly6G$^-$F4/80$^+$Ly6C$^-$) (**Ji**), the proportion of Arg1$^+$ cells that are macrophages (**Jii**), the proportion of macrophages that are Arg1$^+$ (**Jiii**), and the GMF of Arg1 on Arg1$^+$ macrophages (**Jiv**). **K.** Changes in the number of Arg1$^+$ inflammatory monocytes (CD11b$^+$Ly6G$^-$F4/80$^+$Ly6C^{hi}) (**Ki**), the proportion of Arg1$^+$ cells that are inflammatory monocytes (**Kii**), the proportion of inflammatory monocytes that are Arg1$^+$ (**Kiii**), and the GMF of Arg1 on Arg1$^+$ inflammatory monocytes (**Kiv**). (n=8) (2way ANOVA with multiple comparisons: ∗ P<0.05, ∗∗ P<0.01, ∗∗∗ P<0.001, ∗∗∗∗ P<0.0001; ROUT Outliers analysis with Q=0.1%). All points represent mean ± SD.

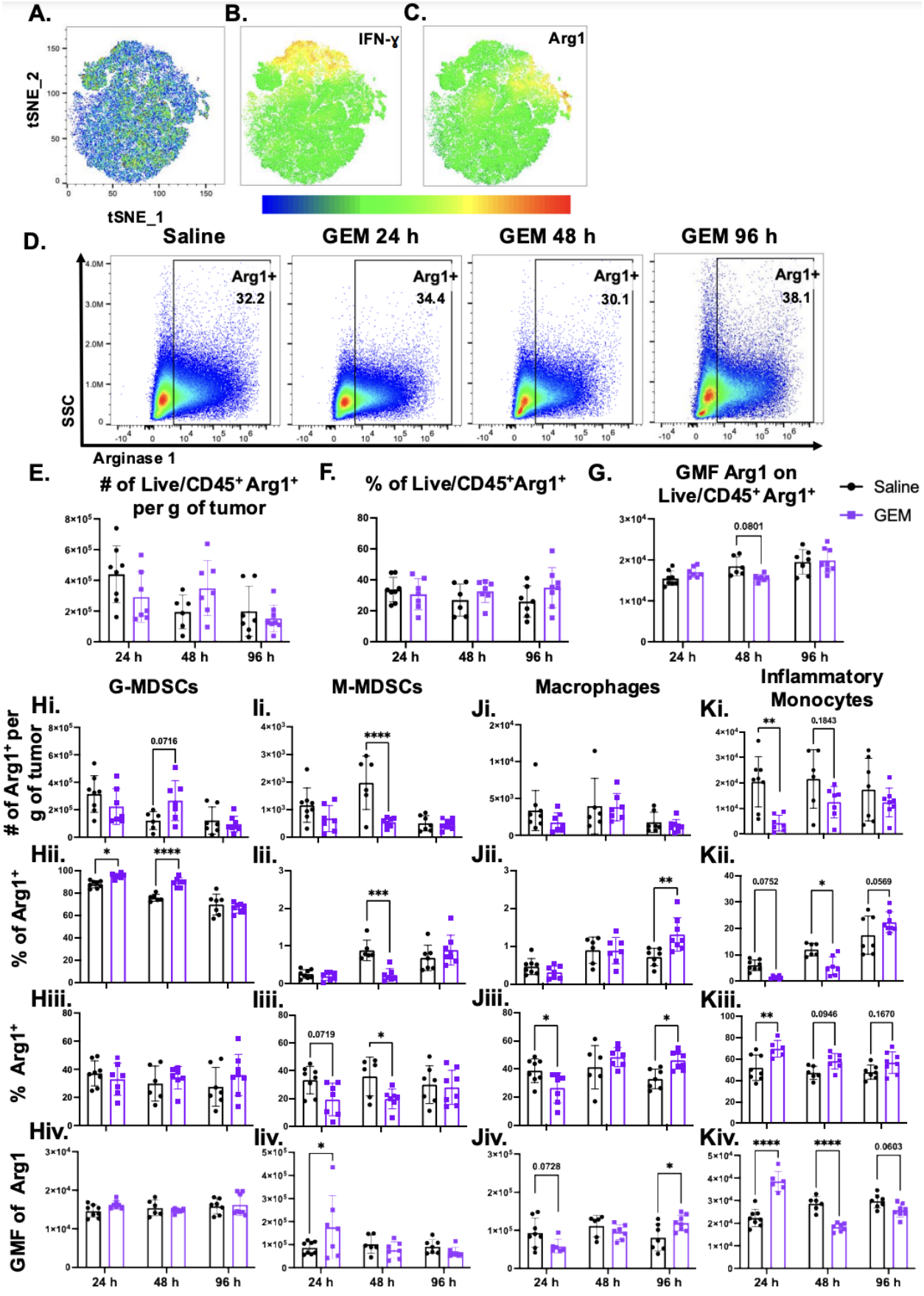
A.
B.
C.
IFN-γ
Arg1
tSNE_2
tSNE_1
D.
Saline
GEM 24 h
GEM 48 h
GEM 96 h
Arg1+ 32.2
Arg1+ 34.4
Arg1+ 30.1
Arg1+ 38.1
SSC
Arginase 1
E.
# of Live/CD45+ Arg1+ per g of tumor
F.
% of Live/CD45+Arg1+
G.
GMF Arg1 on Live/CD45+ Arg1+
Saline
GEM
24 h
48 h
96 h
G-MDSCs
M-MDSCs
Macrophages
Inflammatory Monocytes
Hi.
Ii.
Ji.
Ki.
Hii.
Iii.
Jii.
Kii.
Hiii.
Iiii.
Jiii.
Kiii.
Hiv.
Iiv.
Jiv.
Kiv.
# of Arg1+ per g of tumor
% of Arg1+
% Arg1+
GMF of Arg1
0.0716
****
0.1843
0.0801
0.0752
0.0569
0.0719
0.0946
0.1670
0.0728
0.0603

DISCUSSION

Regarding MDSC depletion, while the mAbs proved challenging to sustain depletion and avoid toxicity in the 4T1 model, future studies could be aimed at inhibiting MDSC and TAM generation in the TME through genetic deletion or inhibition of cyclooxygenase 2 (COX2) – an immunosuppressive enzyme that promotes MDSC and TAM differentiation through the production of prostaglandins such as PGE2 & can induce the expression of Arg1 in tumor-associated myeloid cells[160–162]. Alternatively, instead of trying to deplete or reduce these myeloid populations, future studies could focus on reprogramming and repolarizing the existing cells to avoid toxicity most likely due to massive cell death, while abrogating the suppressive function of the cells residing in the TME. This could be achieved by employing toll-like receptor (TLR) agonism, which mimics endogenous responses to pathogen or danger associated molecular patterns, to skew myeloid differentiation and functionality towards less suppressed, more anti-tumorigenic state[163–167].

Additionally, we found that altering the ablation fraction of a TFUS treated tumor, which changes the amount of the tumor tissue that is destroyed, induces diverging transcriptional and differential gene expression alterations in the treated tumors. A higher degree/area of ablation (1mm-TFUS) resulted in sustained transcriptional changes in the treated tumors a week post therapy. While additional studies would need to be done to validate the transcriptomic findings proteomically, this data is critical when thinking about patient responsive to TFUS. As many clinical trials have been conducted using TFUS as a therapy for BrCa[168], when comparing outcomes, we may need to consider how much of the tumor is ablated, what effects does this ablation have on both the local and systemic immune system, and would it be more beneficial to ablate more or less of the tumor tissue? While we were unable to replicate the previously

published studies using the FUSSY single element transducer system (described in chapter two), UVA has since acquired another extracranial FUS system (referred to as the PG4). Unlike the FUSSY system which only has one treatment transducer, the PG4 system has four treatment transducers that converge into a smaller focal region. This allows for more precise targeting and ablation, limiting heat deposition. Others in our labs have since used the PG4 system to treat higher ablation fractions than the ~5% obtained on FUSSY with 3mm-spaced TFUS, and they have observed therapeutic success consistent with previous studies accompanied by significantly less toxicity than were apparent in the studies described in this Chapter. In the future, the extent of TFUS+GEM induced immunogenicity as well as the potential tuning of an immune response based on TFUS ablation fraction should be further studied using the PG4 system.

Given the prognostic implications of MDSC and TIL presence in the tumors of TNBC patients, the immunosuppressive effects of MDSCs, and the capacity of a subset of TNBC patients to respond to anti-PD-1 treatment, we examined whether the previously reported systemic immunological effects of the clinically relevant chemotherapy, GEM, are recapitulated in the TME of TNBC in a preclinical model. This information is important when considering combination therapies that are likely to improve anti-tumor immunity in TNBC patients with aggressive disease and would thus provide a rationale for the efficacy of GEM in the context of ablative focused ultrasound. Prior research suggests that GEM acts as a myeloablative therapy, depleting suppressive MDSC populations systemically with limited effects on cytotoxic lymphocytes[144–146]. Our findings are consistent with the previous study where we examined peripheral $CD45^+$ immune cell populations in spleens and blood of 4T1 tumor-bearing mice treated with GEM or vehicle control (Figures 5-13 & 5-14). However, in contrast to the effects on circulating immune cells, we found that GEM treatment does not have myeloablative effects

in the TME; at no assessed timepoint did GEM decrease the granulocyte number in the TME. Rather, the proportion of granulocytes increased in response to treatment. Similar results were seen with the monocyte and macrophage populations (Figure 5-16).

We further considered the impact of GEM on cellular components that contribute to T-cell responses against tumors. Inconsistent with our hypothesis that GEM would support anti-tumor immunity, we found that contrary to the minimal effects of GEM on T-lymphocyte numbers in circulation after a single dose or multiple doses[84,145,146], there were sustained significant reductions in cytotoxic $CD8\alpha^+$ and helper $CD4^+$ T cells, as well as a reduction in DCs in the TME following GEM treatment (Figure 5-19). While immune cells in circulation can feed and supply immune cells to the TME, it is possible that we did not observe the T cells and DCs repopulate over the time course studied because cell extravasation requires proper transmigratory signals such as proinflammatory cytokines, chemoattractant gradients, and adhesive integrins present so that leukocytes can migrate from the bloodstream into the TME[169]. This process can be inhibited by the presence of pro-tumorigenic cytokines and immunosuppressive cells such as MDSCs[170,171]. Nonetheless, although GEM displays positive immunological effects on peripheral immune cell subsets—such as reducing MDSC burden—the diminution of TILs in the TME provides insight as to why GEM as a monotherapy may be unable to induce a robust adaptive immune response and regress TNBC growth (Figure 5-15), and it suggests that combinatorial regimens utilizing GEM and anti-PD-1 may not be efficacious due to the reduction in TIL presence.

In murine species, GEM has a short half-life of ≈3 h[153], raising the possibility that the ineffectiveness of GEM against MDSCs in the TME could be due to insufficient accumulation in this environment. While we found that the inflammatory monocyte subset of $F4/80^+Ly6C^{hi}$ cells

was significantly reduced acutely following GEM administration (Figure 5-16), it is possible that sufficient accumulation of the active metabolite of GEM differs amongst immune cell types. We investigated whether GEM was preferentially affecting F4/80^{+}Ly6C^{hi} cells due to their proliferative status, as GEM will non-specifically incorporate into the DNA of any replicating cell and induce cell cycle arrest. Surprisingly, we found that all four myeloid populations, including MDSCs, were proliferative in the TME (Figure 5-17). GEM is a prodrug, meaning it is pharmacologically inactive in its administered state. Functional nucleoside transport proteins are required for this drug to permeate a cell's plasma membrane[172]. Once inside a cell, GEM must undergo three distinct phosphorylation events to reach its metabolically active form. During its metabolism, GEM can be inactivated at different metabolic stages by deamination via cytidine deaminase or deoxycytidylate deaminase[133,173] and by dephosphorylation by 5′-nucleotidases[174]. Additionally, GEM and its metabolites can also be effluxed from cells by ATP-binding cassette (ABC) transporters[175]. One of the most prominent causes hindering chemotherapeutic efficacy is multidrug resistance. Other mechanisms include increased DNA repair capacity, upregulated anti-apoptotic proteins[176], and activation of the transcription factor NRF2 to support tumorigenesis during oxidative stress[177–179]. Therefore, differential protein expression of nucleoside transporters, deaminase enzymes, 5′-nucleotidases, DNA repair proteins, cell death factors, ABC transporters, and/or activation of the NRF2 pathway would impact the efficacy of GEM across immune cell types and could explain the selective ablative effects of GEM. Another possibility is that the penetration of GEM may be locoregional in the TME, resulting in preferential depletion of immune cells residing in areas where GEM may be accumulating. Altogether, our data suggest that DNA replication is not the only factor impacting a cell's susceptibility to GEM.

Despite the apparent deleterious effects of GEM on the T cell presence in tumors, bulk RNA-seq of TNBC tumors 24 h and 7 days after GEM treatment revealed upregulation of genes and pathways associated with immune activation, one of which being the IFN-γ response pathway (Figure 5-20). Upon examining IFN-γ production by immune cells in the TME, we discovered that GEM significantly increased the proportion and amount of IFN-γ being secreted by total live immune cells. Interestingly, most of the IFN-γ (>95%) is being produced by granulocytes (Figure 5-21). While T-lymphocytes and natural killer cells are most often the main producers of this cytokine[155,156,180], neutrophils and granulocytic cells in both the murine and human setting have been shown to produce IFN-γ[157–159]. As a potent immunomodulatory cytokine, IFN-γ mediates many tumoricidal mechanisms[181–184]. However, consistent with previous studies, impeding IFN-γ function did not affect primary 4T1 tumor outgrowth[185,186], and neutralizing IFN-γ did not affect GEM's ability to constrain 4T1 tumor outgrowth (Figure 5-23), indicating that the anti-tumoral effects of GEM are not dependent of IFN-γ. These data suggest that the upregulation of IFN-γ is a byproduct of the chemotherapy, by a mechanism yet to be established but possibly related to GEM's modest ability to induce immunogenic cell death[187]. While other immunosuppressive factors may limit the activity of IFN-γ elicited by GEM in a monotherapy setting, this induction of IFN-γ by GEM may contribute to the enhanced immune responses generated when used in combination with thermally ablative focused ultrasound, per our previous study[84].

The presence of Arg1 in human and murine BrCa correlates with poor prognosis and increased immunosuppression. In the context of BrCa, GEM has been shown to enhance Arg1 expression by $Ly6C^{hi}$ myeloid cells in vitro[148]. Supporting Wu et al.'s findings, we observed a sustained increase in the proportion of inflammatory monocytes ($F4/80^{+}Ly6C^{hi}$) that were $Arg1^{+}$

in the GEM treated cohort. Additionally, we found that GEM temporally altered the number of $Arg1^+$ cells and the amount of Arg1 being produced on a per cell basis. Reductions in $Arg1^+$ cell number are observed in M-MDSC and inflammatory monocyte populations, while we found an increase in $Arg1^+$ G-MDSCs 48 h after GEM. Acutely, M-MDSCs and inflammatory monocytes expressed a significant increase in Arg1 GMF, while the macrophage subset had a significant reduction 24 h after GEM administration, followed by a significant increase at 96 h (Figure 5-24). While further work would need to be done to determine whether GEM is enhancing the immunosuppressive nature of myeloid cells in the TME, our findings support that the chemotherapy is playing a role in augmenting Arg1 expression within these $CD11b^+$ cell subsets, suggesting the use of Arg1 inhibitors in combination with GEM.

In conclusion, our data show that treatment of murine TNBC with the clinically employed chemotherapy GEM results in tissue- and temporal-dependent immune ablative effects. While GEM acts as a pan-myeloablative drug in the periphery, it has an isolated impact on $F4/80^+Ly6C^{hi}$ myeloid cells in the TME. Additionally, we found that a single dose of GEM resulted in a sustained reduction of T-lymphocytes in the TME, potentially hinting at an explanation as to why GEM as a monotherapy is not able to induce a strong adaptive immune response capable of regressing TNBC outgrowth. While we interrogated the immunological impact of a single dose of systemic GEM, future studies could consider whether multiple treatments with this chemotherapy mimic the effects we observe or deviate in terms of immune cell perturbations.

Chapter Six: Conclusions & Future Directions

Mode of boiling histotripsy-induced tumor antigen dissemination to the TDLNs

Boiling histotripsy (BH) is a non-invasive and non-ionizing form of mechanically ablative FUS that has displayed promise preclinically as a cancer therapeutic. While BH and other forms of mechanical ablation have been reported to induce anti-tumorigenic immune activation, the immune responses elicited are not durable as tumor growth control is lost over time. Here, we chose to address key gaps in knowledge regarding where BH therapy could intersect with the Cancer-Immunity Cycle, as well as identifying limitations of BH-induced immunity to improve combinatorial treatment regimens and optimize therapeutic efficacy.

Our previous studies have reported that BH treatment results in the dissemination of an acute bolus of tumor antigen to the TDLNs[75], however, it remained unclear how this antigen was making its way to there. Others have shown that the presence of tumor antigen in the lymph nodes is dependent on migratory cDCs – specifically cDC1s[4] – which traffic from the tumor to the TDLNs. To impede CCR7-mediated cDC migration, we utilized an αCCR7 blocking antibody. We found that that when cDC trafficking was inhibited, BH treatment still increased proportions of ZsG positive migratory and LN-resident cDCs. This data in conjunction with our prior findings of BH increasing ZsG presence across multiple subsets of APCs and phagocytic cells[75], and ZsG colocalization to the lymphatic sinuses of the TDLNs 2 h following ablation, supports the notion that antigen dissemination to the TDLNs post BH is independent of CCR7-mediated cDC trafficking. We have acknowledged that the approach used here to hinder cDC trafficking did not completely abrogate migratory cells. While we did try to utilize whole body

CCR7$^{-/-}$ mice, which lack all migratory cDCs[4] , we encountered technical challenges in that the absence of CCR7 results in impaired lymphatic flow[116]. Therefore, we could not distinguish whether reductions in ZsG antigen presence in the TDLNs are the result of impeding cDC migration or due to the inherent defects in lymphatic vasculature in CCR7$^{-/-}$ mice. It is just as likely that we did not observe a bolus of ZsG antigen to the TDLNs post BH in this model due to impeded lymphatic drainage rather than the loss of migratory cDCs. To combat these limitations, we have proposed mixed BM chimera mice reconstituted with equal parts CCR7$^{-/-}$: Zbtb46^{dtr}. By utilizing BM from the Zbtb46^{dtr} mice, we can ensure presence of a complete immune system with CCR7-expressing cDCs during animal development and tumor progression. Then prior to BH treatment, diphtheria toxin will be administered to deplete cDCs derived from Zbtb46^{dtr} BM – thus leaving behind only CCR7 $^{-/-}$cDCs[117].

Alternatively, we have only examined one aspect of this chemotactic axis, the CCR7 receptor, but we have not determined whether BH induces changes to CCL19 and CCL21, the chemokines secreted by stromal and lymphatic endothelial cells to drive cDC migration. Our findings here could be supplemented with ELISA assays performed on TDLNs from Sham or BH treated cohorts to determine whether BH augments expression of either of these cytokines. Based on our previous results we would predict that this is not the case, but it may be an important control to substantiate the claim that cDC migration via CCR7 is not required for tumor antigen dissemination into the TDLNs following mechanical ablation of tumors with BH. When considering the role of BH in the Cancer-Immunity Cycle, this finding suggests that BH can bypass the need for peripheral acquisition of tumor antigen and cDC trafficking.

The effect of BH on tumor-specific CD8^{+} T-cell activation

Prior to our studies, it was unknown whether the liberation of cell-free antigen by BH can bypass the requirement of migratory cDC trafficking for the stimulation of a $CD8^+$ T-cell response against the cancer. Utilizing adoptive cell transfer studies with PMEL TCR transgenics, we were able to assess tumor-specific T-cell activation in response to BH. We found that BH treatment results in increased activation status of PMEL $CD8^+$ T-cells. This was evident by an increase in the co-expression of canonical activation markers CD69 and CD25, as well as the upregulation of surface CD69 24 h proceeding BH. Because CD25 is the α chain of the IL-2 receptor, its upregulated surface expression is crucial for activated T-cells to be able to respond to IL-2 and undergo expansion[107]. This elevated phenotypic activation of the PMELs also strongly correlated with antigen positive cDCs (Figure3-7). In addition to the increase in PMEL activation status at this acute timepoint, there was also a trend towards a higher degree of tumor-specific T-cell proliferation and expansion post BH. This effect was not significant as two samples in the BH group did not mirror the response of the rest of the cohort. Given what we now know about the potency and differential immune responses elicited by BH in the TME, and how cDC1 activation is dependent on the level of tumor debulking observed, it is possible that BH treatment of those tumors did not induce endogenous bubble formation and cavitation. While the Cavitation Scores recorded for those two tumors resembled those observed in the remaining cohort, this metric is subjective as it is acquired via qualitative B-mode assessment. Furthermore, the effects we observed on PMEL activation were not contained to the TDLNs, as we found that PMELs that had seeded the cLNs of BH-treated mice also experienced elevated activation status and increased T-cell proliferation. Importantly, we demonstrated that impeding cDC migration with **α**CCR7 blockade did not inhibit PMEL proliferation in response to BH, suggesting that LN-resident cells initiated adaptive immune activation in response to mechanical insult by BH.

When we examined the number of PMELs that had not undergone division in the Sham and BH cohorts, we found that there was an equal number across both treatment conditions. The equivalent number of undivided PMELs suggests that enhanced division of PMELs observed in the BH treated mice is due to signals from augmented antigen presentation rather than just an increase in tumor antigen positive cDCs, This finding aligns with our previous results which showed that BH induced a greater level of phenotypic activation on antigen consuming cDCs when compared to ZsG^+ cDCs from Sham TDLNs. An area of future study should involve assessing whether antigen immunogenicity is altered by BH treatment. This could be tested by immunoprecipitating ZsG, gp100, and/or TRP-2 tumor antigen from Sham or BH treated tumor lysates for a coculture with bone marrow derived or lymphoid sorted cDCs. Immunogenicity can be measured by the ability of pulled down antigen to induce upregulation of costimulatory molecules and IL-12 production by the cocultured cDCs.

While our data infers that superior tumor-specific T-cell activation is the result of increased tumor antigen acquisition by cDCs, further studies are needed to test this. We propose the use of the genetic model $Zbtb46^{dtr}$, which will allow for the elimination of classical cDCs through the administration of diphtheria toxin. If cDCs are responsible for inducing PMEL activation and expansion post BH, then we would hypothesize that the loss of the cDC populations would abrogate T-cell activation following BH treatment. Alternatively, we can determine whether cDC1s or cDC2s are directly cross-presenting antigen to the PMELs by sorting ZsG^+ cDC1s and ZsG^+ cDC2s from the TDLNs of BH treated mice, and coculturing these cDCs with PMELs to determine which cell subset is responsible for tumor-specific T-cell expansion induced by BH.

Questions that arise from these findings are that if BH is showing evidence of systemic tumor-specific T-cell activation, why are tumor growth control and lengthened survival not sustained? Maybe these activated T-cells are not making their way into the tumors following this mechanical ablation regimen. This would occur if the tumor vasculature was not compatible to promote T-cell infiltration[115]. In the future, the ability of the PMELs to infiltrate into primary and distal malignancies could be monitored through positron emission tomography (PET) imaging, if the PMELs are radiolabeled prior to adoptive transfer. Alternatively, if the activated T-cells are infiltrating into the tumor, they may become exhausted due to the immunosuppressive TME and chronic antigen stimulation. Another possibility could be due to the variability in PMEL activation. BH was not able to elicit activation of PMEL $CD8^+$ T-cells isolated from 10-month-old, aged mice, which reportedly have reduced metabolically capabilities compared to PMELs isolated from younger 2-month-old mice, and BH could not overcome FTY720 suppression on T-cell activation. However, in both these settings, the PMELs from our positive control cohort that received anti-CD40, poly:ICLC and gp100 vaccination robustly responded, underwent activation and expanded. We have previously published that the increased activation status of cDCs post BH is much lower than what is observed following TLR agonism with polyI:CLC. Additionally, there is an ongoing clinical trial (NCT06472661) at UVA combining T-FUS with intratumoral polyI:CLC administration to regionally advanced melanoma patients[188]. Therefore, it would be rational to combine polyI:CLC with BH as a dual therapy in the future. As BH results in the liberation and drainage of antigen to the TDLNs, polyI:CLC could be employed to further induce the activation of LN-resident cDCs that had acquired the antigen. This additional stimulation may be enough to consistently promote tumor-specific T-cell activation, expansion, and potentially T-cell mediated growth control.

Localization of tumor antigen in the TDLNs following BH-mediated antigen liberation

The effects mechanically lysing tumors with BH has on tumor antigen dispersion and interaction of this antigen with APC subsets in the TDLNs was unknown. Our immunofluorescence data indicates that released tumor antigen localizes around the periphery of the TDLNs, significantly overlapping with regions of the lymphatic sinuses (Figure 3-3). As the LN is a well-organized structure, the most abundant APCs in these regions are LN-resident cDC2s and subcapsular macrophages[7,103,104]. Migratory cDC1s reside deeper within the paracortex region of the lymph nodes and will not encounter large particulate antigen[6,8]. Therefore, antigen liberated post BH is more likely to encounter and be phagocytosed by LN-resident cDC2s and subcapsular macrophages. cDC2s predominately present antigen to $CD4^+$ T-cells, and subcapsular macrophages present antigen acquired from the lymph to B-cells[5,103,104]. While neither of these cell types is thought to commonly interact with $CD8^+$ T-cells, both have been shown to mediate $CD8^+$ T-cell responses in certain contexts. $CD169^+$ macrophages have been found in the boundary between the LN sinus and the intersection between the T-cell zone and B-cell follicle. These cells can also cross-present dead cell-associated antigens, such as dead tumor cells, directly to $CD8^+$ T-cells to confer protective immunity[104]. On the other hand, when cDC2s engulf antibody-associated tumor antigens, they have been shown to directly cross-present that antigen to $CD8^+$ T-cells as well[5]. If BH-mediated PMEL expansion is the result of cross-presentation by $CD169^+$ macrophages or cDC2s, then it would inform us of the state of the antigen being liberated and drained to the TDLNs via BH. Importantly, this data only represents an acute snapshot of where the antigen was located 2 h post BH ablation. In the future, time course studies monitoring dispersion of tumor antigen would be crucial for understanding

whether these antigen eventually makes it deeper into the TDLNs via the conduit network, where it is has a higher chance of encountering cDC1s capable of cross-presenting tumor antigen to $CD8^+$ T-cells, or if majority of the antigen remains contained to the outer edges of the LNs, confined to the lymphatic sinus.

While this data provides us insight into tumor antigen availability within the TDLNs following BH treatment, we are also left with further questions. Upon adoptive transfer naïve $CD8^+$ T-cells reside in the paracortex region of the LN, while central memory $CD8^+$ T-cells localize to the cortical edge, near the boundary of B-cell/T-cell boundary[189] – in closer proximity to the lymphatic sinuses. Therefore, a key piece of missing information is where, spatially, within the TDLNs are activated tumor-specific T-cells, and what APCs are they interacting with? Are they near antigen positive cDCs? If so, which cDC subset? Is their compartmental location altered following BH treatment? Where exactly within the TDLNs are the antigen engulfing, phenotypically activated cDCs? Our current IF approaches have insufficient resolution required to answer these questions. To be more definitive in our identification of cDC subsets, antigen dissemination, PMEL localization, and activation states further studies should employ a multiplex imaging approach. This would allow us to visualize cell-cell interactions that may be mediated following BH-induced immunity.

Discrepancies in intratumoral immunological consequences mediated by BH

The primary goal of these studies was to develop a more complete understanding of how BH was impacting the immune system. Our prior work focused on the dissemination of tumor antigen to the TDLNs and how immune cell populations were responding to antigen within the TDLN[75]. However, a longstanding question was how is BH impacting the immune cells at the site of mechanical ablation? Utilizing conserved treatment parameters, we predicted that

treatment efficacy and effects on primary tumor outgrowth would be consistent. This was not the case. In some instances, BH resulted in tumor debulking and constrain of tumor-outgrowth, while in others, there was no evidence of debulking. Flow cytometric analysis of these tumor showed distinct alterations to the immune repertoire in the TME based on the level of primary growth control observed. In tumors where outgrowth was inhibited, significant reductions were seen in APC subsets – including cDC1s, cDC2s, and macrophages – while no differences in APC presence was seen in the non-debulked setting. In the debulked setting, these cells ultimately repopulate the TME by 96 h post BH. However, how functionally similar the newly infiltrated cDCs and macrophages are to the cells that were previously present in the TME remains unknown. cDCs retained in the TME can develop an exhausted signature, distinct from cDCs found in the TDLNs[124], and macrophages can transition into immunosuppressive TAMs when sequestered in the TME under chronic antigen exposure and cytokine stimuli. Determining if BH abrogates and eliminates exhausted, tumor-retained cDCs, and subsequently allows for the repopulation of non-immunosuppressed cDCs capable of initiating $CD8^+$ T-cell activation, is important when considering BH's potential as a cancer therapeutic.

We also found that when tumor-debulking was achieved by BH, there was a significant increase in the proportion of ZsG tumor antigen positive APCs acutely – 24 h following treatment – and most of these effects were sustained in the TME through 96 h. The engulfment of antigen by cDCs in the TME indicates that BH-induced liberated tumor antigen is not entirely sequestered by the highly phagocytic macrophage population. It is of note that while we maintained increased antigen presence in cDCs at the 96 h timepoint, we do not observe differences between the Sham and BH cohorts in ZsG^+ cDCs in the TDLNs at that same timepoint. This may indicate that cDCs acquiring antigen in the TME post BH are not migrating

to the TDLNs. A limitation to these studies is the resolution of ZsG staining in the tumors. We could not compare the GMF of ZsG on ZsG^+ APCs across samples because of the unique shift in the ZsG intensity within each APC examined. Therefore, we cannot conclude whether BH is resulting in changes to the amount of antigen these cells are consuming on a per cell basis. Future studies are needed to optimize this staining approach, and quench external ZsGreen presence to avoid the shifts observed in ZsG intensity from sample to sample. Additionally, the ImageStream system can be further employed to confirm external versus internal ZsG presence with an anti-ZsGreen fluorescent antibody to tag non-endocytosed antigen.

The differences in immune alterations between debulked and non-debulked tumors carried over to distinct alterations in cDC activation status. CD86 upregulation and activation was promoted almost exclusively in the cDC1 population (Figures 4-8B-F & 4-9B-I), while in the non-debulked setting, activation was only seen in the cDC2 population (Figure 4-8G-K & 4-9J-Q). This effect was not dependent on ZsG antigen acquisition, suggesting that the inflammatory stimuli induce by BH is sufficient to promote cDC activation. This finding contrast what we have previously observed in the TDLNs, where cDC activation was dependent on ZsG acquisition[75]. One rationale for this may be that immune stimuli such as DAMPs induced by BH are staying in the TME and not making their way to the TDLNs. Therefore, non-tumor antigen engulfing cDCs in the TDLNs are not being exposed to these immunostimulatory signals, therefore, they are not expressing equivalent markers of activation compared to the ZsG^+ cDCs. As this is just a phenotypic assessment of activation, future studies should be performed to determine the functional capacity of these cells, such as their ability to effectively process and cross-present the tumor antigen. This could be tested by sorting ZsG^+ cDCs from the BH and Sham treated tumors, and coculturing them with PMEL and/or TRP-2 T-cells to determine

differences in tumor-specific T-cell activation. We also propose the use of a B16-ZsGminOVA model, which expresses the peptides specific for OT-I and OT-II T-cells, to measure MHC-peptide complexes and cross-presentation by these cDCs in the future.

While these studies provided insight into how BH impacts the APC compartment in melanoma tumors, we have yet to examine the impacts these different debulking regimens have on T-cell presence and activation in the TME. Does the elevated activation status of cDC1s in the debulked state correlate to increased $CD8^+$ T-cell infiltration and activation? If so, is it absent in the non-debulked setting? Do increases in cDC2 activation status result in $CD4^+$ T-cell accumulation in the tumors – are they helper or regulatory cells? Although these studies have addressed unknowns in the field, many more interrogations remain.

Additionally, these findings raise an important question: why were these outcomes so different if conserved parameters were used across all studies? Although the same murine tumor model and mouse strain was used in all these studies, this cell line is polyclonal. Therefore, inherently within these tumors is genetic variability and heterogeneity. While we opted to use polyclonal tumors to better mimic the variability seen in human cancer, it may be a caveat in these studies. Another explanation for the dissimilarities in tumor outgrowth could involve the heterogenous and unique development of each TME. Alterations to the stromal and immune make-up of a TME can result in changes to the overall stiffness of the tissue, which could hinder the ability of the ultrasound to effectively mechanically ablate the tissue. On stiffer tissues, the frequency of the BH being applied may need to be increased to reduce the duty cycle and enhance ablative efficacy. To determine whether tumor stiffness plays a role in BH-induced tumor control, elastography could be performed on tumors from the BH-cohort prior to treatment. Not only can we measure the correlation of tumor stiffness to the propensity of BH to

result in tumor control, but we can also utilize our qualitative B-mode assessment to further determine whether tumor rigidity is impacting the formation of a cavitation cloud. However, the most optimal way to quantify BH intensity and endogenous bubble cavitation would be through the development of a PCD monitoring approach. A quantitative measurement could eventually allow for real-time alterations and tuning of BH treatment regimens to induce tumor destruction, and potentially skew cDC1: $CD8^+$ T-cell activation.

Gemcitabine – not a myeloablative chemotherapy in the TME

Previous work by *Sheybani et al*. described a T-cell mediated combinatorial treatment regimen of TFUS+GEM for TNBC. While we had initially set out to determine the basis of enhanced T-cell control initiated by TFUS+GEM, we became privy to lack of understanding regarding the effects of GEM as a monotherapy on immune cells in the TME. In preclinical BrCa models, GEM had been deemed a myeloablative therapy, as it significantly reduced the presence of GR-1^+ MDSCs[144] in the periphery of tumor-bearing mice without perturbing adaptive immune cell populations[145,146]. We were able to replicate the systemic effects of GEM on immune cells subsets observed in previous studies performed in the 4T1 murine TNBC model (Figures 5-13 & 5-14). However, in contrast to the effects on circulating immune cells, we found that GEM treatment did not have myeloablative effects in the TME. Tumoral granulocytic, monocytic and macrophage populations were unaltered following GEM treatment (Figure 5-16). While we had initially hypothesized that GEM would spare adaptive immune related cells in the TME, we discovered that GEM induced significant reductions to $CD8^+$ and $CD4^+$ T-cell populations, as well as cDCs (Figure 5-19). Given the diminution in TILs, the combination of GEM and ICB may not be efficacious. This could explain the minimally improved efficacy of TFUS+GEM and anti-PD-1 treatment previously reported[84].

Despite the reduction of the T-cell presence in these tumors, bulk RNA-seq of TNBC tumors 24 h and 7 days after GEM treatment revealed upregulation of genes and pathways associated with immune activation, one of which being the IFN-γ response pathway (Figure 5-20). While GEM treatment resulted in increased production of IFN-γ by granulocytes in the TME (Figure 5-21), neutralizing this inflammatory cytokine neither abrogated nor improved GEM-mediated tumor control (Figure 5-23). In addition to IFN-γ production, we reported alterations in Arg1 expression following GEM administration. As the presence of Arg1 in human and murine BrCa correlates with poor prognosis and increased immunosuppression[22], these findings suggest that the use of Arg1 inhibitors in combination with GEM may improve therapeutic efficacy.

In these studies, we interrogated the immunological impact of a single dose of systemic GEM. A standard infusion schedule for patients receiving this drug is 1000mg/m^2 administered on days 1, 8, 15 and 28 of a cycle. Here, we mimicked the single dose given to patients enrolled in the Breast 54 trial (NCT04796220) combining T-FUS with GEM[190]. Future studies could consider whether multiple treatments with this chemotherapy mimic or deviate from the effects we observe in terms of immune cell perturbations. Importantly, we observed that different brands of GEM can result in varied transcriptional changes in TNBC tumors (Figures 5-10 - 5-12), with only 3% of DEGs in 4T1 tumors being conserved between the two tested brands of GEM (Figure 5-10). Therefore, these results should be repeated with one's available GEM stock before assuming all immunological effects are conserved across various manufacturers.

Chapter Seven: References

1. Chen, D. S. & Mellman, I. Oncology Meets Immunology: The Cancer-Immunity Cycle. *Immunity* **39**, 1–10 (2013).
2. Liu, K. Dendritic Cells. in *Encyclopedia of Cell Biology* 741–749 (Elsevier, 2016). doi:10.1016/B978-0-12-394447-4.30111-0.
3. Ohl, L. *et al.* CCR7 Governs Skin Dendritic Cell Migration under Inflammatory and Steady-State Conditions. *Immunity* **21**, 279–288 (2004).
4. Roberts, E. W. *et al.* Critical Role for CD103+/CD141+ Dendritic Cells Bearing CCR7 for Tumor Antigen Trafficking and Priming of T Cell Immunity in Melanoma. *Cancer Cell* **30**, 324–336 (2016).
5. Jo, S. *et al.* Shared pathway of WDFY4-dependent cross-presentation of immune complexes by cDC1 and cDC2. *Journal of Experimental Medicine* **222**, e20240955 (2025).
6. Gerner, M. Y., Kastenmuller, W., Ifrim, I., Kabat, J. & Germain, R. N. Histo-Cytometry: A Method for Highly Multiplex Quantitative Tissue Imaging Analysis Applied to Dendritic Cell Subset Microanatomy in Lymph Nodes. *Immunity* **37**, 364–376 (2012).
7. Gerner, M. Y., Torabi-Parizi, P. & Germain, R. N. Strategically Localized Dendritic Cells Promote Rapid T Cell Responses to Lymph-Borne Particulate Antigens. *Immunity* **42**, 172–185 (2015).
8. Ugur, M. *et al.* Lymph node medulla regulates the spatiotemporal unfolding of resident dendritic cell networks. *Immunity* **56**, 1778-1793.e10 (2023).
9. Ruhland, M. K. *et al.* Visualizing Synaptic Transfer of Tumor Antigens among Dendritic Cells. *Cancer Cell* **37**, 786-799.e5 (2020).

10. Pennock, N. D. *et al.* T cell responses: naïve to memory and everything in between. *Advances in Physiology Education* **37**, 273–283 (2013).

11. Prokhnevska, N. *et al.* CD8+ T cell activation in cancer comprises an initial activation phase in lymph nodes followed by effector differentiation within the tumor. *Immunity* **56**, 107-124.e5 (2023).

12. Kaplan, D. H. *et al.* Demonstration of an interferon γ-dependent tumor surveillance system in immunocompetent mice. *Proc. Natl. Acad. Sci. U.S.A.* **95**, 7556–7561 (1998).

13. Shankaran, V. *et al.* IFNγ and lymphocytes prevent primary tumour development and shape tumour immunogenicity. *Nature* **410**, 1107–1111 (2001).

14. Galon, J. *et al.* Type, Density, and Location of Immune Cells Within Human Colorectal Tumors Predict Clinical Outcome. *Science* **313**, 1960–1964 (2006).

15. Erdag, G. *et al.* Immunotype and Immunohistologic Characteristics of Tumor-Infiltrating Immune Cells Are Associated with Clinical Outcome in Metastatic Melanoma. *Cancer Research* **72**, 1070–1080 (2012).

16. Van Houdt, I. S. *et al.* Favorable outcome in clinically stage II melanoma patients is associated with the presence of activated tumor infiltrating T-lymphocytes and preserved MHC class I antigen expression. *Intl Journal of Cancer* **123**, 609–615 (2008).

17. Azimi, F. *et al.* Tumor-Infiltrating Lymphocyte Grade Is an Independent Predictor of Sentinel Lymph Node Status and Survival in Patients With Cutaneous Melanoma. *JCO* **30**, 2678–2683 (2012).

18. Dunn, G. P., Bruce, A. T., Ikeda, H., Old, L. J. & Schreiber, R. D. Cancer immunoediting: from immunosurveillance to tumor escape. *Nat Immunol* **3**, 991–998 (2002).

19. Salemme, V., Centonze, G., Cavallo, F., Defilippi, P. & Conti, L. The Crosstalk Between Tumor Cells and the Immune Microenvironment in Breast Cancer: Implications for Immunotherapy. *Front. Oncol.* **11**, 610303 (2021).

20. Mittal, S. K., Cho, K.-J., Ishido, S. & Roche, P. A. Interleukin 10 (IL-10)-mediated Immunosuppression. *Journal of Biological Chemistry* **290**, 27158–27167 (2015).

21. Yang, L., Pang, Y. & Moses, H. L. TGF-β and immune cells: an important regulatory axis in the tumor microenvironment and progression. *Trends in Immunology* **31**, 220–227 (2010).

22. Su, X. *et al.* Breast cancer–derived GM-CSF regulates arginase 1 in myeloid cells to promote an immunosuppressive microenvironment. *Journal of Clinical Investigation* **131**, e145296 (2021).

23. Muz, B., De La Puente, P., Azab, F. & Azab, A. K. The role of hypoxia in cancer progression, angiogenesis, metastasis, and resistance to therapy. *HP* 83 (2015) doi:10.2147/HP.S93413.

24. Chang, C.-H. *et al.* Metabolic Competition in the Tumor Microenvironment Is a Driver of Cancer Progression. *Cell* **162**, 1229–1241 (2015).

25. Dong, H. *et al.* Tumor-associated B7-H1 promotes T-cell apoptosis: A potential mechanism of immune evasion. *Nat Med* **8**, 793–800 (2002).

26. Lanitis, E., Irving, M. & Coukos, G. Targeting the tumor vasculature to enhance T cell activity. *Current Opinion in Immunology* **33**, 55–63 (2015).

27. Lee, P. P. *et al.* Characterization of circulating T cells specific for tumor-associated antigens in melanoma patients. *Nat Med* **5**, 677–685 (1999).

28. Sharma, P., Hu-Lieskovan, S., Wargo, J. A. & Ribas, A. Primary, Adaptive, and Acquired Resistance to Cancer Immunotherapy. *Cell* **168**, 707–723 (2017).

29. Melanoma Research Foundation.pdf.

30. American Cancer Society_melanoma.pdf.

31. Immune Checkpoint Inhibitors - NCI.pdf.

32. Hamid, O. *et al.* Five-year survival outcomes for patients with advanced melanoma treated with pembrolizumab in KEYNOTE-001. *Annals of Oncology* **30**, 582–588 (2019).

33. Robert, C. *et al.* Pembrolizumab versus Ipilimumab in Advanced Melanoma. *N Engl J Med* **372**, 2521–2532 (2015).

34. Rizzetto, G., De Simoni, E., Molinelli, E., Offidani, A. & Simonetti, O. Efficacy of Pembrolizumab in Advanced Melanoma: A Narrative Review. *IJMS* **24**, 12383 (2023).

35. Lim, S. Y. *et al.* The molecular and functional landscape of resistance to immune checkpoint blockade in melanoma. *Nat Commun* **14**, 1516 (2023).

36. Ribas, A. *et al.* Association of Pembrolizumab With Tumor Response and Survival Among Patients With Advanced Melanoma. *JAMA* **315**, 1600 (2016).

37. American Cancer Society - Cancer Facts & Figures 2023. https://www.cancer.org/content/dam/cancer-org/research/cancer-facts-and-statistics/annual-cancer-facts-and-figures/2023/2023-cancer-facts-and-figures.pdf (2024).

38. Bauer, K. R., Brown, M., Cress, R. D., Parise, C. A. & Caggiano, V. Descriptive analysis of estrogen receptor (ER)-negative, progesterone receptor (PR)-negative, and HER2-negative invasive breast cancer, the so-called triple-negative phenotype: a population-based study from the California cancer Registry. *Cancer* **109**, 1721–1728 (2007).

39. Dent, R. *et al.* Triple-Negative Breast Cancer: Clinical Features and Patterns of Recurrence. *Clinical Cancer Research* **13**, 4429–4434 (2007).

40. Vargo, J. A. *et al.* Molecular Class as a Predictor of Locoregional and Distant Recurrence in the Neoadjuvant Setting for Breast Cancer. *Oncology* **80**, 341–349 (2011).

41. Jwa, E. *et al.* Locoregional Recurrence by Tumor Biology in Breast Cancer Patients after Preoperative Chemotherapy and Breast Conservation Treatment. *Cancer Res Treat* **48**, 1363–1372 (2016).

42. Swisher, S. K. *et al.* Locoregional Control According to Breast Cancer Subtype and Response to Neoadjuvant Chemotherapy in Breast Cancer Patients Undergoing Breast-conserving Therapy. *Ann Surg Oncol* **23**, 749–756 (2016).

43. Lin, N. U. *et al.* Sites of distant recurrence and clinical outcomes in patients with metastatic triple-negative breast cancer: High incidence of central nervous system metastases. *Cancer* **113**, 2638–2645 (2008).

44. Cortes, J. *et al.* Pembrolizumab plus Chemotherapy in Advanced Triple-Negative Breast Cancer. *N Engl J Med* **387**, 217–226 (2022).

45. Kulangara, K. *et al.* PD-L1 IHC 22C3 pharmdx demonstrates precision and reproducibility in detecting PD-L1 expression in triple negative breast cancer. *JCO* **38**, e13104–e13104 (2020).

46. Mittendorf, E. A. *et al.* PD-L1 Expression in Triple-Negative Breast Cancer. *Cancer Immunology Research* **2**, 361–370 (2014).

47. Ghebeh, H. *et al.* The B7-H1 (PD-L1) T Lymphocyte-Inhibitory Molecule Is Expressed in Breast Cancer Patients with Infiltrating Ductal Carcinoma: Correlation with Important High-Risk Prognostic Factors. *Neoplasia* **8**, 190–198 (2006).

48. Dunn, G. P., Old, L. J. & Schreiber, R. D. The Immunobiology of Cancer Immunosurveillance and Immunoediting. *Immunity* **21**, 137–148 (2004).

49. Casbon, A.-J. *et al.* Invasive breast cancer reprograms early myeloid differentiation in the bone marrow to generate immunosuppressive neutrophils. *Proc. Natl. Acad. Sci. U.S.A.* **112**, (2015).

50. Bronte, V. *et al.* Unopposed production of granulocyte-macrophage colony-stimulating factor by tumors inhibits CD8+ T cell responses by dysregulating antigen-presenting cell maturation. *J Immunol* **162**, 5728–5737 (1999).

51. Pak, A. S. *et al.* Mechanisms of immune suppression in patients with head and neck cancer: presence of CD34(+) cells which suppress immune functions within cancers that secrete granulocyte-macrophage colony-stimulating factor. *Clin Cancer Res* **1**, 95–103 (1995).

52. Feng, S. *et al.* Myeloid-derived suppressor cells inhibit T cell activation through nitrating LCK in mouse cancers. *Proc. Natl. Acad. Sci. U.S.A.* **115**, 10094–10099 (2018).

53. Yang, L. *et al.* Expansion of myeloid immune suppressor Gr+CD11b+ cells in tumor-bearing host directly promotes tumor angiogenesis. *Cancer Cell* **6**, 409–421 (2004).

54. Okazaki, T. *et al.* Granulocyte colony-stimulating factor promotes tumor angiogenesis via increasing circulating endothelial progenitor cells and Gr1+CD11b+ cells in cancer animal models. *International Immunology* **18**, 1–9 (2006).

55. Kumar, S. *et al.* ΔNp63-driven recruitment of myeloid-derived suppressor cells promotes metastasis in triple-negative breast cancer. *Journal of Clinical Investigation* **128**, 5095–5109 (2018).

56. Siret, C. *et al.* Deciphering the Crosstalk Between Myeloid-Derived Suppressor Cells and Regulatory T Cells in Pancreatic Ductal Adenocarcinoma. *Front. Immunol.* **10**, 3070 (2020).

57. Corzo, C. A. *et al.* HIF-1α regulates function and differentiation of myeloid-derived suppressor cells in the tumor microenvironment. *Journal of Experimental Medicine* **207**, 2439–2453 (2010).

58. Jordan, K. R. *et al.* Myeloid-derived suppressor cells are associated with disease progression and decreased overall survival in advanced-stage melanoma patients. *Cancer Immunol Immunother* **62**, 1711–1722 (2013).

59. Gonda, K. *et al.* Myeloid-derived suppressor cells are increased and correlated with type 2 immune responses, malnutrition, inflammation, and poor prognosis in patients with breast cancer. *Oncology Letters* **14**, 1766–1774 (2017).

60. Pruneri, G., Vingiani, A. & Denkert, C. Tumor infiltrating lymphocytes in early breast cancer. *The Breast* **37**, 207–214 (2018).

61. Wang, K., Xu, J., Zhang, T. & Xue, D. Tumor-infiltrating lymphocytes in breast cancer predict the response to chemotherapy and survival outcome: A meta-analysis. *Oncotarget* **7**, 44288–44298 (2016).

62. Zhou, Y.-F. High intensity focused ultrasound in clinical tumor ablation. *WJCO* **2**, 8 (2011).

63. Curley, C. T., Sheybani, N. D., Bullock, T. N. & Price, R. J. Focused Ultrasound Immunotherapy for Central Nervous System Pathologies: Challenges and Opportunities. *Theranostics* **7**, 3608–3623 (2017).

64. Khokhlova, T. D. *et al.* Pilot in vivo studies on transcutaneous boiling histotripsy in porcine liver and kidney. *Sci Rep* **9**, 20176 (2019).

65. Williams, R. P., Simon, J. C., Khokhlova, V. A., Sapozhnikov, O. A. & Khokhlova, T. D. The histotripsy spectrum: differences and similarities in techniques and instrumentation. *Int J Hyperthermia* **40**, 2233720 (2023).

66. Hoogenboom, M. *et al. In vivo* MR guided boiling histotripsy in a mouse tumor model evaluated by MRI and histopathology: *In vivo* MR Guided Boiling Histotripsy. *NMR Biomed.* **29**, 721–731 (2016).

67. Hu, Z. *et al.* Release of endogenous danger signals from HIFU-treated tumor cells and their stimulatory effects on APCs. *Biochemical and Biophysical Research Communications* **335**, 124–131 (2005).

68. Kruse, D. E., Mackanos, M. A., O'Connell-Rodwell, C. E., Contag, C. H. & Ferrara, K. W. Short-duration-focused ultrasound stimulation of Hsp70 expression *in vivo*. *Phys. Med. Biol.* **53**, 3641–3660 (2008).

69. Nam, G. *et al.* Investigation of the Potential Immunological Effects of Boiling Histotripsy for Cancer Treatment. *Advanced Therapeutics* **3**, 1900214 (2020).

70. Hundt, W., O'Connell-Rodwell, C. E., Bednarski, M. D., Steinbach, S. & Guccione, S. In Vitro Effect of Focused Ultrasound or Thermal Stress on HSP70 Expression and Cell Viability in Three Tumor Cell Lines. *Academic Radiology* **14**, 859–870 (2007).

71. Wu, F. *et al.* Expression of Tumor Antigens and Heat-Shock Protein 70 in Breast Cancer Cells After High-Intensity Focused Ultrasound Ablation. *Ann Surg Oncol* **14**, 1237–1242 (2007).

72. Xu, Z.-L. *et al.* Activation of Tumor-Infiltrating Antigen Presenting Cells by High Intensity Focused Ultrasound Ablation of Human Breast Cancer. *Ultrasound in Medicine & Biology* **35**, 50–57 (2009).

73. Yuan, S.-M. *et al.* High intensity focused ultrasound enhances anti-tumor immunity by inhibiting the negative regulatory effect of miR-134 on CD86 in a murine melanoma model. *Oncotarget* **6**, 37626–37637 (2015).

74. Van Den Bijgaart, R. J. E. *et al.* Mechanical high-intensity focused ultrasound creates unique tumor debris enhancing dendritic cell-induced T cell activation. *Front. Immunol.* **13**, 1038347 (2022).

75. Thim, E. A. *et al.* Focused ultrasound ablation of melanoma with boiling histotripsy yields abscopal tumor control and antigen-dependent dendritic cell activation. *Theranostics* **14**, 1647–1661 (2024).

76. Xia, J.-Z. *et al.* High-Intensity Focused Ultrasound Tumor Ablation Activates Autologous Tumor-Specific Cytotoxic T Lymphocytes. *Ultrasound in Medicine & Biology* **38**, 1363–1371 (2012).

77. Lu, P. *et al.* Increased infiltration of activated tumor-infiltrating lymphocytes after high intensity focused ultrasound ablation of human breast cancer. *Surgery* **145**, 286–293 (2009).

78. Wu, F. *et al.* Activated anti-tumor immunity in cancer patients after high intensity focused ultrasound ablation. *Ultrasound in Medicine & Biology* **30**, 1217–1222 (2004).

79. Abe, S. *et al.* Combination of ultrasound-based mechanical disruption of tumor with immune checkpoint blockade modifies tumor microenvironment and augments systemic antitumor immunity. *J Immunother Cancer* **10**, e003717 (2022).

80. Zhou, Q. *et al.* Changes in Circulating Immunosuppressive Cytokine Levels of Cancer Patients After High Intensity Focused Ultrasound Treatment. *Ultrasound in Medicine & Biology* **34**, 81–87 (2008).

81. Qu, S. *et al.* Non-thermal histotripsy tumor ablation promotes abscopal immune responses that enhance cancer immunotherapy. *J Immunother Cancer* **8**, e000200 (2020).

82. Singh, M. P. *et al.* In-situ vaccination using focused ultrasound heating and anti-CD-40 agonistic antibody enhances T-cell mediated local and abscopal effects in murine melanoma. *Int J Hyperthermia* **36**, 64–73 (2019).

83. Chavez, M. *et al.* Distinct immune signatures in directly treated and distant tumors result from TLR adjuvants and focal ablation. *Theranostics* **8**, 3611–3628 (2018).

84. Sheybani, N. D. *et al.* Combination of thermally ablative focused ultrasound with gemcitabine controls breast cancer via adaptive immunity. *J Immunother Cancer* **8**, e001008 (2020).

85. Clinicaltrials.gov - search = thermal ablation. https://clinicaltrials.gov/search?intr=Thermal%20Ablation.

86. Clinicaltrials.gov - search = histotripsy. https://clinicaltrials.gov/search?intr=Histotripsy.

87. Kolaczkowska, E. & Kubes, P. Neutrophil recruitment and function in health and inflammation. *Nat Rev Immunol* **13**, 159–175 (2013).

88. Le, H. K. *et al.* Gemcitabine directly inhibits myeloid derived suppressor cells in BALB/c mice bearing 4T1 mammary carcinoma and augments expansion of T cells from tumor-bearing mice. *International Immunopharmacology* **9**, 900–909 (2009).

89. Ewels, P., Magnusson, M., Lundin, S. & Käller, M. MultiQC: summarize analysis results for multiple tools and samples in a single report. *Bioinformatics* **32**, 3047–3048 (2016).

90. Dobin, A. *et al.* STAR: ultrafast universal RNA-seq aligner. *Bioinformatics* **29**, 15–21 (2013).

91. Love, M. I., Huber, W. & Anders, S. Moderated estimation of fold change and dispersion for RNA-seq data with DESeq2. *Genome Biol* **15**, 550 (2014).

92. Zhu, A., Ibrahim, J. G. & Love, M. I. Heavy-tailed prior distributions for sequence count data: removing the noise and preserving large differences. *Bioinformatics* **35**, 2084–2092 (2019).

93. Liberzon, A. *et al.* Molecular signatures database (MSigDB) 3.0. *Bioinformatics* **27**, 1739–1740 (2011).

94. Liberzon, A. A Description of the Molecular Signatures Database (MSigDB) Web Site. in *Stem Cell Transcriptional Networks* (ed. Kidder, B. L.) vol. 1150 153–160 (Springer New York, New York, NY, 2014).

95. Liberzon, A. *et al.* The Molecular Signatures Database Hallmark Gene Set Collection. *Cell Systems* **1**, 417–425 (2015).

96. Edwards, J. *et al.* CD103+ Tumor-Resident CD8+ T Cells Are Associated with Improved Survival in Immunotherapy-Naïve Melanoma Patients and Expand Significantly During Anti–PD-1 Treatment. *Clinical Cancer Research* **24**, 3036–3045 (2018).

97. Khokhlova, T. D. *et al.* Ultrasound-guided tissue fractionation by high intensity focused ultrasound in an in vivo porcine liver model. *Proc. Natl. Acad. Sci. U.S.A.* **111**, 8161–8166 (2014).

98. Sixt, M. *et al.* The Conduit System Transports Soluble Antigens from the Afferent Lymph to Resident Dendritic Cells in the T Cell Area of the Lymph Node. *Immunity* **22**, 19–29 (2005).

99. Gretz, J. E., Kaldjian, E. P., Anderson, A. O. & Shaw, S. Sophisticated strategies for information encounter in the lymph node: the reticular network as a conduit of soluble information and a highway for cell traffic. *J Immunol* **157**, 495–499 (1996).

100. Roozendaal, R., Mebius, R. E. & Kraal, G. The conduit system of the lymph node. *International Immunology* **20**, 1483–1487 (2008).

101. Misslitz, A. *et al.* Thymic T Cell Development and Progenitor Localization Depend on CCR7. *The Journal of Experimental Medicine* **200**, 481–491 (2004).

102. Meeth, K., Wang, J. X., Micevic, G., Damsky, W. & Bosenberg, M. W. The YUMM lines: a series of congenic mouse melanoma cell lines with defined genetic alterations. *Pigment Cell Melanoma Res* **29**, 590–597 (2016).

103. Junt, T. Subcapsular sinus macrophages in lymph nodes clear lymph-borne viruses and present them to antiviral B cells.

104. Asano, K. *et al.* CD169-Positive Macrophages Dominate Antitumor Immunity by Crosspresenting Dead Cell-Associated Antigens. *Immunity* **34**, 85–95 (2011).

105. Overwijk, W. W. *et al.* Tumor regression and autoimmunity after reversal of a functionally tolerant state of self-reactive CD8+ T cells. *J Exp Med* **198**, 569–580 (2003).

106. Lindsey, W. B. *et al.* CD69 expression as an index of T-cell function: assay standardization, validation and use in monitoring immune recovery. *Cytotherapy* **9**, 123–132 (2007).

107. Peng, Y. *et al.* CD25 : A potential tumor therapeutic target. *Intl Journal of Cancer* **152**, 1290–1303 (2023).

108. Brinkmann, V. *et al.* The Immune Modulator FTY720 Targets Sphingosine 1-Phosphate Receptors. *Journal of Biological Chemistry* **277**, 21453–21457 (2002).

109. Kissenpfennig, A. *et al.* Dynamics and Function of Langerhans Cells In Vivo. *Immunity* **22**, 643–654 (2005).

110. Vaena, S. *et al.* Aging-dependent mitochondrial dysfunction mediated by ceramide signaling inhibits antitumor T cell response. *Cell Rep* **35**, 109076 (2021).

111. Ntranos, A. *et al.* FTY720 impairs CD8 T-cell function independently of the sphingosine-1-phosphate pathway. *Journal of Neuroimmunology* **270**, 13–21 (2014).

112. Mazzola, M. A. *et al.* Identification of a novel mechanism of action of fingolimod (FTY720) on human effector T cell function through TCF-1 upregulation. *J Neuroinflammation* **12**, 245 (2015).

113. Baer, A., Colon-Moran, W. & Bhattarai, N. Characterization of the effects of immunomodulatory drug fingolimod (FTY720) on human T cell receptor signaling pathways. *Sci Rep* **8**, 10910 (2018).

114. Meredith, M. M. *et al.* Expression of the zinc finger transcription factor zDC (Zbtb46, Btbd4) defines the classical dendritic cell lineage. *Journal of Experimental Medicine* **209**, 1153–1165 (2012).

115. Karakousi, T., Mudianto, T. & Lund, A. W. Lymphatic vessels in the age of cancer immunotherapy. *Nat Rev Cancer* **24**, 363–381 (2024).

116. Ivanov, S. *et al.* CCR7 and IRF4-dependent dendritic cells regulate lymphatic collecting vessel permeability. *Journal of Clinical Investigation* **126**, 1581–1591 (2016).

117. Blair, T. C. *et al.* Fluorescent tracking identifies key migratory dendritic cells in the lymph node after radiotherapy. *Life Sci. Alliance* **5**, e202101337 (2022).

118. Menares, E. *et al.* Tissue-resident memory CD8+ T cells amplify anti-tumor immunity by triggering antigen spreading through dendritic cells. *Nat Commun* **10**, 4401 (2019).

119. Jensen, T. O. *et al.* Macrophage Markers in Serum and Tumor Have Prognostic Impact in American Joint Committee on Cancer Stage I/II Melanoma. *JCO* **27**, 3330–3337 (2009).

120. Hendricks-Wenger, A. *et al.* Histotripsy Ablation Alters the Tumor Microenvironment and Promotes Immune System Activation in a Subcutaneous Model of Pancreatic Cancer. *IEEE Trans Ultrason Ferroelectr Freq Control* **68**, 2987–3000 (2021).

121. Schade, G. R. *et al.* Boiling Histotripsy Ablation of Renal Cell Carcinoma in the Eker Rat Promotes a Systemic Inflammatory Response. *Ultrasound in Medicine & Biology* **45**, 137–147 (2019).

122. Waibl Polania, J. *et al.* Antigen presentation by tumor-associated macrophages drives T cells from a progenitor exhaustion state to terminal exhaustion. *Immunity* **58**, 232-246.e6 (2025).

123. Salgaonkar, V. A., Datta, S., Holland, C. K. & Mast, T. D. Passive cavitation imaging with ultrasound arrays. *J Acoust Soc Am* **126**, 3071–3083 (2009).

124. Lee, C. Y. C. *et al.* Tumour-retained activated CCR7+ dendritic cells are heterogeneous and regulate local anti-tumour cytolytic activity. *Nat Commun* **15**, 682 (2024).

125. Spranger, S., Dai, D., Horton, B. & Gajewski, T. F. Tumor-Residing Batf3 Dendritic Cells Are Required for Effector T Cell Trafficking and Adoptive T Cell Therapy. *Cancer Cell* **31**, 711-723.e4 (2017).

126. Salmon, H. *et al.* Expansion and Activation of CD103+ Dendritic Cell Progenitors at the Tumor Site Enhances Tumor Responses to Therapeutic PD-L1 and BRAF Inhibition. *Immunity* **44**, 924–938 (2016).

127. Wculek, S. K. *et al.* Dendritic cells in cancer immunology and immunotherapy. *Nat Rev Immunol* **20**, 7–24 (2020).

128. McGuire, A., Lowery, A. J., Kell, M. R., Kerin, M. J. & Sweeney, K. J. Locoregional Recurrence Following Breast Cancer Surgery in the Trastuzumab Era: A Systematic Review by Subtype. *Ann Surg Oncol* **24**, 3124–3132 (2017).

129. Przanowski, P. *et al.* Oncogenic TRIM37 Links Chemoresistance and Metastatic Fate in Triple-Negative Breast Cancer. *Cancer Research* **80**, 4791–4804 (2020).

130. American Cancer Society - Chemotherapy for Breast Cancer. https://www.cancer.org/cancer/types/breast-cancer/treatment/chemotherapy-for-breast-cancer.html (2021).

131. Bonadonna, G. *et al.* Combination Chemotherapy as an Adjuvant Treatment in Operable Breast Cancer. *N Engl J Med* **294**, 405–410 (1976).

132. Hanna, PharmD, Bcps, Bcop, K. & Mayden, Msn, Fnp, Aocnp, K. Chemotherapy Treatment Considerations in Metastatic Breast Cancer. *JADPRO* **12**, (2021).

133. Plunkett, W. *et al.* Gemcitabine: metabolism, mechanisms of action, and self-potentiation. *Semin Oncol* **22**, 3–10 (1995).

134. Huang, P., Chubb, S., Hertel, L. W., Grindey, G. B. & Plunkett, W. Action of 2',2'-difluorodeoxycytidine on DNA synthesis. *Cancer Res* **51**, 6110–6117 (1991).

135. Heinemann, V. *et al.* Cellular elimination of 2',2'-difluorodeoxycytidine 5'-triphosphate: a mechanism of self-potentiation. *Cancer Res* **52**, 533–539 (1992).

136. Green, M. R. Gemcitabine safety overview. *Semin Oncol* **23**, 32–35 (1996).

137. Possinger, K. *et al.* Phase II study of gemcitabine as first-line chemotherapy in patients with advanced or metastatic breast cancer: *Anti-Cancer Drugs* **10**, 155–162 (1999).

138. Carmichael, J. *et al.* Advanced breast cancer: a phase II trial with gemcitabine. *JCO* **13**, 2731–2736 (1995).

139. Schmid, P. *et al.* Phase II trial of gemcitabine as prolonged infusion in metastatic breast cancer: *Anti-Cancer Drugs* **10**, 625–632 (1999).

140. Brodowicz, T. *et al.* Single-agent gemcitabine as second- and third-line treatment in metastatic breast cancer. *The Breast* **9**, 338–342 (2000).

141. Spielmann, M. *et al.* Single-Agent Gemcitabine Is Active in Previously Treated Metastatic Breast Cancer. *Oncology* **60**, 303–307 (2001).

142. Blackstein, M. *et al.* Gemcitabine as First-Line Therapy in Patients with Metastatic Breast Cancer: A Phase II Trial. *Oncology* **62**, 2–8 (2002).

143. Lüftner, D. *et al.* Gemcitabine for palliative treatment in metastatic breast cancer. *Journal of Cancer Research and Clinical Oncology* **124**, 527–531 (1998).

144. Bosiljcic, M. *et al.* Targeting myeloid-derived suppressor cells in combination with primary mammary tumor resection reduces metastatic growth in the lungs. *Breast Cancer Res* **21**, 103 (2019).

145. Ko, H.-J. *et al.* A Combination of Chemoimmunotherapies Can Efficiently Break Self-Tolerance and Induce Antitumor Immunity in a Tolerogenic Murine Tumor Model. *Cancer Research* **67**, 7477–7486 (2007).

146. Suzuki, E., Kapoor, V., Jassar, A. S., Kaiser, L. R. & Albelda, S. M. Gemcitabine Selectively Eliminates Splenic Gr-1+/CD11b+ Myeloid Suppressor Cells in Tumor-Bearing Animals and Enhances Antitumor Immune Activity. *Clinical Cancer Research* **11**, 6713–6721 (2005).

147. Bergenfelz, C., Roxå, A., Mehmeti, M., Leandersson, K. & Larsson, A.-M. Clinical relevance of systemic monocytic-MDSCs in patients with metastatic breast cancer. *Cancer Immunol Immunother* **69**, 435–448 (2020).

148. Wu, C. *et al.* Tumor Microenvironment following Gemcitabine Treatment Favors Differentiation of Immunosuppressive Ly6Chigh Myeloid Cells. *The Journal of Immunology* **204**, 212–223 (2020).

149. Denkert, C. *et al.* Tumour-infiltrating lymphocytes and prognosis in different subtypes of breast cancer: a pooled analysis of 3771 patients treated with neoadjuvant therapy. *The Lancet Oncology* **19**, 40–50 (2018).

150. Sunderkötter, C. *et al.* Subpopulations of Mouse Blood Monocytes Differ in Maturation Stage and Inflammatory Response. *The Journal of Immunology* **172**, 4410–4417 (2004).

151. Aliazis, K., Yenyuwadee, S., Phikulsod, P. & Boussiotis, V. A. Emergency myelopoiesis in solid cancers. *Br J Haematol* **205**, 798–811 (2024).

152. Boivin, G. *et al.* Durable and controlled depletion of neutrophils in mice. *Nat Commun* **11**, 2762 (2020).

153. Shipley, L. A. *et al.* Metabolism and disposition of gemcitabine, and oncolytic deoxycytidine analog, in mice, rats, and dogs. *Drug Metab Dispos* **20**, 849–855 (1992).

154. Thibaut, R. *et al.* Bystander IFN-γ activity promotes widespread and sustained cytokine signaling altering the tumor microenvironment. *Nat Cancer* **1**, 302–314 (2020).

155. Ghanekar, S. A. *et al.* Gamma Interferon Expression in CD8 $^{+}$ T Cells Is a Marker for Circulating Cytotoxic T Lymphocytes That Recognize an HLA A2-Restricted Epitope of Human Cytomegalovirus Phosphoprotein pp65. *Clin Diagn Lab Immunol* **8**, 628–631 (2001).

156. Szabo, S. J. *et al.* Distinct Effects of T-bet in T $_{H}$ 1 Lineage Commitment and IFN-γ Production in CD4 and CD8 T Cells. *Science* **295**, 338–342 (2002).

157. Sturge, C. R., Burger, E., Raetz, M., Hooper, L. V. & Yarovinsky, F. Cutting Edge: Developmental Regulation of IFN-γ Production by Mouse Neutrophil Precursor Cells. *J Immunol* **195**, 36–40 (2015).

158. Gomez, J. C. *et al.* Mechanisms of Interferon-γ Production by Neutrophils and Its Function during *Streptococcus pneumoniae* Pneumonia. *Am J Respir Cell Mol Biol* **52**, 349–364 (2015).

159. Ethuin, F. *et al.* Human neutrophils produce interferon gamma upon stimulation by interleukin-12. *Laboratory Investigation* **84**, 1363–1371 (2004).

160. Zea, A. H. *et al.* Arginase-Producing Myeloid Suppressor Cells in Renal Cell Carcinoma Patients: A Mechanism of Tumor Evasion. *Cancer Research* **65**, 3044–3048 (2005).

161. Sinha, P., Clements, V. K., Fulton, A. M. & Ostrand-Rosenberg, S. Prostaglandin E2 Promotes Tumor Progression by Inducing Myeloid-Derived Suppressor Cells. *Cancer Research* **67**, 4507–4513 (2007).

162. Veltman, J. D. *et al.* COX-2 inhibition improves immunotherapy and is associated with decreased numbers of myeloid-derived suppressor cells in mesothelioma. Celecoxib influences MDSC function. *BMC Cancer* **10**, 464 (2010).

163. Takeda, Y. *et al.* A TLR3-Specific Adjuvant Relieves Innate Resistance to PD-L1 Blockade without Cytokine Toxicity in Tumor Vaccine Immunotherapy. *Cell Reports* **19**, 1874–1887 (2017).

164. Shirota, Y., Shirota, H. & Klinman, D. M. Intratumoral Injection of CpG Oligonucleotides Induces the Differentiation and Reduces the Immunosuppressive Activity of Myeloid-Derived Suppressor Cells. *The Journal of Immunology* **188**, 1592–1599 (2012).

165. Luo, W. *et al.* Repolarization of Tumor-Infiltrating Myeloid Cells for Augmentation of CAR T Cell Therapies. *Front. Immunol.* **13**, 816761 (2022).

166. Zoglmeier, C. *et al.* CpG Blocks Immunosuppression by Myeloid-Derived Suppressor Cells in Tumor-Bearing Mice. *Clinical Cancer Research* **17**, 1765–1775 (2011).

167. Shime, H. *et al.* Toll-like receptor 3 signaling converts tumor-supporting myeloid cells to tumoricidal effectors. *Proc. Natl. Acad. Sci. U.S.A.* **109**, 2066–2071 (2012).

168. Peek, M. C. L. & Wu, F. High-intensity focused ultrasound in the treatment of breast tumours. *Ecancermedicalscience* **12**, 794 (2018).

169. Van Der Woude, L. L., Gorris, M. A. J., Halilovic, A., Figdor, C. G. & De Vries, I. J. M. Migrating into the Tumor: a Roadmap for T Cells. *Trends in Cancer* **3**, 797–808 (2017).

170. Schouppe, E. *et al.* Tumor-induced myeloid-derived suppressor cell subsets exert either inhibitory or stimulatory effects on distinct CD 8 $^{+}$ T -cell activation events. *Eur J Immunol* **43**, 2930–2942 (2013).

171. Ku, A. W. *et al.* Tumor-induced MDSC act via remote control to inhibit L-selectin-dependent adaptive immunity in lymph nodes. *eLife* **5**, e17375 (2016).

172. Mackey, J. R. *et al.* Functional nucleoside transporters are required for gemcitabine influx and manifestation of toxicity in cancer cell lines. *Cancer Res* **58**, 4349–4357 (1998).

173. Yi-Zheng, X. & Plunkett, W. Modulation of deoxycytidylate deaminase in intact human leukemia cells. *Biochemical Pharmacology* **44**, 1819–1827 (1992).

174. Hunsucker, S. A., Mitchell, B. S. & Spychala, J. The 5′-nucleotidases as regulators of nucleotide and drug metabolism. *Pharmacology & Therapeutics* **107**, 1–30 (2005).

175. Rudin, D., Li, L., Niu, N., R. Kalari, K. & A. Gilbert, J. Gemcitabine Cytotoxicity: Interaction of Efflux and Deamination. *J Drug Metabol Toxicol* **02**, (2011).

176. Musyuni, P. *et al.* Precision medicine: Ray of hope in overcoming cancer multidrug resistance. *Drug Resistance Updates* **65**, 100889 (2022).

177. Mukhopadhyay, S. *et al.* Undermining Glutaminolysis Bolsters Chemotherapy While NRF2 Promotes Chemoresistance in KRAS-Driven Pancreatic Cancers. *Cancer Res* **80**, 1630–1643 (2020).

178. Zhang, H.-S. *et al.* NRF2 facilitates breast cancer cell growth via HIF1α-mediated metabolic reprogramming. *The International Journal of Biochemistry & Cell Biology* **95**, 85–92 (2018).

179. Lee, Y. S., Kang, J., Jung, E. S. & Lee, A. High Expression of NRF2 and Low Expression of KEAP1 Predict Worse Survival in Patients With Operable Triple-Negative Breast Cancer. *J Breast Cancer* **26**, 461 (2023).

180. Perussia, B. Lymphokine-activated killer cells, natural killer cells and cytokines. *Current Opinion in Immunology* **3**, 49–55 (1991).

181. Glasner, A. *et al.* NKp46 Receptor-Mediated Interferon-γ Production by Natural Killer Cells Increases Fibronectin 1 to Alter Tumor Architecture and Control Metastasis. *Immunity* **48**, 107-119.e4 (2018).

182. Bhat, P., Leggatt, G., Waterhouse, N. & Frazer, I. H. Interferon-γ derived from cytotoxic lymphocytes directly enhances their motility and cytotoxicity. *Cell Death Dis* **8**, e2836–e2836 (2017).

183. Briesemeister, D. *et al.* Tumor rejection by local interferon gamma induction in established tumors is associated with blood vessel destruction and necrosis. *Intl Journal of Cancer* **128**, 371–378 (2011).

184. Lu, Y. *et al.* Responsiveness of Stromal Fibroblasts to IFN-γ Blocks Tumor Growth via Angiostasis. *The Journal of Immunology* **183**, 6413–6421 (2009).

185. Pulaski, B. A., Smyth, M. J. & Ostrand-Rosenberg, S. Interferon-gamma-dependent phagocytic cells are a critical component of innate immunity against metastatic mammary carcinoma. *Cancer Res* **62**, 4406–4412 (2002).

186. duPre', S. A., Redelman, D. & Hunter, K. W. Microenvironment of the murine mammary carcinoma 4T1: Endogenous IFN-γ affects tumor phenotype, growth, and metastasis. *Experimental and Molecular Pathology* **85**, 174–188 (2008).

187. Gebremeskel, S. *et al.* Natural Killer T-cell Immunotherapy in Combination with Chemotherapy-Induced Immunogenic Cell Death Targets Metastatic Breast Cancer. *Cancer Immunology Research* **5**, 1086–1097 (2017).

188. ClinicalTrials.gov - FUSA With Intratumoral PolyICLC in Regionally Advanced Resectable Melanoma (Mel 70). https://clinicaltrials.gov/study/NCT06472661?cond=Melanoma&intr=Ultrasound&locStr=Virginia&country=United%20States&state=Virginia&rank=1.

189. Kastenmüller, W. *et al.* Peripheral Prepositioning and Local CXCL9 Chemokine-Mediated Guidance Orchestrate Rapid Memory CD8+ T Cell Responses in the Lymph Node. *Immunity* **38**, 502–513 (2013).

190. NIH National Cancer Institute - Clinical Trial: Focused Ultrasound with Low-Dose Gemcitabine to Increase Immune Control in Patients with Stage I-III Breast Cancer TRIAL. https://www.cancer.gov/research/participate/clinical-trials-search/v?id=NCI-2021-13963.